CORRELATION BETWEEN GEOMAGNETIC FIELD VARIATIONS AND THE DYNAMICS OF THE EQUATORIAL IONOSPHERE OVER EAST AFRICA

BY

OMONDI GEORGE ERICK

A THESIS SUBMITTED IN FULFILMENT OF THE REQUIREMENTS FOR THE DEGREE OF DOCTOR OF PHILOSOPHY IN PHYSICS

DEPARTMENT OF PHYSICS AND MATERIALS SCIENCE

MASENO UNIVERSITY

DECLARATION

This thesis is my own work and has not been presented to any university for award of any degree.

Omondi George Erick

PHD/SC/00038/2014

Signature: .... Date: ....

This thesis has been presented with our approval as supervisors.

Prof. Paul Baki
Department of Physics and Space Science,
Technical University of Kenya,
P.O Box 52428-00200,
Nairobi, Kenya.

Signature: .... Date: ....

Dr. Boniface Ndinya
Department of Physics,
Masinde Muliro University of Science and Technology,
P.O Box 190-50105,
Kakamega, Kenya.

Signature: .... Date: ....

ACKNOWLEDGEMENT

I am indebted to Professor Paul Baki, my supervisor, who introduced me to the field of Space Physics. Forgetting the many recommendation letters he wrote to ensure that I am sponsored to attend Space Science workshops and conferences and his continuous encouragement to keep working hard is unimaginable. I cannot forget to appreciate Dr. Boniface Ndinya, my other supervisor, for guiding me through this work and keeping me on toes through constant reminders of how fast time was running out. My gratitude to the Scientific Committee on Solar-Terrestrial Physics (SCOSTEP) for awarding me the 2015 SCOSTEP visiting scholar scholarship to the South African National Space Agency (SANSA). Special thanks to SANSA for hosting me and taking care of my living expenses during the entire period I stayed at the institution. Many thanks to, Dr. John Bosco Habarulema, for his brilliant and inspirational supervision during my stay at SANSA. A word of gratitude goes to Maseno University for tuition fee waiver that reduced the cost of this study. I thank my wife Anne for her tremendous support and motivation throughout my research period. Finally and most importantly, I thank the Almighty God for making all these things come to pass. Indeed, as stated in His Holy scriptures, apart from Him I can do nothing.

DEDICATION

To my parents, wife Anne and daughter Alicia

ABSTRACT

The geomagnetic field shows regular variation during geomagnetic quiet conditions. However, during geomagnetic storms, it exhibits irregular fluctuations that can induce hazardous electric currents in ground based conductor systems. Total electron content (TEC) is an important ionospheric parameter capable of causing Global Positioning System (GPS) signal delays, scintillations and loss of lock resulting in inefficient operations of ground and space based satellite systems. The correlation between TEC and geomagnetic field still remains unclear, especially in East African region. The present study investigates the correlation between geomagnetic field variations and the dynamics of the equatorial ionosphere over East Africa using geomagnetic field data and GPS derived TEC and scintillation data sets within the period 2009 to 2014. The objectives of the study are to determine the annual variation of geomagnetic field from low solar activity year (2009) to high solar activity year (2014) during quiet and storm times within equatorial East Africa; investigate the annual morphology of TEC; investigate the correlation between geomagnetic field variations and TEC during quiet and storm times and investigate the possibility of inferring TEC from quiet time geomagnetic field variations. These objectives have been accomplished by use of the methods of scientific programming and statistical analyses. During quiet times, the correlation coefficients (corrcoef) were found to be strongest during the prenoon phase (0600-1200 LT), ranging from 0.69 to 0.98 at Addis Ababa and 0.61 to 0.97 at Nairobi. During the afternoon phase (1300-1800 LT), corrcoef range from -0.28 to 0.89 at Addis Ababa and -0.28 to 0.76 at Nairobi. The strong linear relationship is attributed to the independent increase of the eastward electric field and photo-ionization on TEC, while poor relationship is as a result of domination of photo-ionization over equatorial ionization anomaly (EIA) development. Further, the time instants of the impact of the storms on geomagnetic field and TEC exhibit a good correlation. It was observed that the global drivers of storms overwrite the local factors determining the variation of the geomagnetic field. Scintillation well correlated with depletions in TEC occurred in the post sunset sector during some months, with largest values being experienced in the March and April at Maseno. Inferring TEC from quiet time geomagnetic field variation has been found feasible. The results presented in the present thesis are useful for electric power industries, satellite-based communication and navigational systems as well as ionospheric modelers.

TABLE OF CONTENTS

LIST OF ABBREVIATIONS AND ACRONYMS

AE- Auroral electrojet

AFRL-Air Force Research Laboratory

AGW-Acoustic Gravity Wave

CEJ-Counter electrojet

CHAMP-CHAllenging Minisatellite Payload

CMEs-Coronal mass ejections

corrcoef-correlation coefficient

D-Declination

Dst-Disturbance storm time

DCB- Differential code bias

DDE-disturbance dynamo electric field

EEJ- Equatorial electrojet

EIA-Equatorial Ionization Anomaly

ESP-Earth Surface Potential

EUV-Extreme Ultraviolet

GIC-Geomagnetically Induced Current

GNSS-Global Navigation Satellite System

GPS-Global Positioning System

GSM- Geocentric Solar Magnetospheric

GUVI-Global Ultraviolet Imager

H-Horizontal intensity

IEF-Interplanetary Electric Field

IAGA-International Association of Geomagnetism and Aeronomy

IGS-International GNSS Service

IMF-Interplanetary Magnetic Field

INTERMAGNET-International Real-time Magnetic Observatory Network

IQD-International Quiet Days

LT-Local time

MAGDAS-MAGnetic Data Acquisition System

MM-Magnetic meridian

NASA-National Aeronautics and Space Administration

NOAA-National Oceanic and Space Administration

PRN-Pseudo Random Number

RINEX-Receiver INdependent EXchange

ROCSAT1-Republic of China Satellite 1.

S_4-Amplitude scintillation

SC-storm sudden commencement

SCINDA-Scintillation Network Decision Aid

Sd(H)- storm time variation of *H*-component

SD(H)-storm time perturbation on *H*-component

SEPs-solar energetic particles

SERC-Space Environment Research Center

SFUs- solar flux units

Sq.-quiet daily variation

$Sq(D)$ - Quiet daily variation in declination

$Sq(H)$ -Quiet daily variation in the horizontal intensity

STEC- Slant total electron content.

SYM-H- Symmetric-H.

TEC-Total electron content

TECU-TEC-units

TIMED-Thermosphere Ionosphere Mesosphere Energetics and Dynamics

UT-Universal time

VTEC-Vertical total electron content

Z-Vertical intensity

LIST OF TABLES

LIST OF FIGURES

CHAPTER ONE: INTRODUCTION

The geomagnetic field has its main source in the fluid outer core of the Earth. Near the Earth's surface, it varies spatially and temporally on a range of scales due to processes from deep interior of the Earth, crust, ionosphere, magnetosphere, to the sun **(Macmillan, 2006)**. During quiet times, the geomagnetic field has a regular variation with a fundamental period of 24 hours. This regular variation, called quiet daily variation (Sq)**(Campbell, 1982)**, is dependent on local time, geomagnetic latitude, season and solar cycle and is caused by electric currents in the upper atmosphere. On the other hand, active solar activity results in flares and coronal mass ejections (CMEs) which can join solar wind (solar plasma and remnant of solar magnetic field) flowing towards the magnetosphere as a result of pressure difference between the solar corona and interstellar space **(Kivelson and Russel, 1995, p.91)**. During interaction of the magnetosphere and Earth's magnetic field with solar wind, the solar wind and geomagnetic field can undergo magnetic reconnection resulting in entry of the solar wind constituents into the Earth's atmosphere. This entry of the solar wind constituents into the terrestrial atmosphere causes a disturbance on the geomagnetic field called geomagnetic storm. Specifically, it makes the geomagnetic field undergo noteworthy deviations from its normal quiet day pattern **(Fejer, 2002).** The geomagnetic field is measured using magnetometers found in magnetic observatories (stations). The geomagnetic stations are set up by specific organizations and their partners around the world. Examples of magnetic observatory networks include International Real-time Magnetic Observatory Network (INTERMAGNET) and MAGnetic Data Acquisition System (MAGDAS).

A number of studies have been carried out on geomagnetic field variations during geomagnetic quiet and disturbed times. For example, considering recent studies in Africa, **ElHawary *et al.* (2012)** studied the Sq variations of the geomagnetic field of the ten International Quiet Days (IQD) by using geomagnetic data from MAGDAS I and II stations selected around the 96^0 Magnetic Meridian (MM) over Africa and analyzed from September 2008 to August 2009. The study involved the analysis of the horizontal (H) and declination (D) components of the geomagnetic field and found that quiet daily variation in the horizontal geomagnetic field intensity, *S*q (*H*) and declination, *S*q (*D*), show a predominant annual variation. **Abbas *et al.* (2013)** used hourly variation of H and D from Aswan and Nairobi magnetometer stations for the period from January to December, 2008 to study the variation pattern of Sq and solar disturbed conditions. The variation pattern of Sq obtained showed that the maximum intensity of Sq occurred around local noon and the magnitudes of variation during disturbed conditions were noted to be greater than those during quiet times for the same geomagnetic field element. The aforementioned studies used hourly averaged geomagnetic field data during periods of low solar activity. The present study aims to determine the variations of the geomagnetic field from a period of low solar activity (the year 2009) to high solar activity (the year 2014) using high resolution (minute) geomagnetic field data. It is important to note that part of the geomagnetic field originates from the ionosphere.

The ionosphere is a region of the Earth's atmosphere that begins at about 60 km and extends beyond 1000 km, where significant numbers of free electrons and ions are present. The region as a whole is electrically quasi-neutral having approximately equal number of free electrons and ions. The free electrons and ions are produced through ionization of the neutral particles by solar radiation (solar extreme ultraviolet and X-ray radiations) and by collisions with energetic particles (solar wind) that penetrate the upper atmosphere. The ionization produced by solar wind is usually small compared with that produced by photons. Once formed the ions and electrons tend to recombine and react with other gases species to produce other ions. Thus the dynamic equilibrium in the concentration of free electrons (electron density) depends on the relative speed of production and loss processes (recombination).

The ionosphere is structured vertically in four main ionized regions: the D, E , F and the topside regions in order of the increasing altitude, that differ in composition, density, ionization sources and degree of variability and dynamics. Figure 1.1 depicts different regions of the ionosphere.

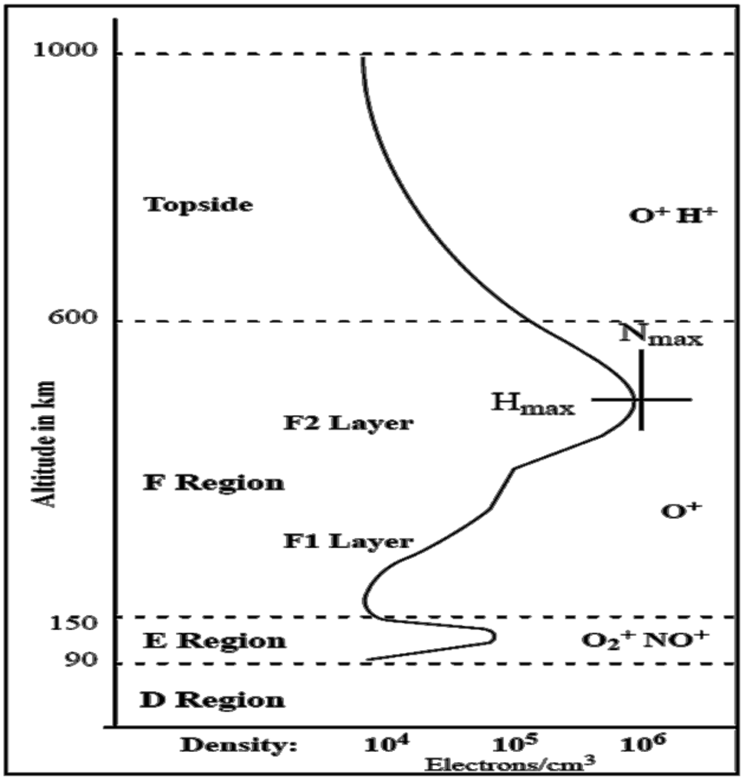

Figure1.1: Regions of the ionosphere

During the day the F region consists of two parts: F1 layer at about 170 km and F2 layer at about 250 km altitude. Above the F region is the topside ionosphere where exponentially decreasing plasma densities extend vertically to a few thousand kilometers. During night time, the D and E regions disappear mainly due to recombination between molecular ions and free electrons and the F1 and F2 layers combine to form the F region. The maximum plasma density in the ionosphere occurs in the F region. Overall plasma densities in the ionosphere vary with season, time of day, solar cycle and level of geomagnetic activity **(Akala, *et al.*, 2011).**

The dynamics of the ionosphere pose serious threats to communication and navigation systems. As a result, proper understanding of its dynamics from various aspects such as characterization, causative mechanisms and prediction remains crucial to the space science community. For instance, **Chen, *et al.*, (2009)** investigated the solar activity dependence of the topside ionosphere with Republic of China Satellite 1(ROCSAT 1) observations. The results show that in the day time, plasma density peaks around the dip equator with the peak more distinct in equinoxes and weaker in May-July and enhances with solar activity in all seasons. Some of the parameters used to quantify the dynamics of the ionosphere are the TEC and scintillation. TEC is defined as the number of electrons within a column of one square metre from the receiver on the ground up through the ionosphere to the transmitting satellite in space **(Bhuyan and Borah, 2007, Radicella, 2009)**. Apart from providing an overall description of the ionization in the ionosphere, TEC can be used for practical applications of radio wave propagation. For example, single frequency GPS users can use TEC measurements to correct their signal, since the group delay contributed by the ionosphere to the trans-ionospheric communication signals has a direct relation to the TEC in the ionosphere **(Sharma *et al*. 2012)**. The variations in TEC cause fluctuations in amplitude and phase of the signals of GPS as these signals traverse the ionosphere. This fluctuation in amplitude and phase of signals traversing the ionosphere is known as ionospheric scintillation and can cause signal degradation and, in extreme cases, loss of lock which severely affects the performance of global navigation and communication satellite systems. Ionospheric scintillations occur typically in the post sunset sector especially in the equatorial region **(Wong, 2009).** For decades, TEC has been measured using Faraday rotation effect on a linear polarized propagating plane wave but presently TEC measurements are made mostly using GPS data because of the good global coverage of the GPS observation network. TEC exhibits diurnal, seasonal and annual variations (**Sharma, *et al.*, 2012**). Some of the recent studies using TEC to quantify the dynamics of the ionosphere in Africa include **Olwendo *et al*. (2012b)** that studied TEC depletions and enhancements influenced by ionospheric irregularities in Kenya using the Global Navigation Satellite System (GNSS) data, **Adeniyi *et al.* (2014)** whose study entails the variations of the ionosphere at Ilorin, Nigeria and **Oryema *et al.* (2016)** that studied the variations of crest-to-trough TEC ratio of the East African region using Malindi and Addis Ababa data. The present study intends to investigate the annual morphology of TEC over the East African region from low to high solar activity period (year 2009 to 2014).

Quiet-time electric fields, plasma drifts and currents in the mid-to-low latitude ionosphere result from the dynamo action of E and F region neutral winds, driven by solar and lunar tides, and atmospheric gravity and planetary waves. As a result, the electric field variations and composition and distribution of low latitude ionospheric plasma are coupled. Ionospheric modelers continually work towards improving models used in predicting the dynamics of the ionosphere. One of the factors that dictate the inclusion of a variable as an input into a model is its relationship with the output. Correlation between geomagnetic field and ionospheric variations has attracted the attention of researchers in the past, with special attention given to total electron content or electron density within the range of geomagnetic pulsations Pc3-Pc5 periods from 3 to 300 seconds **(Al'perovich *et al.*1991)** and the period range of 30 to 60 minutes, which is equivalent to the period of acoustic-gravity waves (AGWs) **(Afraimovich *et al*., 2001, Afraimovich *et al*., 2006)**. The mechanisms of quantitative correlation between geomagnetic field variations and the dynamics of the ionosphere as depicted by the ionospheric parameters is not yet clear due to lack of data sets with good spatial resolution **(Afraimovich *et al*. 2006).** A possibility of such a study within East Africa is provided by the availability of GPS stations and magnetometer stations at Addis Ababa, Ethiopia and Nairobi, Kenya because of the short spatial resolution (the co-location) between the geomagnetic field data and ionospheric parameters for both stations. **Bolaji *et al.* (2013)** used simultaneous ten quiet days' records of TEC and H component of the geomagnetic field over the equatorial trough station Ilorin, Nigeria to investigate the relationship between TEC and $Sq(H)$. The dynamics of the equatorial ionosphere within the East and West African sectors are different (**Rabiu *et al*. 2012a**) and there is need to consider the entire data during geomagnetic quiet times for periods longer than one year. This thesis seeks to address this need.

The present study is motivated by the need to bridge the following gaps: knowledge gap on long term variation of geomagnetic field within East Africa; knowledge gap on correlation between geomagnetic field and ionospheric variations during geomagnetic quiet and disturbed periods and for periods longer than those of AGWs especially within the East African sector, owing to the fact that the dynamics of the ionosphere is longitudinally dependent, and the knowledge gap on the possibility of inferring TEC from $Sq(H)$.

1.1 Statement of the problem

The structure of the equatorial ionosphere is characterized by the geomagnetic field geometry and mutual interaction between plasma electrodynamics and the neutral atmosphere. The technological advancement in the recent past has resulted in enormous increase in the application of ground based electric conductor systems (influenced by geomagnetic field variations) as well as trans-ionospheric communication systems such as satellites, aircraft and surface transportation. Therefore, extensive knowledge of the ionospheric dynamics and geomagnetic field variations are of great importance to the modern society. However, the sparse instruments for measuring the ionospheric dynamics and geomagnetic field are a hindrance in the African region. The knowledge of the strength of the relationship between variations in the geomagnetic field and ionosphere is useful in determining the possibility of using geomagnetic field data to improve existing ionospheric models. A good correlation implies that the influence of one parameter on technological systems can be inferred from the other during data outages in either of the two.

The research problem in the present thesis is the variations of the geomagnetic fields and ionospheric dynamics and the, currently unclear, correlations between them over East Africa using MAGDAS, INTERMAGNET, International GNSS Service (IGS) and SCIntillation Network Decision Aid (SCINDA)-derived data sets from low solar activity to high solar activity within the solar cycle 24 with a view to answering the following outstanding research questions.

i. What is the annual variation of the geomagnetic field during the ascending phase of solar cycle 24?

ii. What are the trends of the variation of total electron content from the geomagnetic equator towards the Equatorial Ionization Anomaly region?

iii. What is the strength of the relationship between geomagnetic field variations and total electron content over East Africa?

iv. Is inference of TEC from $Sq(H)$ feasible within the East African sector?

1.2 Objectives of the study

i. To determine the mean annual variation of the geomagnetic field from low solar activity year (2009) to high solar activity year (2014) at Addis Ababa and Nairobi within East Africa.

ii. To investigate the annual morphology of total electron content at Addis Ababa, Nairobi and Maseno within East Africa for the period 2009 to 2014.

iii. To investigate the correlation between geomagnetic field variations and total electron content during quiet and storm time at Addis Ababa and Nairobi within East Africa during the period 2009 to 2014.

iv. To investigate the feasibility of inferring quiet time TEC from geomagnetic field variations at Addis Ababa and Nairobi.

1.3 Significance of the study

Accuracy in positioning using GPS is applied in communication and navigation within civilian and military sectors such as remote sensing, marine and aircrafts navigation, geographic information systems, surveying and accurate timing. The effects of the ionosphere on GPS signals are of great concern. The electron density, hence, TEC is an important ionospheric parameter that is capable of causing GPS signal delays, degradation (scintillation) and loss of lock in extreme cases, resulting in inefficient operations of ground and space based GNSS applications. Rapid fluctuations in the geomagnetic field can cause geomagnetically induced currents in electric power grid, railway and telephone lines. The knowledge of the variation of the TEC is critical to communication and navigation industries while the variations of the geomagnetic field is critical to electric power industries in decision making concerning accuracy of their measurements and the safety of their equipment. The knowledge of the strength of the relationship between the geomagnetic field variations and dynamics of the equatorial ionosphere, for the first time, within East African sector, will provide insight to ionospheric modelers as to whether one parameter can be used as a proxy or input in modeling the other parameter. The results obtained from the present study will be of significance to the civilian, industrial, military and scientific society, especially those interested in high level of positioning and timing accuracy, safety of ground based conductor systems and ionospheric modeling within the East African sector.

1.4 Justification of the study

It is known that the dynamics of the terrestrial ionosphere is complex and may behave quite differently from region to region **(Sharma *et al.,* 2012)**. From the literature presented in this thesis and to the best of our knowledge, no research has been carried within the equatorial East African region simultaneously correlating TEC variations to geomagnetic field variations, despite the need for better understanding of the relationship between geomagnetic field variations and morphology of the equatorial ionosphere. The present study takes advantage of the availability of co-located stations from which both TEC and magnetic field data sets specific to each station can be obtained as well as data from the SCINDA-GPS receiver at Maseno University, Kenya. Furthermore, the present study stands out from the previous researches by introducing a method of calculating Sq variations using high resolution (one minute) geomagnetic field data during all quiet periods as opposed to the commonly used hourly geomagnetic field data for a few selected quiet days.

CHAPTER TWO: LITERATURE REVIEW

This chapter presents a review of the existing scholarship in line with the present study. The chapter has been broken down into three sub-topics namely, 2.1, 2.2 and 2.3. Sub-topic 2.1 reviews previous research on geomagnetic field variations, sub-topic 2.2 presents a review of studies about the dynamics of the equatorial ionosphere and sub-topic 2.3 discusses literature on the correlation between geomagnetic field variations and the dynamics of the equatorial ionosphere. The available body of knowledge within each sub-topic has been presented chronologically.

2.1 Geomagnetic field variations

By using hourly mean values of horizontal intensity, H, declination, D and vertical intensity, Z in Japan to study the geomagnetic field variations during the year 1998, **Okeke and Hamano (2000)** found the amplitude of the variation in H, (dH) to have diurnal variation which peaks during the day at about local noon in the equatorial electrojet regions, attributed to enhanced dynamo action in these regions. Seasonal variations with more pronounced equinoctial maximum were observed in the H component of the geomagnetic field. The equinoctial maximum was due to enhanced electron density at equinox.

In a study, aimed at determining the variations of Sq for the entire solar cycle 22, that occurred during the period between 1986 and 1996, in middle latitude regions in the northern hemisphere, **Rabiu (2001)** noted that the Sq seasonal variation was maximum in June solstice and minimum in December solstice.

An investigation by **Rastogi (2004)** found that the daily and latitudinal variations of geomagnetic H and Z components comply with the Chapman's model of the equatorial electrojet in Eastern Brazil, Peru, Western and Central Africa while in the Pacific an abnormally large positive peak is observed at Trivandrum India, with decreasing magnitude at stations with increasing latitude.

Two mechanisms for the interaction of solar wind with the Earth's magnetosphere to produce electric field in the ionosphere at low to middle latitudes, namely slowly and rapidly varying southward Interplanetary Magnetic Field –IMF-B_Z were shown by **Rastogi, (2006).** The changes in the horizontal geomagnetic field intensity at the ground are largest at stations close to the magnetic equator and midday longitudes.

The variability of equatorial ionosphere was examined by **Rabiu *et al*. (2007a)** using ground based geomagnetic field data of H and Z obtained at the equatorial station of Ibadan. The results show that the values of Sq daily variation rises from the early morning period to maximum at about local noon and falls to lower values towards evening; hence the ionospheric current responsible for the magnetic field variations was inferred to build up at the early morning periods and attain maximum intensity about local noon.

After analysis of magnetic records obtained at low latitude geomagnetic observatory of Addis Ababa in Africa during the sunspot minimum year 1986 for day-to-day variability of the hourly amplitudes of solar daily variation in H and Z geomagnetic field intensities under quiet and disturbed conditions, results of **Rabiu *et al*. (2007b)** show that quiet day-to-day variability had consistent and explicable diurnal and seasonal variation and the daytime (0700-2000 hours) magnitudes were greater than the nighttime magnitudes (2000 -0700 hours through 2400 hours) for all the months in the two elements. Due to the variability in the characteristics of solar cycles the current research considered the sunspot minimum year 2009 for comparison and inclining solar activity years 2010 to 2014. The features arising from the current solar cycle, which has been observed to be the weakest solar cycle, have been identified and explained.

From another research work, **Rabiu *et al.* (2011)** examined the daily Sq for hourly profiles of H and D taken on 29th December, 2008 at ten MAGDAS stations (AAB, NAB, ASW, DES, DRB, FYM, HER, KRT, LSK and MPT) along 96^0 Magnetic Meridian (MM) in Africa. The results show that the H component experienced more variation within the equatorial electrojet zone and the EEJ appears stronger in the East than West Africa, attributed to a possible re-injection of energy as the jet flows eastward.

A study by **ElHawary *et al*. (2012)** considered the daily Sq variations of the geomagnetic field by using the geomagnetic data of the ten IQD. Geomagnetic data from MAGDAS I and II stations (LAQ, FYM, ASW, KRT, NAB, DES, LSK, MPT, DRB and HER) were selected around the 96^0 MM over Africa and analyzed from September 2008 to August 2009. The work analyzed H and D components of the geomagnetic field and found that $Sq(H)$ and $Sq(D)$ show a predominantly annual variation.

The work of **Obiekezie and Obiadazie (2013)** investigated the variability of the $Sq(H)$ in the African sector using the geomagnetic field measurements during IQD at Hermanus, Addis Ababa, Mbour and Bangui in the year 1987. An enhancement in *S*q (*H*) at Addis Ababa station was observed. The enhancement in $Sq(H)$ was attributed to the influence of equatorial electrojet (EEJ) current system.

Using hourly variation of two magnetic elements H and D from Aswan and Nairobi from January to December, 2008 to study the variation pattern of solar quiet and solar disturbed conditions, **Abbas *et al*. (2013)** noted that the variation pattern of $Sq(H)$ and $Sq(D)$ obtained shows that the maximum intensity of solar quiet currents occurred around local noon. The magnitudes of the variation on disturbed days were greater than those of the quiet condition for same element.

From the presented literature review in this sub-topic, appreciable research on geomagnetic field variations has been conducted. However, most of these previous studies considered short term (less than three years) and mean hourly geomagnetic field data. The present study has analyzed longer term data (years 2009 to 2014: six years) within the current solar cycle using high temporal resolution (one minute) data. As a result an alternative method of analyzing the data has been devised allowing the determination of general geomagnetic field variations without loss of any details, caused by the use of data with large temporal resolution.

2.2 Dynamics of the equatorial ionosphere

The equatorial ionosphere spans about 20 to 30 degrees on either side of the geomagnetic equator and is influenced by strong electromagnetic forces resulting from the horizontal orientation of the geomagnetic field in the region. The complexity of this region has ignited the attention of a number of researchers as detailed below.

According to the work of **Basu and Gupta (1967),** total electron content exhibits a latitudinal dependence analogous to the equatorial anomaly in F2 ionization. The latitudinal dependence shows a diurnal variation, being most pronounced in the afternoon between 1200 and 1530 hours local time (LT) and least prominent (almost absent) in the early morning and late evening hours.

From the results of a study of the motion of the Equatorial Ionization Anomaly (EIA) crest and its geophysical implications, **Yeh *et al*. (2001)** found that the crest forms at 0900 LT, on an average day, then moves towards the poles with a speed of about 1° per hour, in the next 2 hours, as it intensifies. The motion towards the poles is slowed as the crest reaches its highest latitude where it stays for several hours until early afternoon. The crest then weakens as it recedes with a speed of about 0.5° per hour towards the geomagnetic equator.

The work of **deHaro *et al*. (2002)** analyzed the variations of TEC during a geomagnetic storm, from measurements of ionospheric delay in code and phase, with the satellites of the GPS at Tucumán, Argentina. The TEC values were observed to exceed the average values for quiet days for the same time of year by 30%.

An investigation of the vertical TEC (VTEC) response to two severe geomagnetic storms on 15th May, 2005 and 24th August, 2005 at Bhopal, a station located near the crest of the anomaly region (geomagnetic latitude, 14.2°N) in India by **Jain *et al*. (2010)** shows more than +68% and +70% deviation in VTEC for 15th May, 2005 and 24th August, 2005 respectively, relative to the average of five quiet days of the respective months. These significant deviations in VTEC were found to be associated with prompt penetration electric field.

An analysis of the TEC derived from the IGS station at Malindi, Kenya for the periods 2004–2006 during the declining phase of solar cycle 23 by **Olwendo *et al.* (2012b)**, revealed that mean GPS–TEC values show a minimum at 0600 LT and a peak value about 1300LT.

The work of **Sharma *et al*., (2012)** showed that the diurnal variation of TEC during the period 2007-2009 at Delhi (low-latitude station), India maximizes around 1200 to 1400 LT, with minimum in pre-dawn period. However at Trivandrum (equatorial station), India, the day maximum is broad and its peak occurs around 1600 LT. The day minimum in TEC occurs between 0500 and 0600 LT at both stations.

TEC variations at Kampala during the period from 2010 to 2011 are highest during equinox and lowest during solstice as shown by **Oron *et al*., (2013)**. Further, the mean TEC varies from pre-dawn minimum to afternoon maximum (1300-1800 LT), reducing after sunset.

Research conducted by **Oryema *et al*., (2015)** shows that Addis Ababa which is located at the trough of the equatorial ionization anomaly recorded higher TEC values than Malindi and Kampala stations which are closer to the Southern crest of the ionization anomaly. In addition, the TEC data from Addis Ababa exhibited a good correlation with geomagnetic storm indices during the storm of 9th March, 2012.

In summary, it is important to note that, the studies of the dynamics of the ionosphere in the East African sector have paid more attention to short term (less than 3 years) variation of TEC. Extensive studies of the ionosphere are still necessary for better understanding of its ever changing morphology. The present study investigates the TEC variation on a larger temporal scale (6 years) during the ascending phase of the solar cycle 24. The dynamics of the ionosphere also varies during different solar cycles.

2.3 Correlation between geomagnetic field variations and the dynamics of the ionosphere

The global evolution of two major geomagnetic storms, occurring on 4th November, 1993 and 26th November, 1994 respectively was investigated by **Ho *et al*. (1998)**. They found a good correlation between gradients of the storm time disturbance (Dst) index and global ionospheric TEC changes. The correlation suggested that the high latitude sub-storms affect the ionosphere through a direct, possibly electromagnetic, coupling process.

Using one minute averages of $Sq(H)$ from Peru, South America, **Anderson *et al.* (2002)** gave a quantitative report concerning the relationship between ΔH and $\vec{E} \times \vec{B}$ drifts. Their results based on 10 days of observations, reported a direct proportionality between ΔH and $\vec{E} \times \vec{B}$ drifts.

A comparative analysis of TEC variations and geomagnetic field variations during the major geomagnetic storm on 29th to 31st October, 2003 as well as the moderate geomagnetic activity period on 13th to 18th October, 1999 for the mid-latitude ionosphere in North America and Central Europe as well as California in the United States of America was performed by **Afraimovich *et al.* (2006)**. It was found that magnetic field intensity variations for the period range of 30-60 minutes correlate well with TEC variations of the same time scale (though the numerical values of the correlation coefficients were not stated) during the geomagnetic storm. However, a similar dependence was not observed in California for the moderate geomagnetic activity period.

The study by **Stolle *et al.*, (2008)** investigated the response of EIA derived from the proxy of equatorial electrojet (ΔH) over the equatorial crest and trough within South America by use of Challenging Minisatellite Payload (CHAMP). The study found that a weak Counter electrojet (CEJ) event (less than 1 hour duration with magnitude less than $-5\,nT$) is associated with eastward electric field but EIA does not respond to it. Nevertheless, if contrary conditions are satisfied, the magnitude of EIA gradually decreases and reduces significantly with response time of approximately 1 to 2 hours after the occurrence of the CEJ.

The investigation by **Bolaji *et al.*, (2013)** used TEC and H-field for 10 quiet days to study the relationship between TEC variations and $Sq(H)$ over the equatorial trough station, Ilorin in Nigeria. They found that the best relationship exists between the two parameters during the prenoon phase of the day time (0600-1200 LT).

The work of **Chakraborty *et al.* (2015)** studied the response of GPS-TEC to two geomagnetic storms of 24th April, 2012 and 15th July, 2012, at two stations around 92^0 longitudes in Indian sector during the rising phase of solar cycle 24. They observed significant enhancements up to 150% and depletions up to 72% in TEC in comparison to normal quiet day variation.

In brief, it is worth noting here that mechanisms of correlation between geomagnetic variations and ionospheric parameters are not yet clearly understood because of lack of statistically significant sets of experimental data with good spatial resolution **(Afraimovich *et al.* 2006, Bolaji *et al*. 2013).** The present study has chosen Addis Ababa, Ethiopia and Nairobi, Kenya because both places have closely located magnetometers and GPS receivers and no such studies have been carried out in this sector, yet the information is necessary for GPS users, ionospheric modelers, and electric power grid and pipeline industries.

CHAPTER THREE: BACKGROUND THEORY

The current chapter presents a discussion of the theoretical and equipment aspects guiding this thesis. It begins by providing a discussion of the sun which is the main energy source responsible for the creation of plasma in the ionosphere. The ionospheric electrodynamics, geomagnetic field and equipment from which data used in the thesis were obtained are explained.

3.1 The Sun

The Sun (radius, $R_s \approx 6.9599 \times 10^8$ km, mass $\approx 1.989 \times 10^{30}$ kg) is one of the estimated 100 billion stars in the Milky Way galaxy. It is the Earth's primary source of energy. In the solar centre nuclear reactions convert hydrogen to helium; hence the relative abundance of helium is higher than the other heavier elements. Figure 3.1 shows regions of the sun.

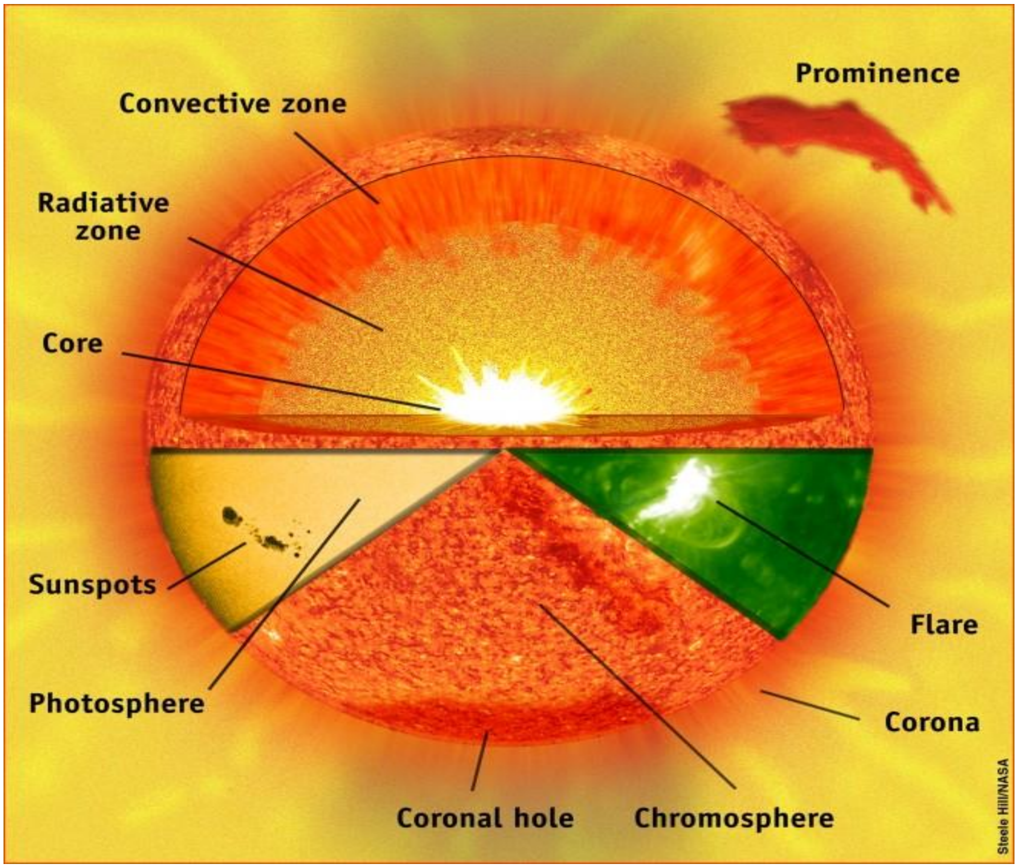

Figure 3.1: Parts of the sun

Figure 3.1 shows the sun’s interior showing parts, such as core, radiative, convective zones as observed by the Solar and Heliospheric Observatory (SOHO).

(http://sohowww.nascom.nasa.gov/gallery/Presentations/slides2002low.pdf. Retrieved on 1st November, 2017)

3.1.1 Core

It is the central region of the Sun where nuclear reactions consume hydrogen to form helium. Within the core are photons which immediately downgrade to hard X rays $(>10keV)$ by interactions with electrons and ions in the core, but remain trapped inside the Sun for millions of years, scattering off core material and slowly diffusing outward. The hard X-rays are usually responsible for ionization processes.

3.1.2 Radiative Zone

It surrounds the core and extends to approximately $0.7\ R_S$ in which photon- energy transport dominates. The temperature decreases with increasing radial distance as heat flows outward through successively cooler overlying layers. As the hard X-ray photons meander outward, they interact with ions and free electrons and are absorbed and re-emitted many times, each time at a lower energy and in a different direction-even back to the core. This process is called radiative diffusion. Due to radiative diffusion, the average energy of photons gradually decreases to soft X-rays as they diffuse outward. By the time the energy reaches the upper portions of the radiative zone, it is in the form of Extreme Ultraviolet (EUV) radiation: one of the main sources of ionization.

3.1.3 The Chromosphere

It is about four times thicker than the photosphere, but because of its low density produces less light. At the base of the chromospheres, the temperature reduces to 4300 K and then begins to rise, reaching about 20000 K at the top of the layer. The high temperature in the middle to upper chromosphere allows for electronic transition in the resident neutral hydrogen atoms at 656.3 nm, known as hydrogen-Balmer-α $(H-\alpha)$ line. This electronic n=3 to n=2 transition provides most of the visible chromospheric radiative emissions. In the upper chromosphere, the particle density declines steeply, allowing magnetic field pressure to approach and eventually exceed thermal pressure, hence magnetism takes control.

Filaments are the relatively cool and dense thread-like features of chromospheric gas and plasma suspended in the hotter upper atmosphere by the generally horizontal magnetic field. Their temperatures range between 7000 K and 15000 K, while the surrounding material is much hotter, $(10^5 K)$ and $(10^6 K)$. They absorb more photospheric continuum radiation in H_α than they emit, therefore they are darker than the background disk. Filaments viewed near the Sun's limb are often referred to as prominences**,** because they are prominent H_α emitters glowing against a backdrop of cool space. Sometimes the magnetic fields that support the prominence or filament become unstable, allowing some of the plasma to fall to the photosphere and the remainder to accelerate into interplanetary space. Disintegrating filaments launched in Earth's direction are a source of space weather events at Earth.

3.1.4 The Corona

The corona is the Sun's outer atmosphere. The relatively few particles occupying the corona receive a lot of energy but have limited means for cooling hence they are energized to high temperatures and emit in EUV and X-ray wavelengths. These short wavelength photons associated with coronal temperature are responsible for completely ionizing coronal materials.

The ionizing radiation from the corona has far- reaching effects, creating ionospheres within the Earth's upper atmosphere and in most planetary atmospheres.

Temperature of the corona is so great that the Sun's gravity cannot prevent its expansion. Each second, a small portion of the Sun's coronal plasma escapes into space in an outflow called the solar wind.

3.1.5 Solar wind

Solar wind forms as a result of the huge pressure difference between the solar corona and the interstellar space **(Kivelson and Russel, 1996 p.99).** The pressure difference means the existence of a resultant force directed outwards from the sun despite the restraining influence of solar gravity. This resultant force is the driver of plasma outward into the interstellar space.

The solar wind which consists mainly of electrons and protons extends tenuously for more than a hundred astronomical units and surrounds the Earth and all of the planets. On average, solar wind blows past the Earth at a speed of $\approx 400\, km/s$ **(Knipp, 2011 p. 209)**.

3.2 Quiet Sun Radio emissions above the Photosphere

All portions of the solar atmosphere emit radio waves but the photospheric signal intensity is overwhelmed by radio emissions from plasma processes in the chromosphere and the corona. The amount of energy received at the Earth's surface is small hence the value reported for such radiation is often in units of $10^{-22}\, W\left(m^2 Hz\right)$ known as solar flux units (SFUs). The ambient solar radio emission from the chromosphere has two components: the background component and the slowly varying component. The background component arises primarily from the chromospheres and is the dominant contributor to the Sun output during solar minimum. The slowly varying component also arises from the chromospheres but is more closely associated with active regions. Since 1940s, solar scientists have monitored the slowly varying component of the Sun at $2.8\ GHz\ (\lambda = 10.7cm)$. In many applications, the F10.7 cm is used to describe the state of solar activity. Figure 3.2 illustrates the F10.7 index from the year 2009 to 2014.

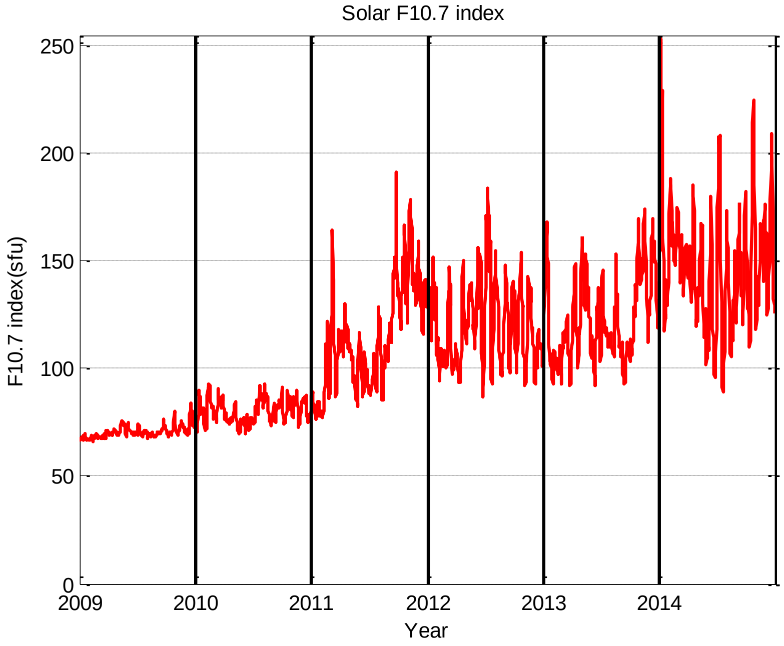

Figure 3.2: Daily averaged solar flux from 2009 to 2014

Table 3.1 shows the various quiet sun emissions and their characteristics **(Knipp, 2011, p. 13)**.

Table 3.1: Quiet solar emissions

Quiet Sun Emission	**Time to arrive at Earth**	**Impact**
Photons from $\approx$ 5800K surface	8min	Normal conditions
Minimal solar energetic particles	Several hours	Normal conditions
Solar wind plasma With strong magnetic field With high speed	100 hr 60-100hr 30hr	Normal conditions Geomagnetic storm Geomagnetic storm

3.3 Sunspots

Sunspots are regions on the Sun’s surface with lower temperatures (about 4600K) than their surroundings and thus appear as dark spots relative to their surroundings. The cooler areas are characterized by concentrated magnetic fields in which the magnetic pressure increases. The number of sunspots visible on the solar surface varies with the average of 11-year sunspot cycle which is marked by increased (solar maximum) or decreased (solar minimum) geomagnetic activity. A period of no or few observed sunspots is a sunspot minimum while a period with most sunspots is a sunspot maximum. Beginning with the minimum that occurred in 1755, sunspot cycles have been numbered. We are currently in the sunspot cycle 24 which began in January, 2008. Figure 3.3 shows Solar Cycle sunspot number progression.

(http://www.swpc.noaa.gov/products/solar-cycle-progression. Retrieved on 6th June, 2017)

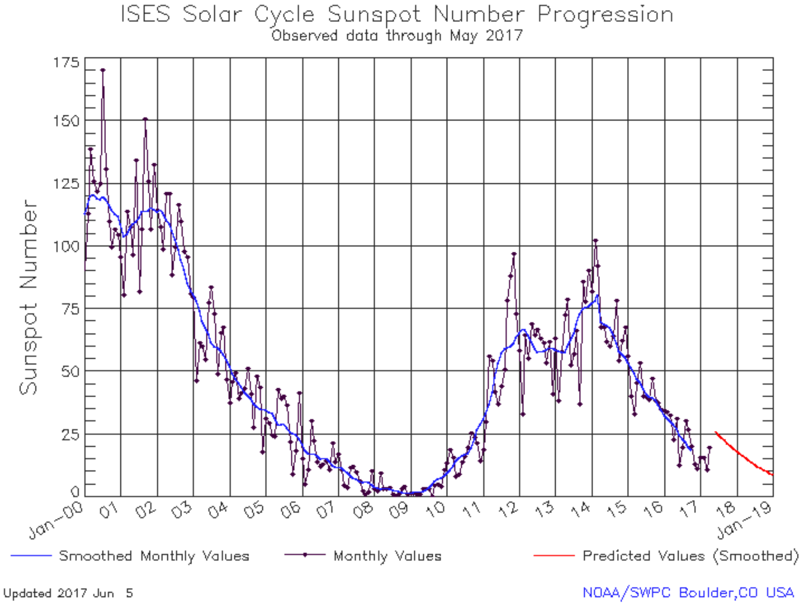

Figure 3.3: Solar Cycle sunspot number progression

The current prediction for Sunspot Cycle 24 gives a smoothed sunspot number maximum of about 72 in late 2013. The smoothed sunspot number reached a peak of 81.9 in April 2014.

This peak is speculated to be the official maximum. This second peak surpassed the level of the first peak (66.9 in February 2012). Many cycles are double peaked but this is the first in which the second peak in sunspot number was larger than the first. The current predicted and observed size makes this the smallest sunspot cycle since Cycle 14 which had a maximum of 64.2 in February of 1906 **(https://solarscience.msfc.nasa.gov/predict.shtml. Retrieved on 6th May, 2016)**.

3.4 Disturbed Solar emissions

Most of the impulsive disturbances occur when the energy stored in the solar magnetic fields transform to other forms. There are three main types of impulsive emissions.

3.4.1 Solar flares

Intense bursts of radiative energy across the entire electromagnetic spectrum, with the largest burst enhancements in the X-ray, EUV and radio sections of the spectrum.

3.4.2 Solar energetic particles (SEPs)

Protons ejected with relativistic speeds near a flare site or particles accelerated by a shock from explosion site pushing into solar wind. Some energetic particles reach the Earth in as little as 20 minutes after eruption from the Sun.

3.4.3 Coronal mass ejections (CMEs)

They are out flowing huge plasma from or through the solar corona into the interplanetary space. The parcels also carry threads of the solar magnetic field into space. CMEs vary widely in structure, density and velocity. Large and fast CMEs can approach densities of 10^{16} g/cm^3 and velocities of 2000 km/s. Earth impacting CMEs, halo-CMEs, can result in significant geomagnetic storm (a major disturbance of Earth's magnetosphere that occurs when there is a very efficient transfer of energy from the solar wind components into the space environment surrounding Earth).

Table 3.2 illustrates the disturbed solar emissions and their characteristics **(Knipp, 2011, p. 13)**.

Table 3.2: Disturbed solar emissions

Disturbed Solar Emissions	**Time to arrive at Earth**	**Impact**
Solar flare photons (X-ray-radio)	8 min	Radio blackout
Burst of solar energetic particles	15min-several hours	Radiation storm
Coronal mass ejection	20hr-120hr	Geomagnetic storm

3.5 Interplanetary Magnetic Field (IMF)

The IMF is part of the Sun's magnetic field that is carried by the solar wind. Due to the frozen-in-flux condition, the IMF travels outward in a spiral pattern originating from the regions on the Sun where open magnetic field lines emerging from do not return to a conjugate region but instead extend indefinitely into space. The frozen-in-flux condition implies that if at a given time t_0 an element of particles exists on a particular field line, then at a later time t, this element will still be on the same field line. The interaction of the IMF with the Earth's magnetic field is responsible for the shape of the magnetosphere and is one of the important conditions that determine the processes that yield geomagnetic storms. The IMF is described by three orthogonal component directions B_X , B_Y and B_Z . The directions of the IMF are important for the study of the interaction of solar wind with magnetosphere. When B_Z is positive, it is said to be northward and when negative it is referred to as southward. The accepted model for the IMF supposes that when the southward directed IMF ($-B_Z$) encounters the northward directed magnetic field of the

Earth then the field lines interconnect, distorting the Earth's dipole field and providing entry for the solar wind particles into the magnetosphere through the process of magnetic reconnection. The topography of the solar-terrestrial environment is shown in Figure 3.4 **(Baumjohann and Treumann, 1996 p. 5)**.

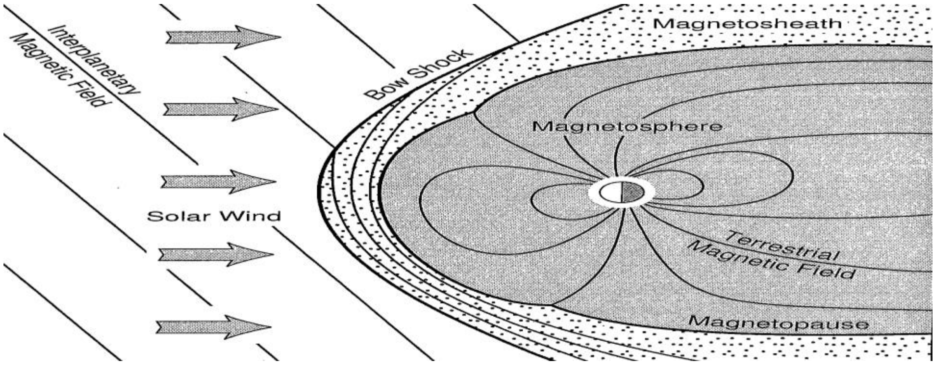

Figure 3.4: Topography of the solar-terrestrial environment

3.6 The Earth's atmosphere

The Earth's atmosphere is a layer of gases surrounding the Earth carved from the heliosphere- the sun's extended atmosphere. Figure 3.5 illustrates the relative locations of the Earth's atmospheric and magnetic regimes, as well as the heliosphere **(Knipp, 2011 p.7)**

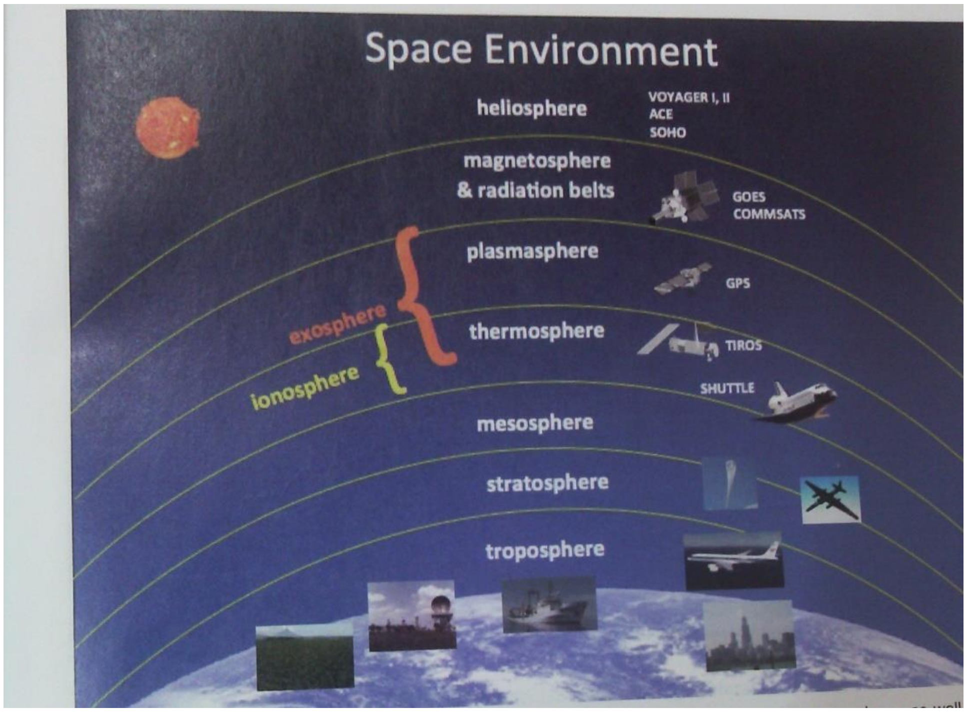

Figure 3.5: Atmospheric layers

The troposphere, between 0 and 15 km, is marked by decreasing temperature with increase in altitude.

The stratosphere is found between 15 km and 50 km and it is a region in which solar radiation creates ozone.

In the mesosphere, between 50 km-80 km, the constituents are poor absorbers of solar radiation. The region experiences rapid cooling with altitude and is dynamically unstable.

In the thermosphere, between 80 km to 1000 km, short wave radiation from the Sun interacts with tenuous and heats individual atoms and molecules. **The ionosphere** is imbedded within the thermosphere. The short wave radiation from the Sun removes electrons from parent atoms, creating distinct layers of ionization. Electric and magnetic fields control ion motion in these layers. The ionosphere affects the propagation of radio waves.

Table 3.3 summarizes some of the important features of the various regions of the Earth's ionosphere together with main constituent species of ions.

Table 3.3: Characteristics of regions of the ionosphere

Ionospheric region	**Altitude Range (km)**	**Major constituents**	**Notable characteristics**
D	70-90	NO^+ O_2^+ (molecular)	Disappears(recombines) very rapidly-minutes after sundown
E	90-140	O_2^+ (molecular) NO^+	Recombines rapidly-often disappears before midnight
F1	140-200	O^+ (atomic) NO^+	Mostly recombines after sundown but pockets may remain.
F2	200-400	O^+ (atomic)	Persistent because of low collision rates but density decreases after sundown.
Topside	>400	O^+ (atomic) H^+	Merges into the plasmasphere, atomic oxygen dominates at lower altitudes and hydrogen dominates at higher altitudes

The exosphere is the extension of the atmosphere above 300 km and the individual particles have energy that is sufficient for their escape from the Earth's gravitational field.

3.6.1 Absorption interactions in the atmosphere

When electromagnetic radiation emitted from a source such as the Sun interacts with matter, the impinging photons are reflected, transmitted or absorbed. However we shall focus on absorption because absorbed photons add energy to the gas and can lead to ionization: an important process in creation of electrons thereby electron density which control the current systems in the upper atmosphere. Absorption occurs when matter retains impinging radiant energy. We model a column of atmosphere as an infinitely long tube filled with gas as in Figure 3.6.

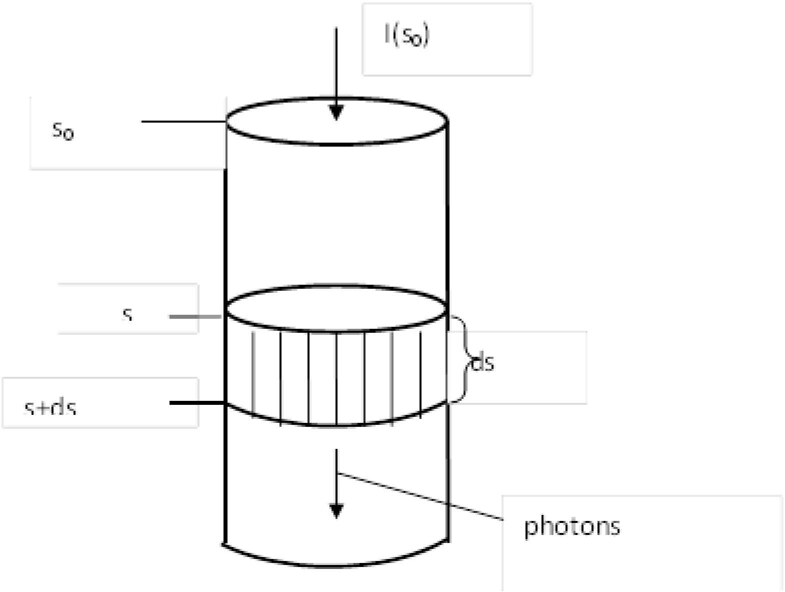

Figure 3.6: Model column of atmosphere

The number of photons emerging at location $s + ds$ is given by the number from the source of the beam minus losses (absorption) of photons to that point in the cylinder. The radiance (I) decreases as position (s) increases: $I(s_0) > I(s) > I(s + ds)$.The change in radiance (dI) is directly proportional to the length (ds) and the initial radiance at s ,(I_s). This implies that the larger the length the photon goes through the larger the loss and the larger the initial radiance.

This relationship is represented mathematically as

$$dI \propto I_s ds \tag{3.1}$$

Accounting for particle density (n) and the absorption cross-section (σ), which is the effective target size each particle presents to the beam, we write the decrement in irradiance as

$$dI = -\sigma n I_s ds \tag{3.2a}$$

The minus sign indicates that the radiance decreases with distance. Equation (3.2a) can be written as

$$\frac{dI}{I_s} = -\sigma n ds \tag{3.2b}$$

Integrating both sides of equation (3.2b) within the limits $[I_0, I_s]$ on the left and $[0, s]$ on the right, we obtain:

$$\ln\left(\frac{I_s}{I_0}\right) = -\sigma n s \tag{3.3}$$

Exponentiation of both sides of equation (3.3) gives the following result.

$$I_s = I_0 e^{-\sigma n s} \tag{3.4}$$

Introducing the optical depth defined by $\tau = \int \sigma n ds = \sigma n s$, we write equation (3.4) in the form

$$I_s = I_0 e^{-\tau} \tag{3.5}$$

The optical depth shows how effective the medium is at absorbing radiation **(Knipp, 2011 p. 132)**. If σ and n are constant, their product is sometimes written as absorption coefficient (k). The absorption coefficient determines the rate of absorption which translates into ionization processes.

3.7 Ionization and the Ionosphere

The Earth's upper atmosphere absorbs photons at wavelengths shorter than $125\,nm$ causing ionization **(Goodman, 2005)**. These photons create conducting regions of electrons and positive ions that are embedded in the neutral upper atmosphere from about $70\,km$ to $1000\,km$-the ionospheric regions. The process begins when an atom or a molecule X intercepts a EUV or X-ray photon of energy $h\upsilon$ in which h is the Planck's constant and υ is the linear frequency of the photon. The photon's energy is sufficient to detach an electron resulting in a positive ion and free electron $\left(X^{+}+e^{-}\right)$. Each interaction reduces the energy in the solar radiation beam by an amount $h\upsilon$. The production rate (R) for ionization or dissociation is obtained from equation (3.2b) according to

$$R=-\sigma n I_{s}=\frac{dI}{ds} \qquad (3.6a)$$

Now, we want to derive the shape of the profile for plasma density in the ionosphere. To do this, we determine the intensity of the ionizing photons as a function of altitude. Assuming that the Sun is directly overhead, we write equation (3.6a) in the form

$$\frac{dI}{I}=\sigma n ds \qquad (3.6b)$$

We have used the positive sign because measurement begins from bottom up (increasing altitude) hence as one moves up in the atmosphere, the light intensity increases. Substituting for number density, n given by

$$n=n_{0}e^{-\left(\frac{\Delta s}{H}\right)} \qquad (3.7)$$

where H is the scale height, equation (3.6b) takes the form

$$\frac{dI}{I}=\sigma n_{0}e^{-\frac{s}{H}}ds \qquad (3.8)$$

where $s_{0}=0$ so that; $s-s_{0}=s$.

Integrating the left hand side within the interval $[I_0, I]$ and the right hand side within the interval $[z_0, z]$, we obtain

$$\ln\left(\frac{I}{I_0}\right) = -\sigma n_0 H e^{-\left(\frac{\Delta z}{H}\right)} \tag{3.9a}$$

where $\Delta z = z - z_0$

Exponentiation of both sides of equation (3.9a) gives

$$I(z) = I_0 e^{\left(-\sigma n_0 H e^{\left(\frac{-\Delta Z}{H}\right)}\right)} \tag{3.9b}$$

The rate at which photons are lost is equal to the rate at which ions are produced. Ions and electrons strive to recombine because that is a lower potential energy state than being separated; hence they continually produce ion-electron pairs to maintain the ionospheric plasma density.

At equilibrium, the production and recombination rates balance. Substituting for number density, n, and radiance, I, in equation (3.6a) with an appropriate sign and variable notation change, we obtain the ionization rate as a function of altitude.

$$R(z) = -\frac{dI}{dz} = \sigma n(z) I(z) \tag{3.10a}$$

$$\Rightarrow R(z) = \sigma\left(n_o e^{\frac{-\Delta z}{H}}\right)\left(I_0 e^{\left(-\sigma n_0 H e^{\left(-\frac{\Delta z}{H}\right)}\right)}\right) \tag{3.10b}$$

$$R(z) = \sigma n_0 I_0 e^{\left(-\frac{\Delta z}{H}\right)}\left(e^{-\sigma n_0 H e^{-\frac{\Delta z}{H}}}\right) \tag{3.10c}$$

Clearly, equation (3.10c) shows that production rate is the product of two exponentially decaying functions. One accounts for the decrease of the ionization above the peak level and the other for the reduction in ionization below the peak level. Together they produce the shape of the Chapman function as shown in Figure 3.7 which also includes the neutral number density and radiation intensity.

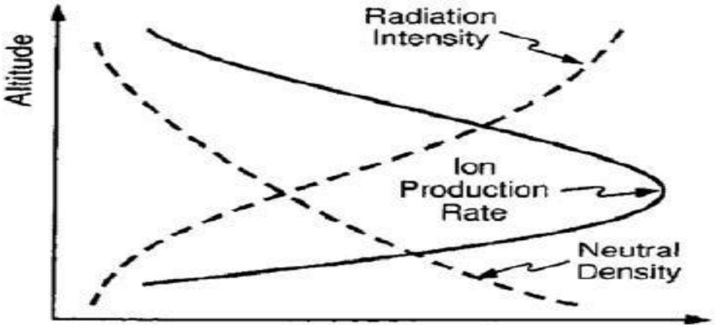

Figure 3.7: Chapman Ionization Production Rate

3.8 The Ionosphere-Thermosphere (I-T) System

Figure 3.8 shows energy input, conversion and transport processes that are useful for the I-T system **(Forbes, 2007).**

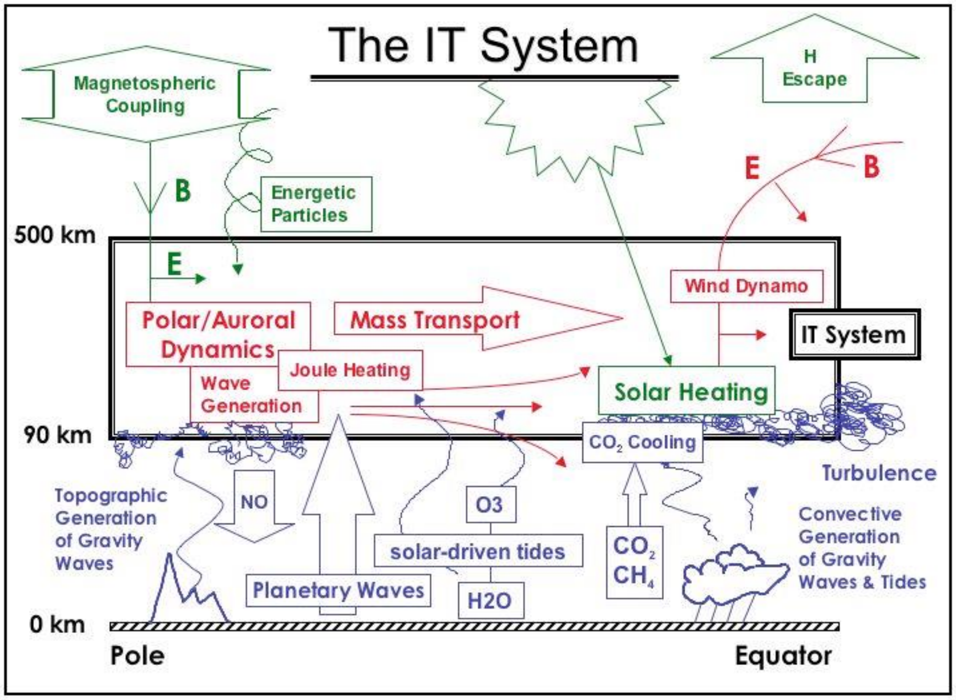

Figure 3.8: Energy input, conversion and transport processes relevant for the Ionosphere-Thermosphere system.

In addition to solar energy in form of EUV radiation, the thermosphere is affected by particle energy from the Sun in form of solar wind as follows. When the IMF, in the solar wind points southward, energy is transferred to the magnetosphere. This sets up plasma convection system in the magnetosphere which maps into the high latitude ionosphere along conducting field lines, setting neutral atmosphere into motion through ion-neutral collisions. Plasma particles are energized on the convection field lines and a number of these precipitate into the high-latitude thermosphere increasing the conductivity of the ionosphere through impact ionization of the neutral gas. This enhanced conductivity facilitates the flow of current between the magnetosphere and ionosphere, causing a net dissipation of magnetospheric energy in form of ohmic heating due to the resistivity of the ionosphere. This process, commonly called Joule dissipation of ionospheric currents can significantly modify the energetic and dynamics of the global I-T system **(Forbes, 2007).**

I-T system has a zonal-mean meridional circulation of the thermosphere driven by solar heating. It begins from summer to winter with upwelling in summer and down-welling in winter. The circulation is closed by a weak return flow to the lower thermosphere to maintain continuity of mass flow. The thermosphere primarily consists of O and N_2 between about 120 and 500 km. The ratio of O to N_2 densities is important for the ionosphere, since photo-ionization and molecular species such as N_2 and O_2 control the loss of ionosphere plasma.

3.9 Conductivity of plasma

Plasma is a gas of charged particles consisting of equal numbers of free positive and negative charge carriers; hence quasi-neutral in the stationary state due to the mutual cancellation of randomly distributed electric charges. In the presence of collisions, a collisional term is added to the equation of motion for charged particle under the action of the Coulomb and Lorentz forces. Assuming all the collision partners move with velocity $\vec{u}$, a charged particle with velocity, $\vec{v}$ experiences a resultant force of the form:

$$m\frac{d\vec{v}}{dt} = q\left(\vec{E} + \vec{v} \times \vec{B}\right) - m\upsilon_c\left(\vec{v} - \vec{u}\right) \tag{3.11}$$

The collision term, $-m\upsilon_c\left(\vec{v} - \vec{u}\right)$, on the right hand side of equation (3.11) describes the momentum lost through collisions taking place at frequency υ_c.

3.9.1 Unmagnetized plasma

Assuming a steady state in unmagnetized plasma with $\vec{B} = 0$, where all electrons move with velocity $\vec{v}_e$ and all collision partners (ions in the case of fully ionized plasma or neutrals in partially ionized plasma) are at rest, equation (3.11) takes the form:

$$0 = -e\vec{E} - m_e\upsilon_c\left(\vec{v} - 0\right) \tag{3.12a}$$

Equation (3.12a) simplifies to the form:

$$\vec{E} = -\left(\frac{m_e \upsilon_c}{e}\right)\vec{v}_e \tag{3.12b}$$

Since electrons move with relative to ions, they have a current of current density

$$\vec{J} = -en_e\vec{v}_e \tag{3.13}$$

where n_e, is the electron density e, is the electronic charge.

Dividing equation (3.12b) by equation (3.13), and rearranging, we obtain

$$\vec{E} = \frac{m_e \upsilon_c}{n_e e^2}\vec{J} \tag{3.14a}$$

Equation (3.14a) is the Ohm's law with

$$\rho = \frac{m_e \upsilon_c}{n_e e^2} \tag{3.14b}$$

being the plasma resistivity. Replacing the plasma resistivity with plasma conductivity defined by

$$\sigma_0 = \frac{1}{\rho} = \frac{n_e e^2}{m_e \upsilon_c} \tag{3.14c}$$

Ohm's law takes the form

$$\vec{J} = \sigma_0 \vec{E} \tag{3.14d}$$

3.9.2 Magnetized plasma

Magnetized plasma can move with a velocity $\vec{v}$ across the magnetic field hence the electric field, $\vec{v} \times \vec{B}$, resulting from the Lorentz transformation equation must be added to the electric field in the unmagnetized state. Ohm's law in equation (3.14d) now takes the form

$$\vec{J} = \sigma_0\left(\vec{E} + \vec{v} \times \vec{B}\right) \tag{3.15}$$

Equation (3.15) is a simple form of generalized Ohm's law, which is valid in fully ionized geophysical plasmas where typical collision frequencies are low and the plasma conductivity can be taken as near infinite. However, in the lower part of the partially ionized terrestrial ionosphere, there are abundant collisions between the ionized and neutral part of the upper atmosphere in the presence of strong magnetic field leading to a finite anisotropic conductivity tensor.

Beginning once more with equation (3.11) and assuming steady state in which all electrons move with velocity $\vec{v}_e$ and all collision partners are at rest so that $\vec{u} = 0$, but now in magnetized plasma, we obtain

$$0 = -e\left(\vec{E} + \vec{v}_e \times \vec{B}\right) - m_e \upsilon_c \vec{v}_e \tag{3.16a}$$

$$\Rightarrow \vec{E} + v_e \times \vec{B} = -\frac{m_e \upsilon_e}{e} \vec{v}_e \tag{3.16b}$$

From equation (3.13), we can write

$$\vec{v}_e = -\left(\frac{\vec{J}}{en_e}\right) \tag{3.17}$$

Substituting equation (3.17) in equation (3.15), we obtain another form of Ohm's law for magnetized plasma in the form

$$\vec{J} = \sigma_0 \vec{E} - \left(\frac{\sigma_0}{n_e e}\right) \vec{J} \times \vec{B} \tag{3.18}$$

Next, we assume that the magnetic field is aligned with the z-axis so that $\vec{B} = B\hat{e}_z$. Therefore,

$$\vec{J} \times \vec{B} = \vec{J} \times B\hat{e}_z = BJ_y \hat{e}_x - BJ_x \hat{e}_y \tag{3.19}$$

Using equation (3.19) in equation (3.18) and writing the resulting equation in terms of vector components, we obtain

$$\vec{J} = \left(\sigma_0 E_x - \frac{\sigma_0 B}{n_e e} J_y \right) \hat{e}_x + \left(\sigma_0 E_y + \frac{\sigma_0 B}{n_e e} J_x \right) \hat{e}_y + (\sigma_0 E_z)\hat{e}_z \tag{3.20}$$

We recall that $\sigma_0 = \frac{n_e e^2}{m_e \upsilon_c}$ and the electron cyclotron (gyro) frequency is given by $\omega_{ge} = \frac{-eB}{m_e} \Rightarrow B = \frac{\omega_{ge} m_e}{-e}$, where we have taken into account the fact that electron cyclotron frequency carries the sign of the charge. We use these two relations to simplify equation (3.20) obtaining

$$\vec{J} = \left(\sigma_0 E_x + \frac{\omega_{ge}}{\upsilon_c} J_y \right) \hat{e}_x + \left(\sigma_0 E_y - \frac{\omega_{ge}}{\upsilon_c} J_x \right) \hat{e}_y + (\sigma_0 E_z)\hat{e}_z \tag{3.21}$$

Extracting the components of the current density from equation (3.21), we obtain

$$J_x = \sigma_0 E_x + \frac{\omega_{ge}}{\upsilon_c} J_y \tag{3.22a}$$

$$J_y = \sigma_0 E_y - \frac{\omega_{ge}}{\upsilon_c} J_x \tag{3.22b}$$

$$J_z = \sigma_0 E_z \tag{3.22c}$$

We proceed to eliminate J_y from equation (3.22a) and J_x from equation (3.22b). We substitute equation (3.22b) into equation (3.22a) as appropriate and perform a little algebraic simplification to get

$$J_x = \frac{\upsilon_c^2}{\upsilon_c^2 + \omega_{ge}^2} \sigma_0 E_x + \frac{\omega_{ge} \upsilon_c}{\upsilon_c^2 + \omega_{ge}^2} \sigma_0 E_y \tag{3.23a}$$

Now, substituting equation (3.23a) into equation (3.22b) and performing algebraic simplification, we obtain

$$J_y = \frac{\upsilon_c^2}{\upsilon_c^2 + \omega_{ge}^2} \sigma_0 E_y - \frac{\omega_{ge} \upsilon_c}{\upsilon_c^2 + \omega_{ge}^2} \sigma_0 E_x \tag{3.23b}$$

Equation (3.22c) retains its original form. That is,

$$J_z = \sigma_0 E_z \tag{3.22c}$$

The system of equations (3.23a), (3.23b) and (3.22c) can be written as a single matrix equation of the form

$$\begin{pmatrix} J_x \\ J_y \\ J_z \end{pmatrix} = \begin{pmatrix} \frac{\upsilon_c^2}{\upsilon_c^2 + \omega_{ge}^2}\sigma_0 & \frac{\omega_{ge}\upsilon_c}{\upsilon_c^2 + \omega_{ge}^2}\sigma_0 & 0 \\ -\frac{\omega_{ge}\upsilon_c}{\upsilon_c^2 + \omega_{ge}^2}\sigma_0 & \frac{\upsilon_c^2}{\upsilon_c^2 + \omega_{ge}^2}\sigma_0 & 0 \\ 0 & 0 & \sigma_0 \end{pmatrix} \begin{pmatrix} E_x \\ E_y \\ E_z \end{pmatrix} \tag{3.24a}$$

Equation (3.24a) can further be written in a more compact form

$$\vec{J} = \sigma . \vec{E} \tag{3.24b}$$

where

$$\vec{J} = \begin{pmatrix} J_x \\ J_y \\ J_z \end{pmatrix}; \quad \vec{E} = \begin{pmatrix} E_x \\ E_y \\ E_z \end{pmatrix} \tag{3.25a}$$

and the conductivity tensor reads

$$\sigma = \begin{pmatrix} \sigma_P & -\sigma_H & 0 \\ \sigma_H & \sigma_P & 0 \\ 0 & 0 & \sigma_{||} \end{pmatrix} \tag{3.25b}$$

in which the tensor elements are defined by

$$\sigma_P = \frac{\upsilon_c^2}{\upsilon_c^2 + \omega_{ge}^2}\sigma_0 \tag{3.26a}$$

$$\sigma_H = -\frac{\omega_{ge}\upsilon_c}{\upsilon_c^2 + \omega_{ge}^2}\sigma_0 \tag{3.26b}$$

$$\sigma_{||} = \sigma_0 = \frac{n_e e^2}{m_e \upsilon_c} \tag{3.26c}$$

The tensor element σ_P is called Pedersen conductivity and governs Pedersen current in the direction of electric field $E_\perp$ which is transverse to the magnetic field. The Hall conductivity σ_H governs the Hall current in the direction perpendicular to both electric and magnetic fields (in the direction $-\vec{E} \times \vec{B}$, where the negative sign accounts for the negativity of the electron gyrofrequency). The parallel conductivity $\sigma_{||}$ governs the magnetic field –aligned current driven by parallel electric field component $E_{||}$. The parallel conductivity equals the plasma conductivity in the unmagnetized case.

When the magnetic field has an arbitrary angle with respect to the chosen coordinate, equation (3.24b) can be rewritten in terms of the three axes as follows.

$$\vec{J} = \sigma_{||}\vec{E}_{||} + \sigma_P \vec{E}_\perp - \sigma_H \left(\frac{\vec{E}_\perp \times \vec{B}}{B} \right) \tag{3.27}$$

where $\left(\frac{\vec{E}_\perp \times \vec{B}}{B} \right)$ is a unit vector in the direction of $\vec{E}_\perp \times \vec{B}$.

In a highly collisional plasma, containing weak magnetic field, $|\omega_{ge}| << \upsilon_c$. Therefore, the set of equations (3.26a), (3.26b) and (3.26c) shows that $\sigma_P = \sigma_{||} = \sigma_0$; $\sigma_H = 0$ and the conductivity tensor becomes isotropic hence reducing to a scalar. For dilute, nearly collisionless plasma with a strong magnetic field, the opposite regime $|\omega_{ge}| >> \upsilon_c$ takes course resulting in $\sigma_{||} = \sigma_0$; $\sigma_P \approx \sigma_H \approx 0$. It follows that in such plasma, the current flows essentially along the magnetic field lines.

3.10 Conductivity of the Ionosphere

For the partially ionized ionosphere, the collision partners are the neutral atmosphere particles and the general collision frequency υ_c is replaced by the electron-neutral collision frequency υ_{en}. Further, the electrons in the ionosphere are not the only ones scattered by the neutrals but also the ions. Since the current caused by the finite ion-neutral collision frequency υ_{in} is governed by the same equation as the current carried by electrons, we retain the generalized Ohm's law given in equation (3.26) if we add the ion contribution to the electron conductivity tensor elements given in equations (3.25a), (3.25b) and (3.25c). The ion conductivities are simply obtained by replacing ω_{ge} and υ_{en} by ω_{gi} and υ_{in} respectively.

Now, substituting equation (3.26c) in each of the tensor elements and using the appropriate notation for the collision frequency, we obtain, after adding the ion contributions;

$$\sigma_P = \left(\frac{\upsilon_{en}}{\upsilon_{en}^2 + \omega_{ge}^2} + \frac{m_e}{m_i} \frac{\upsilon_{in}}{\upsilon_{in}^2 + \omega_{gi}^2} \right) \frac{n_e e^2}{m_e} \tag{3.28a}$$

$$\sigma_H = -\left(\frac{\omega_{ge}}{\upsilon_{en}^2 + \omega_{ge}^2} + \frac{m_e}{m_i} \frac{\omega_{gi}}{\upsilon_{in}^2 + \omega_{gi}^2} \right) \frac{n_e e^2}{m_e} \tag{3.28b}$$

$$\sigma_{||} = \left(\frac{1}{\upsilon_{en}} + \frac{m_e}{m_i} \frac{1}{\upsilon_{in}} \right) \frac{n_e e^2}{m_e} \tag{3.28c}$$

The Hall conductivity dominates within the equatorial ionosphere due to the magnetic field being nearly orthogonal to the electric field.

3.11 The Equatorial Ionospheric currents

Ions and to a lesser degree, electrons in the E-region are coupled (attached) to the neutral components of the atmosphere, therefore follow their dynamics. Atmospheric winds and tidal oscillations of the atmosphere force the E-region ion component to move across the magnetic field lines, while electrons move much slower at right angles to both the field and neutral wind. This relative movement constitutes an electric current and the separation of charge produces an electric field which in turn affects the current. In order to gain insight into the relation between current conductivity, electric field and neutral wind velocity, $\vec{v}_n$, we must add a $\vec{v}_n \times \vec{B}$ electric field term to the Ohm's law given in equation (3.23b) to write

$$\vec{J} = \sigma.\left(\vec{E} + \vec{v}_n \times \vec{B}\right) \tag{3.29}$$

The relation shown in equation (3.28) is valid throughout the Earth's ionosphere. For mid and low latitude dynamo currents, the dominant driving force is the $\vec{v}_n \times \vec{B}$ electric field induced by ion motion across the magnetic field. On the other hand, at high latitudes, the neutral wind is usually smaller than the electric field and can safely be neglected.

The equatorial region covers about 0 to 30 degrees South or North of the magnetic equator **(Knipp, 2011 p. 373)**. It is strongly influenced by electromagnetic forces that arise due to the geomagnetic fields moving horizontally over the magnetic equator. This region is characterized with the highest values of peak electron density and most prominent amplitude and phase scintillation effects on radio signals.

Two main current systems are confined to the equatorial and low latitudes: Sq current and EEJ.

3.11.1 Sq current

Equatorial regions experience dynamo effect: daily variation in atmospheric motion caused by tides of the atmosphere. The tides are the diurnal and semidiurnal oscillations which are excited by the solar radiation heating the atmosphere. The current system created by this tidal motion is called Sq. The Sq currents which create a disturbance on the magnetic field can be estimated on the ground by use of geomagnetic field data from magnetometers and allows the determination of the strength of the currents. In accordance with the contrast between day and night equatorial E-region electron densities, the Sq currents are concentrated in the dayside region.

3.11.2 EEJ

At the geomagnetic equator, the Sq current systems of the southern and northern hemispheres touch each other forming an extended nearly jet-like current in the ionosphere. However, the electrojet current is too strong to be formed only by concentration of the Sq current. In the system with electric fields perpendicular to the north-south geomagnetic field that prevails near the geomagnetic equator together with the nearly perpendicular incidence of solar radiation cause equatorial enhancement in the effective conductivity leading to an amplification of the jet current.

Let us consider a situation where the magnetic field is horizontal to the surface of the Earth as is the case at the geomagnetic equator. The direction of the magnetic field is from South to North, along the x-axis. The primary Sq Pedersen current flows eastward, in the y direction (orthogonal to the magnetic field), parallel to the primary ionospheric electric field E_{py}. This primary electric field drives a Hall current which flows vertically downward in the z direction (perpendicular to both the primary electric field and the magnetic field), causing a charge separation in the equatorial ionosphere with negative charges accumulating at the top boundary and positive charges accumulating at the bottom of the highly conducting layer. Such processes are sketched and displayed in Figure 3.9.

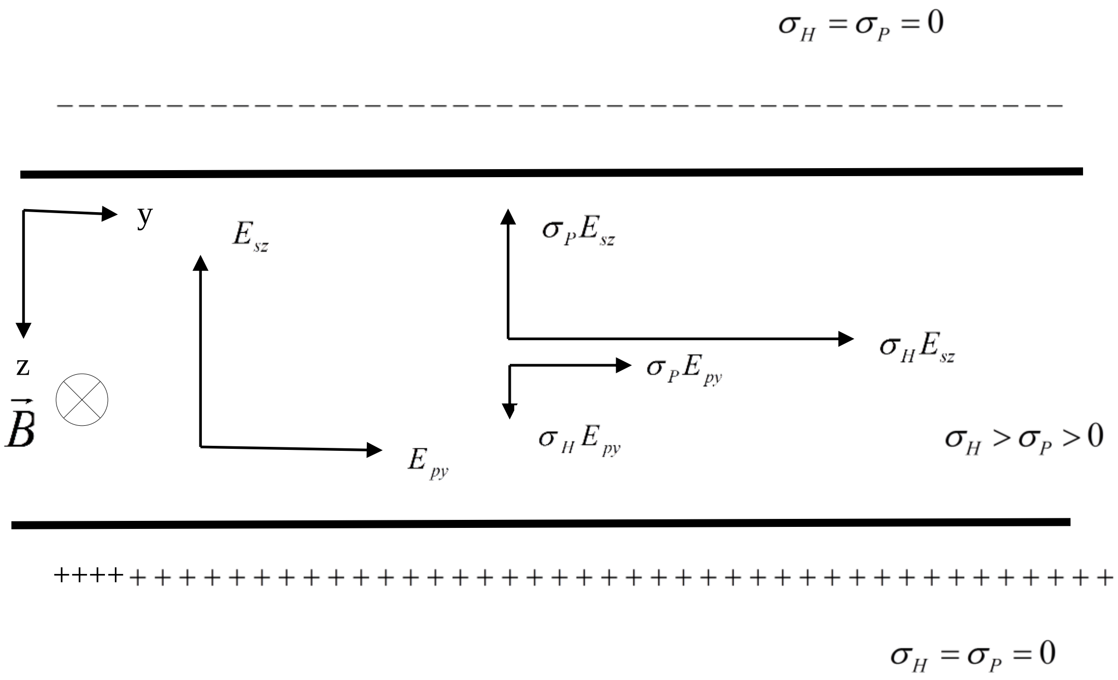

Figure 3.9: Enhancement of the effective conductivity at the geomagnetic equator

The space charge distribution creates a secondary polarization electric field E_{sz} vertically directed from the bottom to the top of the conducting ionosphere. The polarization electric field drives a vertical Pedersen current opposing the Hall current until it fully cancels it, resulting in an equilibrium condition in which no current flows in the vertical direction. Such an equilibrium condition is given by the sum;

$$J_Z = \sigma_H E_{py} + \sigma_P E_{sz} = 0 \tag{3.30}$$

from which the secondary polarization electric field is obtained as

$$E_{sz} = -\frac{\sigma_H}{\sigma_P} E_{py} \tag{3.31}$$

In addition, the secondary polarization electric field component generates a secondary Hall current component (a current perpendicular to both the secondary polarization electric field and the magnetic field directions), flowing into the y direction. The actual direction of the Hall current is the cross product of the secondary polarization electric field (which acts in the negative direction of the chosen z axis) and the magnetic field; hence the secondary Hall conductivity is given by

$$\vec{J}_{sy} = \sigma_H E_{sz}(-\hat{y}) \tag{3.32a}$$

where $\hat{y}$ is a unit vector in the positive y direction.

The Hall conductivity given in equation (3.32a) can be written in the simple form

$$J_{sy} = -\sigma_H E_{sz} = -\sigma_H \left(-\frac{\sigma_H}{\sigma_P} E_{py} \right) \tag{3.32b}$$

in which, we have substituted for E_{sz} from equation (3.31). Equation (3.32b) simplifies to

$$J_{sy} = \frac{\sigma_H^2}{\sigma_P} E_{py} \tag{3.32c}$$

The total current flowing in the eastward direction (positive y direction) consists of the primary Pedersen and the secondary Hall currents and is given by

$$J_y = J_{py} + J_{sy} = \left(\sigma_P + \frac{\sigma_H^2}{\sigma_P} \right) E_{py} \tag{3.33}$$

The conductivity term

$$\sigma_C = \left(\sigma_P + \frac{\sigma_H^2}{\sigma_P} \right) \tag{3.34}$$

is called Cowling conductivity.

For typical Hall to Pedersen ratios lying in the range of 3 to 4, the Cowling conductivity is of order of magnitude higher than the usual Pedersen conductivity; hence explaining the amplification and concentration of the equatorial electrojet above the geomagnetic equator. The strong horizontal jet current causes a magnetic field enhancement close to the dip equator but weakens the terrestrial magnetic field over a distance of about 600 km across the dip equator. Typical enhancement fields near noon at the magnetic equator are of the order of 50 to 100 nT

3.12 $\vec{E}\times\vec{B}$ drift

The behaviour of plasma can be understood in limited conditions by considering a single charged particle and the forces on it. Consider the motion of a charged particle with velocity $\vec{v}$ in the presence of external magnetic field $\vec{B}$ and electric field $\vec{E}$. The force acting on this particle is the Lorentz force with the resulting motion determined by;

$$m\frac{d\vec{v}}{dt} = q\vec{E} + q\left(\vec{v}\times\vec{B}\right) \tag{3.35}$$

where q and m are the charge and mass of the particle. For steady state motion, the time derivative of the velocity is negligible hence equation (3.35) reduces to the form

$$\vec{E} = -\left(\vec{v}\times\vec{B}\right) \tag{3.36a}$$

Whenever there is a continuous motion of ionospheric plasma in the presence of the Earth's magnetic field, there is always an electric field perpendicular to both $\vec{v}$ and $\vec{B}$. Equation (3.36a) can still be written as

$$\vec{E} = \vec{B}\times\vec{v} \tag{3.36b}$$

Taking the cross product of both sides of equation (3.36b) with $\vec{B}$ we write

$$\vec{E}\times\vec{B} = \left(\vec{B}\times\vec{v}\right)\times\vec{B} \tag{3.37}$$

We apply the simplified triple product identity $\left(\vec{A}\times\vec{B}\right)\times\vec{C}=-\vec{C}\times\left(\vec{A}\times\vec{B}\right)=-\vec{A}\left(\vec{B}.\vec{C}\right)+\vec{B}\left(\vec{A}.\vec{C}\right)$ where in this case $\vec{A}\equiv\vec{B}$, $\vec{B}\equiv\vec{v}$ and $\vec{C}\equiv\vec{B}$ to obtain;

$$\left(\vec{B}\times\vec{v}\right)\times\vec{B}=-\vec{B}\left(\vec{v}.\vec{B}\right)+\vec{v}\left(\vec{B}.\vec{B}\right) \tag{3.38}$$

Since $\vec{v}\perp\vec{B}$; it follows that $\vec{v}.\vec{B}=0$. Equation (3.38) now takes the form

$$\left(\vec{B}\times\vec{v}\right)\times\vec{B}=\left|\vec{B}\right|^2\vec{v} \tag{3.39}$$

$$\Rightarrow\vec{E}\times\vec{B}=\left|\vec{B}\right|^2\vec{v} \tag{3.40a}$$

From equation (3.40a) we obtain the expression for the charge drift velocity in the form,

$$\vec{v}=\frac{\vec{E}\times\vec{B}}{\left|\vec{B}\right|^2} \tag{3.40b}$$

During magnetically quiet periods, the main sources of ionospheric electric fields are the magnetospheric convection due to interaction of the solar wind with the Earth's magnetic field (solar wind-magnetosphere dynamo) which dominates at high latitudes and the circulation of the neutral atmosphere across the Earth's magnetic field under the influence of tidal winds (ionospheric wind dynamo) which is predominant at mid and low/equatorial latitudes.

An eastward (westward) electric field causes upward (downward) plasma drift. Thus measurement of the magnetic field line perpendicular drifts of the ionospheric plasma by radars, and satellite borne ion drift meters (and electric field sensors), are important for investigating the equatorial electric field characteristics **(Abdu *et al*. 2005)**.

In the vicinity of the dip equator during the day, the east-west electric field, $\left(\vec{E}\right)_,$ generated in the E-region dynamo gets mapped to the F-region along the conducting field lines and lift the plasma to higher altitudes in the presence of horizontal north-south magnetic field $\left(\vec{B}\right)$. The vertical plasma drift velocity takes the form given in equation (3.40b).

3.12.1 Equatorial Ionization Anomaly

A major consequence of the plasma transport during daytime and evening hours in the equatorial ionosphere is the formation of the Equatorial Ionization Anomaly (Appleton anomaly). The plasma lifted vertically up by the east-west electric field in the E-region around the dip equator diffuses downwards along magnetic field lines under the influence of gravity and pressure gradient forces resulting in crests of ionization in the north and south of the dip equator $\left(\pm 15^{\circ} - 20^{\circ}\right)$, leaving a trough of ionization at the magnetic equator. The combination of electromagnetic drift and diffusion produces a fountain like pattern of plasma motion known as the equatorial fountain as shown in Figure 3.10 **(Rastogi and Klobuchar, 1990, Anderson *et al*., 2002, Knipp, 2011 p.575)**.

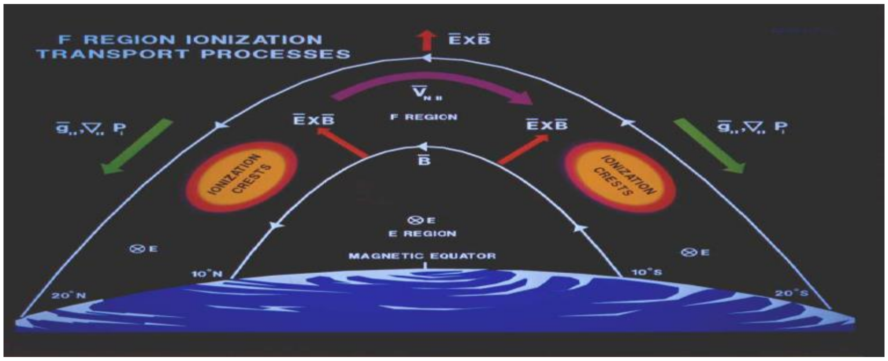

Figure 3.10: Equatorial fountain effect and ionization anomaly

3.13 Total electron content (TEC)

The TEC is a measure of the total number of electrons per square metre cross-sectional area along the line of sight from the transmitter on a satellite to the receiver on ground **(Bhuyan and Borah, 2007).** It is expressed in TEC-units (TECU) with $1\ TECU = 10^{16}$ electrons per square metre. The dispersive ionosphere introduces a time delay in the 1.57542 GHz (L1) and 1.22760

GHz (L2), simultaneous transmissions from GPS satellites orbiting at 20,200 km. Such delays can cause effects such as range errors and scintillations. Fortunately, the relative ionospheric delay of the two signals is directly proportional to TEC **(Sharma *et al*., 2012).** It follows that the time delay measurements of L1 and L2 frequencies can be converted to TEC along the ray path from the receiver to the satellite **(Lanyi and Roth, 1988)**. TEC measurements are made using the principle of the effect of the ionosphere on radio wave propagation. For decades, TEC has been measured using the Faraday rotation effect on a linear polarized propagating plane wave. But today TEC measurements are made mostly using GPS data because of the good global coverage of the GPS observation network such as the IGS and SCINDA networks.

Slant TEC (STEC) is dependent on the ray path geometry through the ionosphere. Therefore, it is important to calculate an equivalent vertical value of TEC which is independent of the ray path. This is done by assuming the ionosphere to be compressed into a thin shell at a shell height of h as shown in Figure 3.11. The vertical TEC values (VTEC) are assigned to an ionospheric pierce point, which is the intercept of the line-of-sight ray and the thin shell at the altitude h.

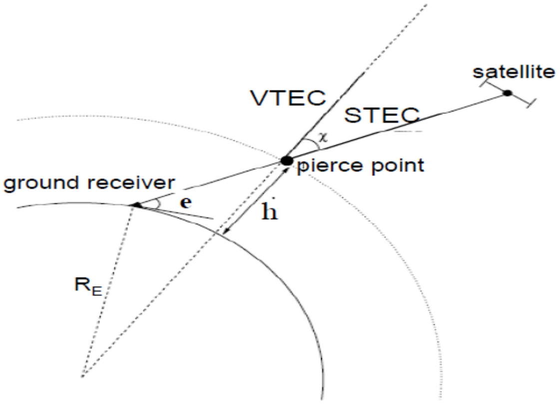

Figure 3.11: Typical geometry for conversion from STEC to VTEC

The conversion usually involves the use of a mapping function as follows:

$$\cos\chi = \frac{VTEC}{STEC} \tag{3.41}$$

$$\Rightarrow \frac{1}{\cos\chi} = \frac{STEC}{VTEC} \tag{3.42}$$

The mapping function is obtained as

$$M(e) = \frac{STEC}{VTEC} = \frac{1}{\cos\chi} = \frac{1}{\sqrt{1-\sin^2\chi}} = \frac{1}{\sqrt{1-\left(\frac{\cos e}{1+\frac{h}{R_E}}\right)^2}} \tag{3.43}$$

where e is the elevation angle of a satellite, h is the ionospheric shell height and R_E is the Earth's mean radius.

3.14 Ionospheric scintillation

The fluctuation in amplitude and phase of signals traversing the ionosphere is known as ionospheric scintillation and can cause signal degradation and, in extreme cases, loss of lock which severely affects the performance of global navigation and communication satellite systems. Ionospheric scintillations occur typically in the post sunset sector especially in the equatorial region **(Wong, 2009).** The amplitude scintillation (S_4) is defined as the normalized uncertainty in the GPS-signal intensity (I).

$$S_4 = \sqrt{\frac{\langle I^2\rangle - \langle I\rangle^2}{\langle I\rangle^2}} \tag{3.44}$$

3.15 IGS and SCINDA

IGS refers to the global system of satellite tracking stations, data centres and analysis centres that provide high quality GPS data, data products online in near real time to meet the objectives of a wide range of scientific and engineering applications and studies. The IGS global network of permanent tracking stations, each equipped with a GPS receiver generates raw orbit and tracking data. The operational data centres, which are in direct contact with the tracking sites, collect raw receiver data then format them into a common standard, using a data format known as Receiver Independent EXchange (RINEX). The formatted data are then forwarded to regional or global data centres. The regional data centres are used to collect data from several operational data centres before transmitting them to the global data centres, to reduce electronic network traffic. Data not used for global analyses are archived and available for online access at regional data centres. The global data centres archive and provide on line access to tracking data and data products.

The SCINDA is a network of ground-based receivers that monitors scintillations at UHF and L-band frequencies caused by electron density irregularities in the equatorial ionosphere. It was established by the Air Force Research Laboratory (AFRL) to provide regional specification and short term forecasts of scintillation to operational users in real time. The GPS-SCINDA was developed to collect high rate GPS measurements with a number of relatively inexpensive and off- the shelf receiver models including the Ashtech Z-12, Ashtech µZ-CGRS, Ashtech Z-xtreme and NovAtel GSV 4004B GPS receivers. All of these receiver models can be operated by a common code with common data output formats. The standardization of data formats is an important step in facilitating usage of the data in space weather products and models. The ionospheric parameters are computed in real time, thereby enabling the use of receiver with high internal data sampling rates at remote stations with low bandwidth connections to the internet.

The GPS-SCINDA system consists of a GPS receiver, a GPS antenna, the GPS-SCINDA data collection software and a computer running on LINUX operating system with access to the internet **(Carrano, 2007).**

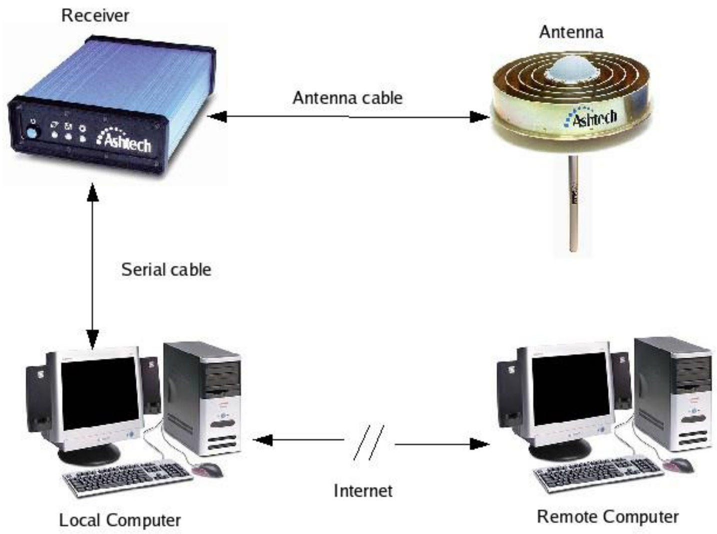

Figure 3.12: Overview of the GPS Data Acquisition System for SCINDA

3.15.1 RINEX processing software

Gopi Krishna Seemala has developed software to process GPS RINEX files in batches. The software is capable of calculating TEC as well as S_4 index from the observation data of the RINEX files and writing ASCII output files (*.CMN & *.STD) in the same directory as the data file. The software also requires RINEX navigation file of the observation data to calculate elevation and azimuth angles of satellites which are needed for the computation of VTEC, the differential code bias (DCB) files provided by the IGS website for the satellite biases **(ftp://ftp.unibe.ch/aiub/CODE/)**.

To process the RINEX file, it can be imported into the software as a command line input or by right clicking anywhere on the software window or by dragging and dropping the data file into the GPS-TEC.exe file.

The output file resulting from the processed RINEX file is in ten columns separated by a tab, which is created in the same folder as the data with filename ‘STATddd-YYY-MM-DD.CMN’. The data contains three header lines as shown below.

Line1: Station_name, Country (OR)

Unknown_station, “path\filename”; (if the station and country are not available).

Line2: Latitude (deg) Longitude (deg)   Altitude (m).

Line3: Jdatet Time PRN Az   Ele   Lat   Lon   Stec   Vtec S_4

(Line 3 is a short description of data columns).

Jdatet is Julian date with fraction of day as time, Time refers to Universal time, Az is the azimuth of the satellite in degrees, Ele is the elevation of the satellite in degrees, Lat and Lon are the sub-ionospheric pierce point latitude and longitude respectively at 350 km altitude. STEC, VTEC and S_4 are the STEC, VTEC and S_4 index (where available) respectively. All columns are separated by a tab. A typical example of such data set for Addis Ababa during some minutes from 0600 Universal time on 1st January, 2009 is as follows:

```
\adis,   ETHIOPIA

9.03514          38.76630         2439.15577

Jdatet                  Time        PRN      Az      Ele     Lat     Lon     Stec    Vtec    S4
2454832.750000          6.000000     1       280.91  19.78   10.31   31.69   28.07   17.15   99.000
2454832.750347          6.008333     1       281.14  19.82   10.33   31.71   28.02   17.14   99.000
2454832.750694          6.016667     1       281.38  19.87   10.36   31.73   28.09   17.18   99.000
2454832.751042          6.025000     1       281.61  19.91   10.38   31.74   28.15   17.22   99.000
2454832.751389          6.033333     1       281.84  19.95   10.41   31.76   28.27   17.29   99.000
2454832.751736          6.041667     1       282.08  19.99   10.44   31.78   28.19   17.26   99.000
2454832.752083          6.050000     1       282.31  20.03   10.46   31.79   28.13   17.25   99.000
2454832.752431          6.058333     1       282.54  20.07   10.49   31.81   28.18   17.29   99.000
2454832.752778          6.066667     1       282.78  20.11   10.51   31.83   28.21   17.31   99.000
2454832.753125          6.075000     1       283.01  20.15   10.54   31.85   28.21   17.33   0.162
2454832.753472          6.083333     1       283.25  20.18   10.56   31.86   28.27   17.36   99.000
2454832.753819          6.091667     1       283.48  20.22   10.59   31.88   28.30   17.39   99.000
2454832.754167          6.100000     1       283.72  20.26   10.62   31.90   28.40   17.45   99.000
```

2454832.754514	**6.108333**	**1**	**283.95**	**20.30**	**10.64**	**31.91**	**28.39**	**17.45**	**99.000**
2454832.754861	**6.116667**	**1**	**284.18**	**20.34**	**10.67**	**31.93**	**28.36**	**17.45**	**99.000**
2454832.755208	**6.125000**	**1**	**284.42**	**20.38**	**10.69**	**31.95**	**28.44**	**17.50**	**99.000**
2454832.755556	**6.133333**	**1**	**284.65**	**20.41**	**10.72**	**31.97**	**28.45**	**17.52**	**99.000**
2454832.755903	**6.141667**	**1**	**284.89**	**20.45**	**10.74**	**31.98**	**28.41**	**17.51**	**99.000**
2454832.756250	**6.150000**	**1**	**285.12**	**20.49**	**10.77**	**32.00**	**28.33**	**17.49**	**99.000**
2454832.756597	**6.158333**	**1**	**285.35**	**20.53**	**10.79**	**32.02**	**28.42**	**17.54**	**0.140**
2454832.756944	**6.166667**	**1**	**285.59**	**20.56**	**10.82**	**32.03**	**28.46**	**17.57**	**99.000**
2454832.757292	**6.175000**	**1**	**285.82**	**20.60**	**10.84**	**32.05**	**28.57**	**17.63**	**99.000**

Any record 99.000 depicts absence of data.

3.16 The geomagnetic field

Electric currents flowing in the fluid outer core of the Earth generate about 90% of the geomagnetic field. Additional contributions come from the ionosphere, the magnetosphere, all the way to the sun.

Figure 3.13 shows the elements of the geomagnetic field **(Macmillan, 2006).**

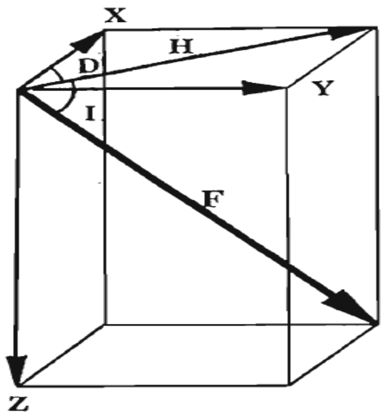

Figure 3.13: Elements of the field vector describing the Earth's magnetic field

The direction of the magnetic field is described by vectors **D** and **I**. **D** indicates the declination between the true north and the magnetic north, measured positive eastwards. **I** indicates, as an angle, how far inclined the field is from the horizontal. The other three independent vectors describe the field intensity**: H, Z** and **F**. The horizontal intensity**, H** defines the horizontal component of the total magnetic field (positive geomagnetic northward) and **Z** defines the vertical component (positive downwards into Earth) which points upward in the southern hemisphere. **F** is the total magnetic field intensity. The horizontal field components can further be divided into **X** (northerly intensity) pointing in the geographic north and **Y** (easterly intensity) pointing in the geographic east.

Some of the elements are geometrically related according to:

$$X = H\cos D \tag{3.45a}$$

$$Y = H\sin D \tag{3.45b}$$

$$\frac{Y}{X} = \tan D \tag{3.45c}$$

Using equations (3.45a) and (3.45b), we can write;

$$H^2\left(\sin^2 D + \cos^2 D\right) = \left(X^2 + Y^2\right) \tag{3.45d}$$

Using the trigonometric identity, $\left(\sin^2 D + \cos^2 D\right) = 1$ in equation (3.45d) we obtain;

$$H = \left(X^2 + Y^2\right)^{\frac{1}{2}} \tag{3.45e}$$

Observers prefer to describe the magnetic field elements using one of two ways: three orthogonal component field directions such that positive values are used for geographic northward, eastward and vertical into the Earth (XYZ) or horizontal magnitude, eastward and vertical into the Earth (HDZ). INTERMAGNET uses the former while MAGDAS uses the latter convention for description of the magnetic field elements. Sample data sets for each convention are as follows.

(i) INTERMAGNET: XYZ convention

```
Format                 IAGA-2002                          |
 Source of Data        University of Addis Ababa                |
 Station Name          Addis Ababa                          |
 IAGA CODE               AAE                              |
 Geodetic Latitude      9.035                            |
 Geodetic Longitude     38.766                            |
 Elevation              2441                          |
 Reported                XYZG                            |
```

```
 Sensor Orientation     HDZF                                   |
 Digital Sampling       1.0 seconds                            |
 Data Interval Type     Average 1-Minute (00:30-01:29)         |
 Data Type              Definitive                             |
 # D-conversion factor  10000                                  |
 # K9-limit             240                                    |
 # This data file was converted from INTERMAGNET CD-ROM/DVD    |
 # Format binary data.                                         |
 # A complete set is available on the INTERMAGNET CD-ROM/DVD.  |
 # Go to www.intermagnet.org for details on obtaining this product. |
 # CONDITIONS OF USE: The Conditions of Use for data provided  |
 # through INTERMAGNET and acknowledgement templates can be found |
 # at www.intermagnet.org                                      |
 # D conversion factor is a fixed value used to allow          |
 # Declination to be converted from minutes of arc to equivalent |
 # nanoteslas. Set to H/3438*10000 where H is the annual mean  |
 # value of horizontal intensity.                              |
DATE       TIME         DOY     AAEX      AAEY      AAEZ      AAEG  |
2009-01-04 00:00:00.000 004     36176.60  1033.90   1599.40    .00
2009-01-04 00:01:00.000 004     36176.70  1034.00   1599.40    .00
2009-01-04 00:02:00.000 004     36176.70  1034.00   1599.50   -.10
2009-01-04 00:03:00.000 004     36177.00  1033.90   1599.50    .10
2009-01-04 00:04:00.000 004     36177.00  1033.80   1599.50    .00
2009-01-04 00:05:00.000 004     36177.00  1033.60   1599.40    .10
2009-01-04 00:06:00.000 004     36177.10  1033.60   1599.50    .10
2009-01-04 00:07:00.000 004     36177.20  1033.50   1599.50    .10
2009-01-04 00:08:00.000 004     36177.20  1033.50   1599.40    .10
2009-01-04 00:09:00.000 004     36176.90  1033.50   1599.30    .00
2009-01-04 00:10:00.000 004     36176.50  1033.60   1599.30    .00
2009-01-04 00:11:00.000 004     36176.30  1033.60   1599.20   -.10
2009-01-04 00:12:00.000 004     36176.20  1033.60   1599.20    .00
2009-01-04 00:13:00.000 004     36176.00  1033.60   1599.20    .00
2009-01-04 00:14:00.000 004     36175.90  1033.50   1599.20   -.10
2009-01-04 00:15:00.000 004     36176.00  1033.20   1599.20    .00
2009-01-04 00:16:00.000 004     36176.20  1032.90   1599.30    .00
2009-01-04 00:17:00.000 004     36176.30  1032.70   1599.30   -.10
2009-01-04 00:18:00.000 004     36176.70  1032.40   1599.30   -.10
2009-01-04 00:19:00.000 004     36177.00  1032.10   1599.40    .00
2009-01-04 00:20:00.000 004     36177.10  1031.80   1599.30    .00
2009-01-04 00:21:00.000 004     36177.20  1031.60   1599.30    .00
2009-01-04 00:22:00.000 004     36177.00  1031.50   1599.30    .00
```

(ii) MAGDAS: HDZ convention

```
      Format              IAGA-2002                            |
Source of Data         Space Environment Research Center, Kyusyu-U  |
Station Name           Nairobi                                 |
```

```
IAGA CODE            NAB (SERC code)                    |
Geodetic Latitude      -01.100                          |
Geodetic Longitude     036.480                          |
Elevation            8888.88                            |
Reported              HDZ                               |
Sensor Orientation     HDZ                              |
Digital Sampling       1 seconds                        |
Data Interval Type     Averaged 1-minute (00:30 - 01:29)           |
Data Type             Provisional                       |
 DATE      TIME          DOY   NABH    NABD    NABZ    NABF
2010-02-18 00:00:00.000 049    83.95    63.14   -79.19  99999.99
2010-02-18 00:01:00.000 049    84.01    63.20   -79.12  99999.99
2010-02-18 00:02:00.000 049    84.30    63.21   -79.00  99999.99
2010-02-18 00:03:00.000 049    84.51    63.14   -78.83  99999.99
2010-02-18 00:04:00.000 049    84.83    63.01   -78.68  99999.99
2010-02-18 00:05:00.000 049    85.41    63.00   -78.38  99999.99
2010-02-18 00:06:00.000 049    85.74    62.87   -78.25  99999.99
2010-02-18 00:07:00.000 049    86.17    62.88   -78.02  99999.99
2010-02-18 00:08:00.000 049    86.41    62.96   -77.93  99999.99
2010-02-18 00:09:00.000 049    86.45    63.01   -77.83  99999.99
2010-02-18 00:10:00.000 049    86.22    63.08   -77.80  99999.99
2010-02-18 00:11:00.000 049    85.97    63.12   -77.90  99999.99
2010-02-18 00:12:00.000 049    85.85    63.09   -77.94  99999.99
2010-02-18 00:13:00.000 049    85.73    62.95   -78.06  99999.99
2010-02-18 00:14:00.000 049    85.78    62.73   -78.08  99999.99
2010-02-18 00:15:00.000 049    86.00    62.58   -77.99  99999.99
2010-02-18 00:16:00.000 049    86.19    62.36   -78.01  99999.99
2010-02-18 00:17:00.000 049    86.32    62.25   -77.87  99999.99
2010-02-18 00:18:00.000 049    86.45    62.27   -77.84  99999.99
2010-02-18 00:19:00.000 049    86.62    62.36   -77.69  99999.99
2010-02-18 00:20:00.000 049    86.70    62.46   -77.62  99999.99
2010-02-18 00:21:00.000 049    86.67    62.54   -77.59  99999.99
2010-02-18 00:22:00.000 049    86.61    62.50   -77.59  99999.99
2010-02-18 00:23:00.000 049    86.54    62.50   -77.59  99999.99
2010-02-18 00:24:00.000 049    86.47    62.54   -77.73  99999.99
2010-02-18 00:25:00.000 049    86.38    62.47   -77.71  99999.99
2010-02-18 00:26:00.000 049    86.39    62.52   -77.69  99999.99
2010-02-18 00:27:00.000 049    86.33    62.52   -77.68  99999.99
2010-02-18 00:28:00.000 049    86.22    62.48   -77.73  99999.99
2010-02-18 00:29:00.000 049    86.16    62.47   -77.77  99999.99
2010-02-18 00:30:00.000 049    86.06    62.46   -77.81  99999.99
2010-02-18 00:31:00.000 049    85.98    62.47   -77.85  99999.99
2010-02-18 00:32:00.000 049    85.99    62.45   -77.87  99999.99
2010-02-18 00:33:00.000 049    86.06    62.48   -77.84  99999.99
2010-02-18 00:34:00.000 049    86.15    62.43   -77.77  99999.99
2010-02-18 00:35:00.000 049    86.32    62.52   -77.70  99999.99
```

A record of value 99999.99 indicates data gap.

3.16.1 Geomagnetic field variations during Quiet Times

The geomagnetic field has a regular variation with a fundamental period of 24 hours, dependent on local time, latitude, season and solar cycle. It is caused by electrical currents in the D and E-regions of the ionosphere where the atmosphere is significantly ionized by the Sun's ultraviolet and X-radiation and the ions are moved by winds and tides arising from the heating effects of the Sun and the gravitational pull of the Sun and the moon.

Quiet time daily field variations can be about $20\,nT$ at mid latitudes and $100\,nT$ at equatorial regions **(Campbell, 2003 p.7).** During quiet times, the H-field becomes large and positive in a very narrow latitude region about the dip equator. This effect is called equatorial electrojet . Using the midnight field levels as baseline (main field position), the equatorial electrojet appears as a large daytime increase in the H-component that maximizes just before local noon. Sometimes, in the morning and/or evening period, depressions of the equatorial field are usually observed. These depressions are credited to the existence of an oppositely directed current called counter-electrojet (CEJ).

3.16.2 Geomagnetic field variations at disturbed times

The geomagnetic field exhibits a deviation from quiet day pattern occasioned by interaction of solar wind and disturbances therein with the geomagnetic field. During geomagnetic disturbances, equatorial ionospheric fields and currents undergo tremendous deviations from their quiet day patterns **(Fejer, 2002)**. The mechanisms responsible for these equatorial electrodynamic effects are prompt penetration of high latitude electric field to lower latitudes

(Nishida, 1968, Gonzales *et al*., 1979) and storm time ionospheric dynamo due to storm time thermospheric winds **(Blanc and Richmond, 1980)**. The amplitude of magnetic disturbances is larger at high latitudes because of oval bands of enhanced currents around each geomagnetic pole called auroral electrojets. Some charged particles get trapped at the boundary of the magnetosphere, and in polar regions, are accelerated along magnetic field lines towards the atmosphere and finally collide with oxygen and nitrogen molecules sometimes resulting in spectacular emissions of mainly red and green light known as aurora borealis at northern latitudes and aurora australis at southern latitudes. The prevailing conditions in the solar-terrestrial environment that result from the emission of charged particles from the Sun and their interaction with the Earth's magnetic field is known as space weather.

Solar-terrestrial disturbance time variations of the geomagnetic field occasionally attain 1000 nT at auroral regions and 250 nT at mid latitudes **(Campbell, 2003 p.8).**

3.17 Geomagnetic storms

A geomagnetic storm is a major disturbance of Earth's magnetosphere that occurs when there is efficient exchange of energy from the solar wind into the space environment surrounding the Earth. These storms result from variations in the solar wind constituents. The solar wind conditions that are effective for creating geomagnetic storms are sustained (for several hours) periods of high-speed solar wind, and most importantly, a southward directed solar wind magnetic field (opposite the direction of Earth's field) at the dayside of the magnetosphere. This condition is effective for transferring energy from the solar wind into Earth's magnetosphere through magnetic reconnection.

The geomagnetic storms recorded by ground-based magnetometers commonly begin with a sudden increase in the *H*-component of the geomagnetic field, called storm sudden commencement (SC) followed by an above normal value of *H* for a few hours known as initial phase, followed by a sudden decrease lasting 4-10 hours called main phase and finally a recovery phase lasting 1 to 2 days **(Rastogi, 2006).** Some storms have only a gradual commencement. The SC is attributed to the sudden increase of the dynamic pressure on the magnetosphere, by plasma ejected from the Sun after a solar flare or by CMEs. SCs are also known to be caused by hydro-magnetic shocks in the solar wind **(Burlaga and Oglivie, 1969).** Initial phase is due to continued solar wind pressure until IMF turns southward when solar wind magnetic field lines merge with magnetospheric field line and the solar plasma gets into the geomagnetic field lines and oscillates between high latitudes simultaneously drifting normal to the field lines. The protons drift westward and electrons eastward causing a westward equatorial ring current at 3 to 5 Earth radii.

During geomagnetic storms, the currents in the ionosphere, as well as the energetic particles that precipitate into the ionosphere add energy in the form of heat that can increase the density and distribution of density in the upper atmosphere, causing extra drag on satellites in low-earth orbit. The local heating also creates strong horizontal variations in the ionospheric density that can modify the path of radio signals (through multiple refractions) and create errors in the positioning information provided by GPS. While the storms create beautiful aurora, they also can disrupt navigation systems such as the Global GNSS and create harmful geomagnetically induced currents (GICs) in the power grid and pipelines as a result of rapid variations in the geomagnetic field, which creates an induced Earth Surface Potential (ESP).

3.17.1 Geomagnetic activity indices

The degree of the geomagnetic field variation serves as a proxy that characterizes the level of disturbance in the magnetosphere and ionosphere. Characterization or indexing is based on a collection of geomagnetic data records. The advantage of indexing is that it helps to sort the geographical data into activity categories. This process further helps one to establish well-defined parameters that enhance the understanding and interpretation of data. Geomagnetic indexing is based on selected time scale variation which is governed by physical quantity driving the variation.

The geomagnetic indices currently in use range from local to global scales. Global indices are derived using data of local indices collected from selected magnetic observatory networks. Some of the geomagnetic activity indices are the K-index, Kp-index, A-index, Disturbance storm time (Dst)-index and Auroral electrojet (AE) index.

(i) The K-index

The principal geomagnetic disturbance index is called the K index obtained from the **H** component of the field (or the D component if it is more disturbed than H) and divides activity into ten levels. The K was selected by Julius Bartels to stand for the word “Kennziffer’’ meaning index of the logarithm of a number **(Campbell, 1997)**. At individual observatories participating in the preparation, an estimated value of the local quiet daily variation is subtracted from the daily records and the range (largest minus smallest) value of geomagnetic activity is determined for each 3-hr UT period. Using a predetermined adjustment to match the statistical occurrences of activity levels among the contributing stations (and some small correction for diurnal and seasonal effects) a 0 (no fluctuations) to 9 (most intense storm) scales value is assigned to the disturbance.

(ii) The Kp- index

Starting 1932, a planetary indication of activity called **Kp-index** has been derived. It is used to indicate the severity of the global magnetic disturbances in near-Earth space. It is based on the average of weighted K indices of 13 ground magnetic field observatories. The values range from 0 (very quiet) to 9 (very disturbed) in 28 discrete steps, resulting in values **of 0, 0+, 1-, 1, 1+, 2-, 2, 2+, …, 9**. On many occasions a level of $K_p \leq 2+$ is usually selected as a quietness level in order to provide enough days to determine the seasonal variation of a phenomenon even during most disturbed years **(Campbell, 2003, p.71).** An estimated Kp is calculated by National Oceanic and Atmospheric Administration (NOAA) in near-real time.

(iii) The A-index

The **A-index** is a 24-hour geomagnetic activity index which is the mean value of the equivalent amplitudes derived from the eight daily 3-hour K indices.

(iv) Disturbance storm time (Dst)

Dst index is a measure of variation in the geomagnetic field due to equatorial ring current. It is computed from H-component at approximately four-near equatorial stations at hourly intervals. At a given time, the Dst index is the average of variation over all longitudes; the reference level set so that Dst is statistically zero on internationally designated quiet days. An index of -50 or deeper indicates a storm- level disturbance. The intensity of geomagnetic storms is often classified based on the value of the minimum Dst as a criterion. For example, **Loewe and Prolss, (1997)**, made a classification as weak ($\leq -30\ nT$), moderate ($\leq -50\ nT$), strong ($\leq -100\ nT$), severe ($\leq -200\, nT$) and great ($\leq -350\, nT$). One minute resolution equivalent of the Dst index is called **symmetric-H (SYM-H)** index.

(v) Auroral electrojet (AE)

AE index is designed to provide a global quantitative measure of auroral zone magnetic activity produced by enhanced ionospheric currents flowing below and within the auroral oval. It is the total range of deviation at an instant of time from quiet day values of the horizontal magnetic field (H) around the auroral oval. The AE index is useful both qualitatively and quantitatively as a correlative index in the coupling between the interplanetary magnetic field and the Earth's magnetosphere.

3.18 Conversion between local time and universal time

When local time (LT) representation is used, the conversion from universal time (UT) is done by considering that the Earth makes one complete rotation in 24 hours. It follows, therefore, that a longitudinal difference of 1° is equivalent to a time difference of 4 minutes. In this regard, the conversion from UT to LT is done according to:

$$LT = UT + \left(\frac{\alpha}{15}\right) \tag{3.46}$$

where α is the geodetic longitude of the station in question.

3.19 Correlation coefficient

When comparing data sets, a quantitative measure to describe the strength of a linear relationship is the correlation coefficient. The correlation coefficient is defined as

$$r = \frac{n\left(\sum_i x_i y_i\right) - \left(\sum_i x_i\right)\left(\sum_i y_i\right)}{\sqrt{\left[n\sum_i x_i^2 - \left(\sum_i x_i\right)^2\right]\left[n\sum_i y_i^2 - \left(\sum_i y_i\right)^2\right]}} \tag{3.47}$$

where n is the number of data points, x_i and y_i are the independent and dependent parameters respectively

CHAPTER FOUR: RESEARCH METHODOLOGY

This chapter gives details regarding the region of study, data sets and procedure used in conducting the study to achieve the stated objectives. Attempts have been made to present the methods precisely with a view to providing other researchers with the ability to replicate the study if need be.

4.1 Region of study and data sets

Geographically speaking, East Africa refers to Kenya, Uganda, Tanzania, Rwanda and Burundi while Eastern Africa refers to Kenya, Uganda, Tanzania, Rwanda, Burundi, Ethiopia, Sudan (South and North) and Somalia. However, in the context of Space Physics, and therefore this thesis, East Africa is used to refer to any country in the African continent whose geomagnetic longitude is east. This includes Ethiopia.

The present study focuses on the East African region, particularly, Addis Ababa, Ethiopia, Nairobi, Kenya and Maseno, Kenya. The data used are for the period between the years 2009 to 2014. The region of study is equatorial where it is well known that the geomagnetic field is nearly horizontally directed North – South **(Campbell, 1989)**, hence more susceptible to for most important electrodynamical phenomena such as EEJ, CEJ and EIA. In addition, the daily geomagnetic field variations, especially during quiet times, normally depend on the local tensor conductivity and the orientation of the main geomagnetic field. The present study analyzed only the H-component of the geomagnetic field.

The data used in the present study were obtained from the owners of magnetic observatories (INTERMAGNET , at Addis Ababa and MAGDAS, at Nairobi) together with corresponding

IGS stations at Addis Ababa (geomagnetic latitude 0.18^0N, geomagnetic longitude110.47^0E) and Nairobi (geomagnetic latitude 10.65^0S, geomagnetic longitude 108.18^0E). The RINEX observation files were downloaded from the Addis Ababa (adis) and Nairobi (rcmn) IGS stations. It is worth noting that acknowledgement of the owners of the data when research paper is published using the data is the necessary and sufficient condition: no other authority is required from the owners of the data.

The data for each station was binned per year. For convenience, Addis Ababa and Nairobi stations are herein denoted by AAB and NAB respectively.

GPS-SCINDA data at Maseno University (geomagnetic latitude 9.64^0S, geomagnetic longitude 108.59^0E) for the high solar activity year 2014 were used. The SCINDA data has an advantage over the IGS data because it provides scintillation index in addition to TEC. Therefore, Maseno data is analyzed separately from the data from AAB and NAB.

All the days with maximum $K_p \leq 2+$ were classified as quiet days while those with maximum $K_p \geq 5$ were classified as geomagnetic storm days. Such days were extracted from the list of K_p index posted by the World Data Centre for Geomagnetism, Kyoto on their website **(http://wdc.kugi.kyoto-u.ac.jp/cgi-bin/kp-cgi)**. To demonstrate the occurrence of geomagnetic storms, the Sym-H and AE index data were extracted from the World Data Center for Geomagnetism, Kyoto. The F10.7 index and IMF-B_Z components in Geocentric Solar Magnetospheric (GSM) coordinates were obtained from the Wind Spacecraft satellite data found in the website of the National Aeronautics and Space Administration (NASA) (**http://omniweb.gsfc.nasa.gov/form/dx1.html).**

The dawn–dusk component of interplanetary electric field (IEF), E_y was computed from the definition of magnetic field.

$$E_y(mV/m) = -B_Z(nT) \times V_X(km/s) \times 10^{-3} \tag{4.1}$$

such that V_X is the solar wind velocity, in Sun-Earth direction, taken from the Wind satellite

The thermospheric O/N_2 ratio, during the storm days and corresponding reference quiet days, was obtained from the Global Ultraviolet Imager (GUVI) instrument onboard Thermosphere Ionosphere Mesosphere Energetics and Dynamics (TIMED) satellite.

4.2 Determination of the mean annual variation of the geomagnetic field as a function of time

The H-component, for each day, from the AAB data was obtained using equation (3.45e).

A quiet level baseline was defined for each day as the arithmetic mean of the geomagnetic field for the first 300 minutes (5hours) starting at local midnight according to:

$$H_0 = \frac{\sum_{s=1}^{300} H_s}{300} \tag{4.2}$$

The usage of these baselines is based on the assumption that the nighttime ionospheric currents are trivial. This assumption is generally accepted based on the fact that the conducting E region of the ionosphere largely disappears at night hours except at the auroral latitudes and currents flowing in the F region of the ionosphere during the night are much smaller in magnitude than the daytime dynamo currents **(Takeda and Araki, 1985, Yamazaki *et al*., 2011)**.

The baseline value for each day was subtracted from each of the one- minute resolution H-field values to get the variation amplitude from the baseline for the particular day. That is;

$$\Delta H_t = H_t - H_0 \tag{4.3}$$

where t = 1, 2,…, 1440 seconds, corresponding to the period 00:00 hour to 23:59 hour. The resulting variation amplitude for any hour is associated with the ionospheric current at that hour (**Rastogi *et al*., 2004**).

During quiet times, the geomagnetic field variation is, theoretically, expected to exhibit a variation pattern similar to that of a periodic function diurnally in such, a way that the value at 00 hr LT should be equal to the value at 24hr LT. However, this may not necessarily be the case. A correction factor, known as non- cyclic variation, should therefore be performed on the data **(Matsutisha and Maeda, 1965, Rastogi *et al*., 2004).** The non-cyclic variation factor was defined as;

$$\Delta_c = \frac{(\Delta H)_1 - (\Delta H)_{1440}}{1439} \tag{4.4}$$

where 1439 is the number of intervals in the data set.

Equation (4.4) can be expressed in the form:

$$(\Delta H)_1 = (\Delta H)_{1440} + 1439\Delta_c \tag{4.5a}$$

Equation (4.5a) implies that in our new arrangement, the first data point will be given by the term on the right hand side, that is,

$$1^{st} = (\Delta H)_{1440} + 1439\Delta_c \tag{4.5b}$$

We make a generalization by reasoning that in equation (4.5b), suppose $t = 1440$, it implies that $1439 = t - 1$ to write a general equation that is representing the quiet daily variation in *H*-component of the geomagnetic field as

$$Sq_t(H) = (\Delta H)_t + (t-1)\Delta_c : t = 1,2,...,1440. \tag{4.6a}$$

The subscript t on the left hand side of equation (4.6a) can be dropped off without loss of generality resulting in the standard form

$$Sq(H) = (\Delta H)_t + (t-1)\Delta_c : t = 1,2,...,1440. \tag{4.6b}$$

The geomagnetic field data from INTERMAGNET and MAGDAS is usually recorded and saved using the .min file extension format. A MATLAB script was written to read the data and use equation (4.6b) to calculate $Sq(H)$ for all the days selected for analysis. For a typical example, the reader is referred to Appendix A.

The average of the monthly, $Sq(H)$, variations for each year was computed. These averages, denoted by $\langle Sq(H)\rangle$ represent mean annual variation of the geomagnetic field during geomagnetic quiet time. The $\langle Sq(H)\rangle$ corresponding to each year was plotted as a function of LT.

The storm time variation of the *H*-component of the geomagnetic field, $Sd(H)$, was obtained by subtracting the baseline (equation 4.2) for a reference quiet day, from the *H*-field values during geomagnetic storm. That is;

$$Sd(H) = H_t - H_0 : t = 1,2,...,1440 \tag{4.7}$$

where H_t is the H-component of the geomagnetic field on storm day.

The perturbation of the storm $(SD(H))$ on quiet time geomagnetic field was determined according to

$$SD(H) = Sd(H) - Sq(H) \tag{4.8}$$

The calculations in equation (4.7) and equation (4.8) were performed by writing scripts in MATLAB.

4.3 Investigation of the annual morphology of total electron content

The RINEX observation files were downloaded from the AAB and NAB, IGS stations for the period, 1st January, 2009 to 31st December, 2015.

Gopi Seemala RINEX processing software version 2.9.3 **(http://seemala.blogspot.com/)** was used to process each station's observation data for each year, giving the desired (.CMN) output files. The CMN files contain data for all visible satellites and elevation angles; hence some values of time are also repeated if more than one satellite passes simultaneously. To obtain accurate data of actual ionospheric parameters above the station, it is important to set the elevation angle high **(Sharma *et al*., 2012, Kumar, 2016)**. This high threshold elevation angle limits the field of view of the GPS receiver hence reducing effects of low elevation angles such as those of multipath and troposcatter due to water vapour. A script was, therefore, written to read each CMN file, select data corresponding to elevation angle greater than or equal to 70° for all satellite pass pseudo random numbers (PRNs) and average duplicate time, giving corresponding unique outputs. The reader may refer to Appendix B for more details about this process.

The mean of all quiet time VTEC for each month as a function of local time was determined per year to obtain the annual mean VTEC for each station.

The effect of the storm on quiet day VTEC was obtained as a percentage using the relation

$$\Delta TEC(\%) = \left(\frac{VTEC_d - VTEC_q}{VTEC_q} \right) \times 100 \tag{4.9}$$

where $VTEC_d$ and $VTEC_q$ denote the VTEC values during storm and quiet times respectively. Equation (4.9) gives the percentage deviation of the reference internationally quiet day *VTEC* from the storm time *VTEC.*

4.4 Investigation of the correlation between geomagnetic field variations and total electron content

The geomagnetic field data had a resolution of 1minute while the RINEX data had a resolution of 30 seconds, MATLAB interpolation process was applied to ensure that only data occurring at the same instants of time are compared with a view to investigating possible correlation. During quiet time, the daytime hours (0600–1800 LT) were categorized into two phases namely, the prenoon (0600-1200 LT) and afternoon (1300-1800 LT) phases. The corrcoef between $VTEC$ and $Sq(H)$ values were computed on all the quiet days from each month based on the prenoon and afternoon phases throughout the period of study. More details are available in Appendix C.

The statistical test for significance (t-test) of the observed correlation coefficients was performed.

4.5. Investigation of the possibility of using $Sq(H)$ as a proxy for TEC

The TEC and geomagnetic field data for the period showing the good correlation was selected and analyzed by use of quadratic fitting with a view to investigating the possibility of using $Sq(H)$ to predict TEC . The relationship was validated by plotting both GPS measured TEC and inferred TEC on the same axes, to demonstrate how well the inferred values compare with the measured values.

CHAPTER FIVE: RESULTS AND DISCUSSIONS

The present chapter presents the detailed results of the study. The findings obtained are discussed and explanations as to whether they support or contradict other studies have been provided.

5.1 Mean annual variation in the quiet time geomagnetic field

The $Sq(H)$ variation for each quiet day in the entire year was calculated using equation (4.6b). The mean annual variation, $\langle Sq(H)\rangle$, of the geomagnetic field is the average of the $Sq(H)$ variations for the year. The annual $\langle Sq(H)\rangle$ as a function of LT for Addis Ababa and Nairobi stations for the years 2009, 2010, 2011, 2012, 2013 2014 and 2015 are presented in Figure 5.1 a, b, c, d, e , f and g respectively.

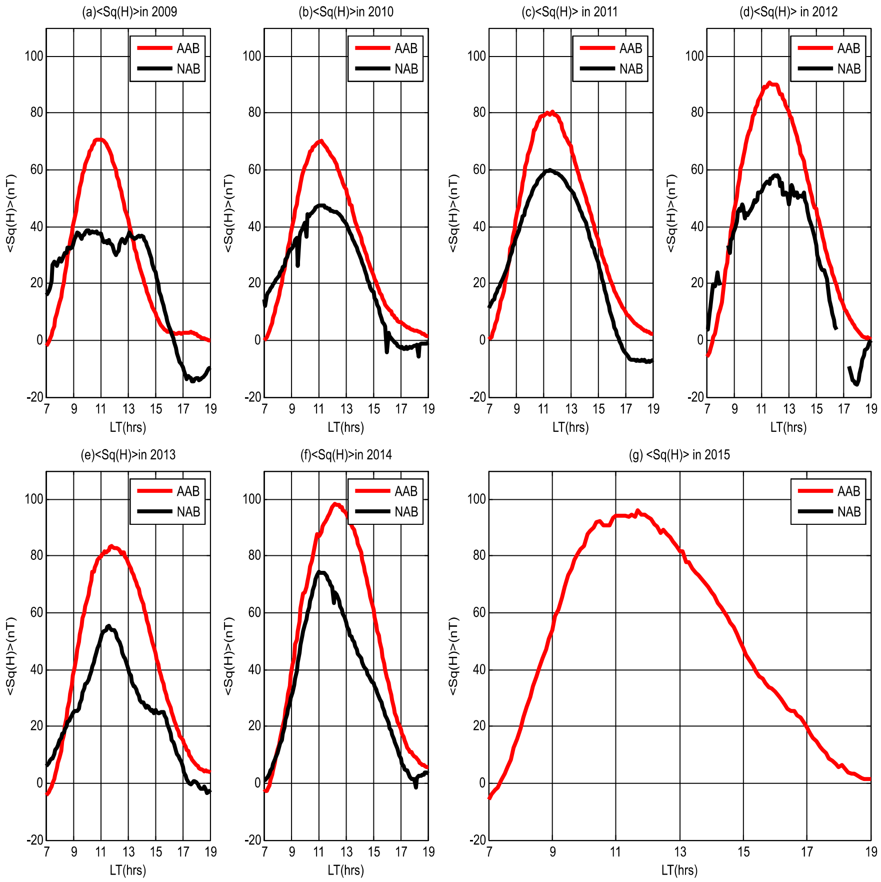

Figure 5.1: Mean annual Sq (H) as a function of day time LT for the years 2009 to 2015.Nairobi data for the year 2015 was missing, hence not shown.

Since Sq is an E-region (which diminishes during the local nighttime) current, the analysis shown in the aforementioned Figure was done strictly for local daytime hours. In Figure 5.1 a, b, c, d, e, f and g, we note that the amplitude of mean annual variation $\langle Sq(H) \rangle$ of the geomagnetic field shows a clear dependence on local time of the day at AAB and NAB stations.

At AAB, $\langle Sq(H) \rangle$ increases from about $0\ nT$ in the morning (around 0700 LT) attaining maximum values around 1100LT during low solar activity years (2009, 2010, 2011 and 2015) and 1200LT during high solar activity years (2012, 2013 and 2014), then decreases attaining values of about $0\ nT$ in the evening at around 1700 LT. In Figure 5.2, are plotted the yearly mean Sunspot number from the year 2009 to 2015.

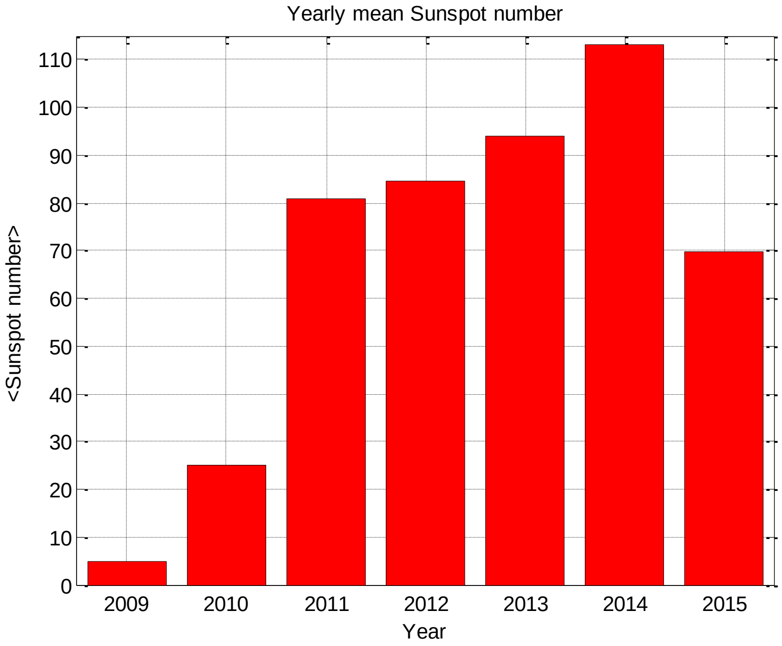

Figure 5.2: Yearly mean Sunspot number from the year 2009 to 2015

At NAB, $\langle Sq(H)\rangle$ increases from about $0\ nT$ in the morning (around 0700 LT) attaining maximum values around 1130 LT; then decreases attaining values around $0\ nT$ in the evening at around 1700 LT during the entire period of study (2009-2014). The maximum amplitude of $Sq(H)$ appears before local noon in the range between 1030 LT to 1130 LT during minimum sunspot years, around dip equatorial regions, and around local noon during maximum sunspot years **(Rastogi and Iyer, 1976, El Hawary *et al.* 2012)**. One of the explanations suggested by **Rastogi and Iyer, (1976)** for maximum $Sq(H)$ occurring well before noon is that, since $Sq(H)$ represents currents in the ionosphere and current being a product of electron density, n_e, electronic charge, e, and charge drift velocity, v, would be maximum at some point between the time of maximum electron density and drift velocity. The electron density maximizes close to noon while the charge drift velocity (hence the electric field) becomes maximum near 0900 to 1000 LT. It follows that the product (current) should maximize around 1100 LT. However, with increasing solar activity (sunspot number), the electron density is known to increase by 50% or more; whereas the electron drift velocity remains constant or decreases. Thus the product of n_e and v should shift to a later time near noon in high sunspot years.

Solar heating and ionization rates are important causes of $Sq(H)$ at all latitudes. This accounts for the minimal values (around $0\ nT$) of $<Sq(H)>$ observed at AAB and NAB in the morning and evening hours, owing to low solar intensity at these hours. The amplitude of maximum $\langle Sq(H)\rangle$ at AAB is consistently higher than the amplitude of maximum $\langle Sq(H)\rangle$ at NAB. This difference is attributed to the existence of the equatorial electrojet that intensifies just before local noon close to the geomagnetic equator (such as at AAB); hence imposing onto the $Sq(H)$ current system. The amplitude of $\langle Sq(H)\rangle$ at NAB is consistently higher than the amplitude of

$\langle Sq(H) \rangle$ at AAB in the morning hours between 0700-0800 LT. This difference is possibly due to the existence of a counter electrojet, a westward electric field close to the dip equator (such as at AAB) in the morning and/or evening hours; that tends to reverse the direction of the $Sq(H)$ current system.

The maximum amplitude of $\langle Sq(H) \rangle$ increases as solar activity increases. The maximum increase occurs between low solar activity year (2009) and high solar activity year (2014), with about 50% and 75% for AAB and NAB respectively.

5.2 Geomagnetic field variation during geomagnetic storms

To study the simultaneous effects of geomagnetic storms on VTEC and *H*-field, we selected two moderate storms: one occurring during a low solar activity period (2011) and the other occurring during a high solar activity period (2014) of the solar cycle 24. A striking feature in the two storms is that they took place in the same season (month). The details of the variations of the geomagnetic parameters during the two storms (6th April, 2011 and 12th April, 2014) are discussed in the following subsections.

5.2.1The storm of 6th April, 2011

A detailed description of the storm is supported by the graphical plots of symmetric-H index, the IMF B_Z, eastward component of the IEF E_y and AE-index shown in Figure 5.3. Variation of $Sym-H$, SC occurred around 10:00 UT (13:00 LT) on 6th April, 2011. The main phase followed immediately and persisted until around 18:00 UT (21:00 LT) when $Sym-H$ attained its minimum value ($Sym-H_{\min} \sim -60 \ nT$) marking the end of the main phase. The recovery phase started at around 19:00UT, increasing with the increase in $Sym-H$ and resumed quiet time level on 7th April, 2011 around 22:00 UT. IMF B_Z and IEF E_y are 180^0 out of phase. When IMF B_Z is southward, IEF E_y is eastward. Nevertheless, when IMF B_Z is northward, IEF E_y is westward. A positive enhancement in the IEF E_y corresponding to an enhancement of southward directed IMF B_Z is strongly related to the initiation of storm activity and that the establishment of a negative (or less positive) IEF E_y in the course of a storm is attributed to the start of the recovery phase. These results are consistent with those in the works of **Rastogi, (2006)**.

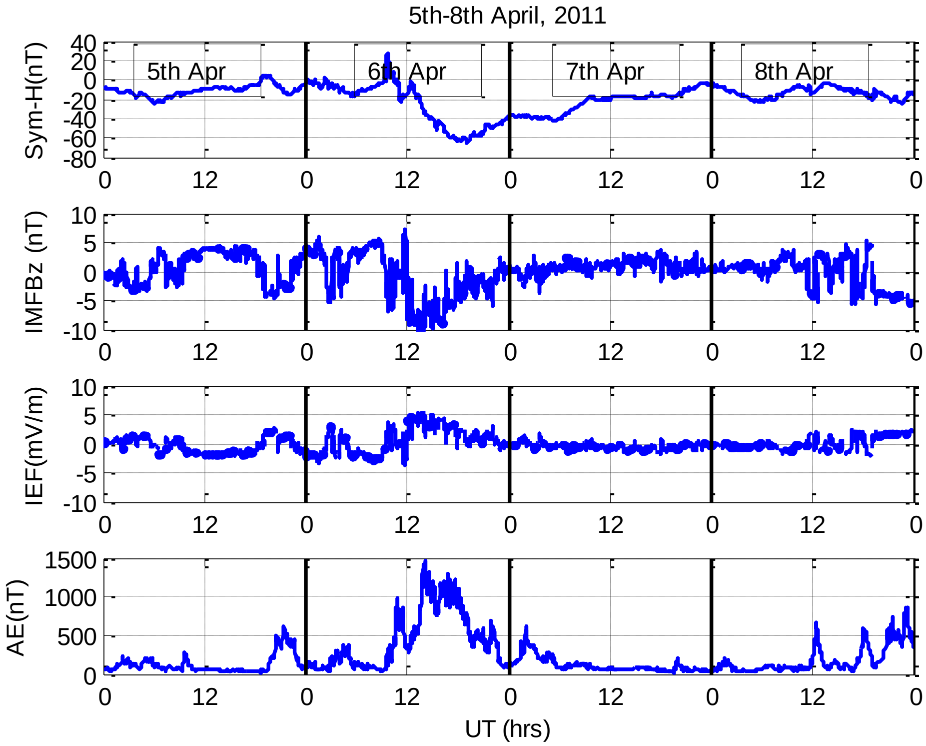

Figure 5.3: Variation of Sym-H index, IMF Bz, IEF Ey and AE index for the period 5th-8th April, 2011.

The variation in AE-index is in phase with the variation in IEF E_y. The enhancements of AE-index suggest the generation of heating energy at high latitudes during the storm, with the ability of launching equatorward surges and winds which may create a disturbance dynamo electric field (DDE) at mid-to- low latitudes. DDE is westward during daytime and eastward during nighttime **(Zhao *et al.* 2005).** The westward sym-H , southward IMF B_Z and enhanced Auroral electrojet on 6th April, 2011 are clear manifestations of the geomagnetic storm.

Figure 5.4 shows the variation of the H-component of the geomagnetic field on a reference quiet day (21st April, 2011) and days before, during and after the storm period for 5th – 8th April, 2011 for AAB and NAB stations. During the reference quiet day, the peak amplitude of $Sq(H)$ at AAB is larger than the peak amplitude of $Sq(H)$ at NAB. This difference is attributed to the existence of the equatorial electrojet that intensifies just before local noon close to the geomagnetic equator (such as at AAB); hence imposing onto the $Sq(H)$ current system. The equatorial electrojet is caused by enhancement of the effective conductivity at the geomagnetic equator. However, the morning $Sq(H)$ at NAB are greater than the corresponding values at AAB; attributed to the morning counter electrojet that acts to reverse the $Sq(H)$ current system closer to the geomagnetic equator **(Omondi *et al*., 2016).** Being quiet days before and after the storm respectively, the $Sq(H)$ variation on 5th April, 2011 and 8th April, 2011 show an excellent correlation with the corresponding variation on the reference quiet day (21st April, 2011).

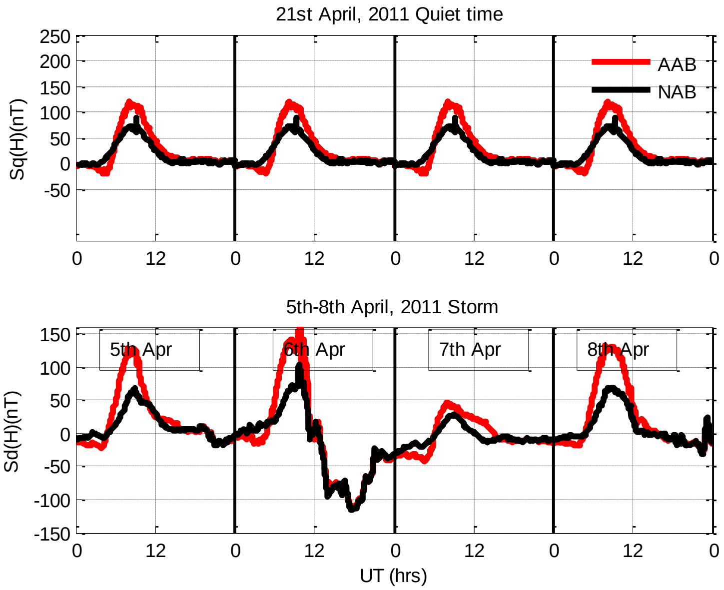

Figure 5.4: Geomagnetic field variation on a reference quiet day (21st April, 2011, top panel) and storm period (5th-8th April, 2011, bottom panel). Quiet day shows a regular diurnal variation while the storm day shows a perturbation in the geomagnetic field variation caused by the ring currents.

The storm time variation in the *H*-component of the geomagnetic field is observed to begin on 6th April, 2011, around 08:00 UT with a strong positive impulse, above quiet time values, attributed to SC. After the SC, $Sd(H)$ drops rapidly, attaining minimum value ($Sd(H)_{\min} \sim -110\, nT$) at both stations. This variation corresponds to the main phase of the storm. It is interesting to note that during the main phase, the geomagnetic field variation at both stations have equal values. This suggests that global effects due to equatorial ring currents cancel local effects during the main phase of the storm. After attaining minimum values, $Sd(H)$ starts increasing slowly (recovering), attaining zero value on 7th April, 2011. The storm time variations are important at mid-to-low latitudes due to the deformations of the pattern of ionospheric currents and induced currents during this period **(Rastogi *et al.* 2004).** Figure 5.5 shows the difference between the geomagnetic field variation on the reference quiet day and the period flanking the day of the storm, herein referred to as the perturbation of the storm, $SD(H)$.

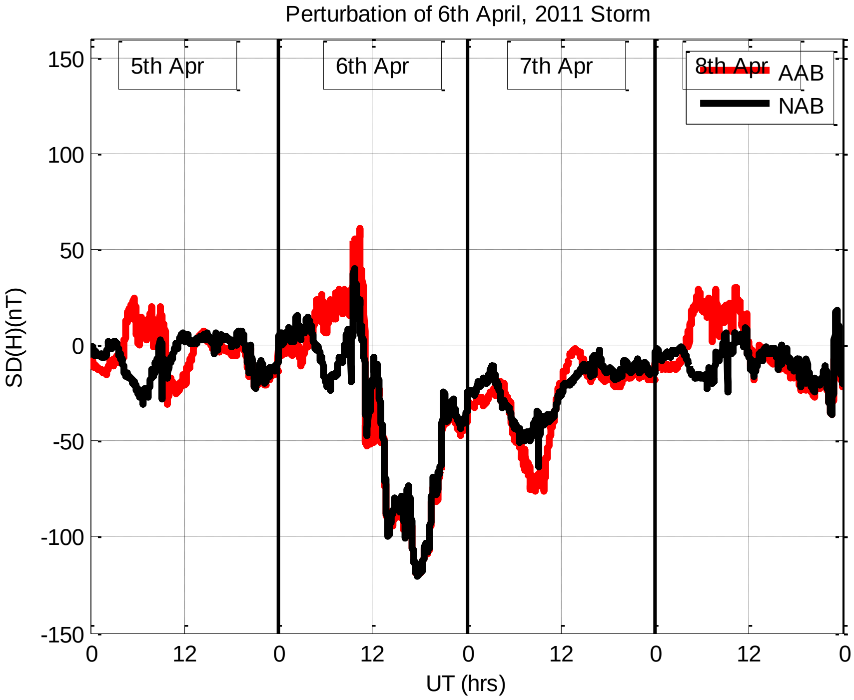

Figure 5.5: Perturbation of the storm during the period 5th-8th April, 2011. The effect of the geomagnetic storm during the main phase on 6th April, 2011 is independent of the geomagnetic latitude of the station.

From Figure 5.5, the values of $|SD(H)|$ before and after the storms are less than the corresponding values during the storms. The fact that these values before and after the geomagnetic storms are mainly non-zero is attributed to the existence of day-to-day variation of solar quiet currents. The perturbation is greatest during the main phase of the storm. This is caused by the westward (anti-Sq) electric field generated by persistent or slowly varying southward IMF-B_Z. The variation of $SD(H)$ is consistent with the variation of $Sym-H$ index.

5.2.2. The storm of 12th April, 2014

Figure 5.6 shows the variation of $Sym-H$ index, IMF B_Z, IEF E_y and AE-index during the period 11th-14th April, 2014.

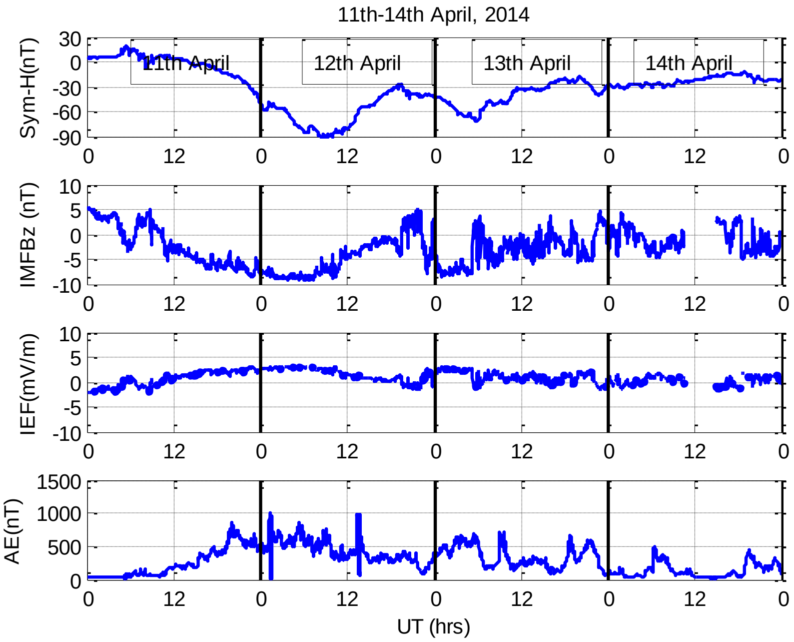

Figure 5.6: Variation of Sym-H index, IMF Bz, IEF Ey and AE index for the period 11th-14th April, 2014. The main phases of the storms occurred on 12th and 13th April, 2014 as shown by maximum westward Sym-H values < -50 nT , southward IMF B_Z and enhanced AE.

From the variation of $Sym-H$, it is evident that two successive sudden commencements of storms occurred around 06:00 UT on 11th April, 2014 and 18:00 UT on 12th April, 2014. The main phase started at around 12:00 UT on 11th April, 2014 with decrease in $Sym-H$ index until around 11:00 UT on 12th April, 2014 when $Sym-H$ index attained its minimum value ($Sym-H_{\min} \sim -90\ nT$), marking the end of the main phase. After 11:00 UT on 12th April, 2014, the recovery phase started but the $Sym-H$ index did not increase to quiet time level. A second storm occurred at around 21:00 UT on 12th April, 2014 attaining minimum $Sym-H$ excursion

($Sym-H_{min} \sim -70\ nT$) on 13th April, 2014. The $Sym-H$ index resumed to its quiet time level at around 01:00 UT on 14th April, 2014. Analogous to the 6th April, 2011 storm, IMF B_Z and IEF E_y are 180^0 out of phase. When IMF B_Z is southward, IEF E_y is eastward. Nevertheless, when IMF B_Z is northward, IEF E_y is westward. The variation in AE-index is in phase with the variation in IEF E_y.

Figure 5.7 shows the H-field variation on a reference quiet day (27th April, 2014) and days before, during and after the storm period for 12th – 13th April, 2011 for AAB and NAB stations.

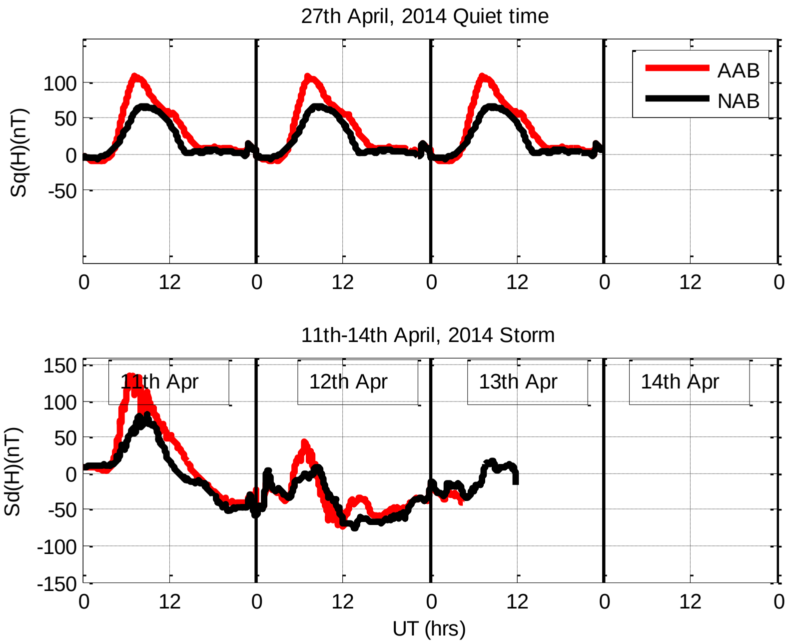

Figure 5.7 Geomagnetic field variation on a reference quiet day (27th April, 2014) and storm period (11th-13th April, 2014)

Irregular variation in the H-component of the geomagnetic field is observed to begin on 12th April, 2014 at around 01:00 UT accompanied by successive enhancements. The $Sd(H)$ then decreases rapidly, attaining minimum value ($Sd(H)_{\min} \sim -70\ nT$) at both stations. This variation corresponds to the main phase of the storm. Again in this case occurrence of equal minimum values of $Sd(H)$ at both stations suggest that global effects due to equatorial ring currents cancel local effects during the main phase of the storm.

Figure 5.8 illustrates the perturbation of the storm, $SD(H)$, obtained by using equation (4.8).

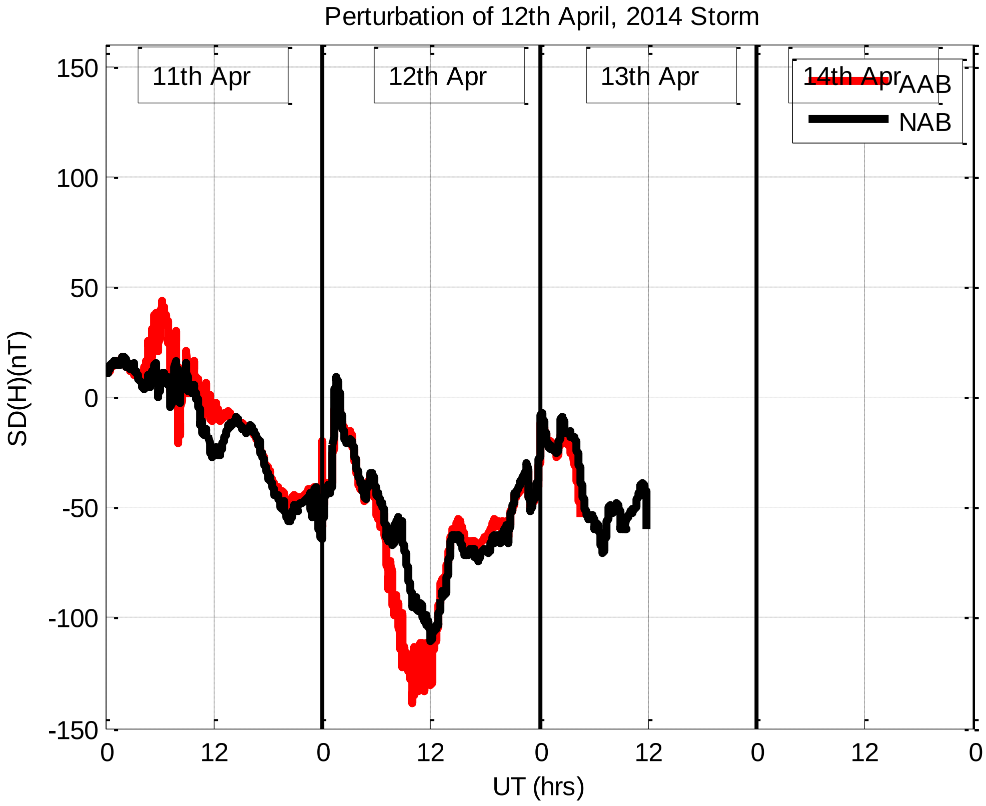

Figure 5.8: Perturbation of the storm during the period 11th-13th April, 2014

The greatest perturbation is observed during the main phase of the storm and is attributed to westward electric field generated by slowly varying southward IMF- B_Z. Again, the variation of $SD(H)$ is consistent with the variation of $Sym-H$ index. The geomagnetic field variation during geomagnetic storms has deviated from the quiet time pattern due to the irregular perturbation electric fields that are imposed by the geomagnetic storms. The geomagnetic storms have generally resulted in a depression of the mean H-field variation relative to the quiet time mean H-field variation. Based on numerical analyses, **Blanc and Richmond (1980),** suggested that the global distribution of ionospheric currents and electric fields can be altered by the perturbations in the solar wind-magnetosphere dynamo and ionospheric wind dynamo. Such modifications in the neutral atmospheric circulation during geomagnetic disturbances are capable of decreasing or even reversing the quiet time electric field pattern in the vicinity of the dip equator. Short period fluctuations in $\boldsymbol{H}$ related to directional changes in the $\boldsymbol{B_Z}$ component of the interplanetary magnetic field also occur at equatorial stations during geomagnetic storms **(Chandra and Rastogi, 1997).**

5.3 Annual morphology of quiet time VTEC

5.3.1. VTEC variation over Addis Ababa and Nairobi

The mean of all quiet time VTEC for each day as a function of local time was determined per year to obtain the annual mean VTEC for each station. The results are displayed in Figure 5.9a, b, c, d, e, f and g. The variation of mean VTEC as a function of local daytime in 2013 is incomplete due to the numerous data gaps during the year.

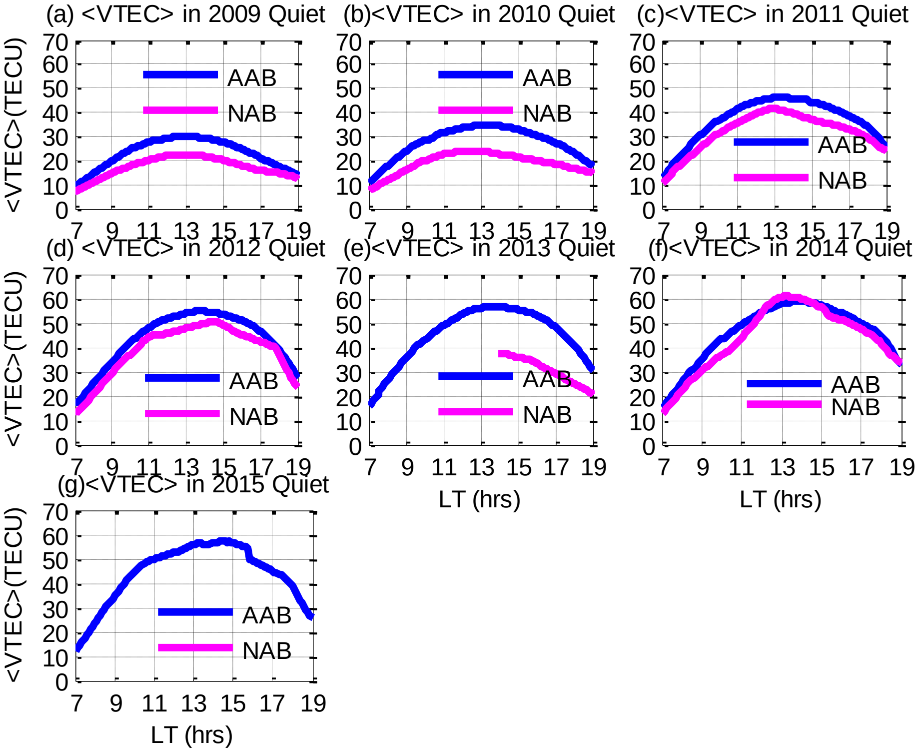

Figure 5.9: Quiet time mean VTEC from 2009 to 2015.

The $<VTEC>$ increases from morning (0700 LT) attaining maximum values around afternoon (1300 LT), then decreases gradually towards sunset (1900 LT) at both stations during the entire period of study. These results are consistent with those of previous research in this region **(Olwendo *et al.*, 2012b, Oron *et al.*, 2013, Oryema *et al.*, 2015)**. The gradual increase of VTEC to a maximum value during the noon to afternoon hours of the day is attributed to photo-ionization by extreme ultraviolet radiation. During the day, as solar intensity increases, the rate of ionization increases beyond the recombination rates of ionized particles; hence increasing VTEC. However, towards sunset, the primary source of ionization (solar radiation) diminishes allowing for recombination rates to exceed the ion production rates, hence the gradual decrease in VTEC.

The magnitude of peak $<VTEC>$ increases linearly with increase in solar activity. The approximate peak values at AAB were 30, 32, 46, 55, 57 and 60 TECU in 2009, 2010, 2011, 2012, 2013 and 2014 respectively while the approximate peak values at NAB were 21, 23, 40, 50 and 62 TECU in 2009, 2010, 2011, 2012 and 2014 respectively. This increase in ionization suggests addition of extra sources of ionization during high solar activity such as impact ionization due to collision of ion-neutral particles arising from intense energy input from the Sun to the ionosphere.

The peak $<VTEC>$ at NAB is less than the peak $<VTEC>$ at AAB during the low solar activity year, 2009. However, this difference decreases with increase in solar activity until the high solar activity year, 2014 when the peak $<VTEC>$ at Nairobi exceeds the peak $<VTEC>$ at Addis Ababa. The day light $\left(\vec{E}\times\vec{B}\right)$ drift of plasma lifts plasma to higher altitudes. The uplifted plasma then diffuses downward along geomagnetic field lines higher latitudes away from the geomagnetic equator under the influence of gravity and pressure gradients creating the EIA characterized by a depression in ionization (trough) at the geomagnetic equator and two peaks (crests) on either side of the geomagnetic equator at about 15° to 20°. The fact that AAB and NAB are closer to the geomagnetic equator and southern crest of the equatorial ionization anomaly respectively, suggests that the Lorentz force responsible for the uplifting of plasma is weak during low solar activity, but increases linearly with increase in solar activity attaining maximum value during solar maximum.

5.3.2 VTEC and S_4 variation over Maseno

It is important to note here, that Maseno a SCINDA station's ionospheric dynamics is being discussed separately from AAB and NAB. This is because, the data from the station provide amplitude scintillation and TEC and it would be interesting to evaluate the relationship between the parameters. Moreover, the station was only operational from the year 2012 and only data for the year 2014 has been found to have good quality.

Figure 5.10 shows the diurnal variation of VTEC and S_4 during geomagnetic quiet time for all the months of the year 2014.

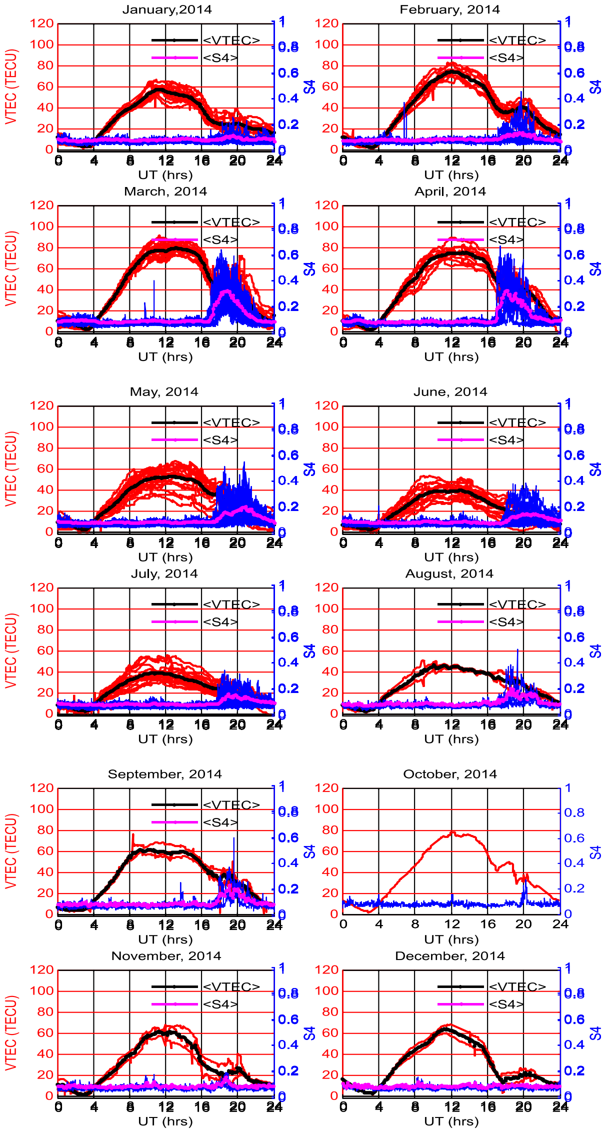

Figure 5.10: Diurnal variation of VTEC at Maseno, plotted on the left hand y-axis, together with the monthly average values <VTEC> and S4 index, plotted on the right-hand y-axis, with the monthly average values <S4>.

VTEC attains minimum values about 0300UT (0600 LT), then increases steadily attaining maximum values between 1000UT (1300 LT) and 1200 UT (1500 LT) throughout the year, consistent with results of **Olwendo *et al*. (2012b)**. The increase in VTEC during the day time to maximum is attributed to the corresponding increase in photo-ionization rates by the Extreme Ultraviolet radiation (EUV) and upward $\vec{E} \times \vec{B}$ plasma drift velocity. After attaining peak values, VTEC values decrease gradually, to smaller values towards evening hours, mainly due to the decrease in photo-ionization. Nighttime enhancements of VTEC occurred in January, February, March, April, May, September, October, November and December. The greatest enhancements were observed in March and April. These post sunset enhancements have been attributed to the 'fountain effect' in which the $\vec{E} \times \vec{B}$ drift uplifts ionospheric plasma at the geomagnetic equator, then the plasma diffuses to higher latitudes through the influence of gravity and pressure gradients **(Anderson *et al*. 2006, Bhattacharya *et al.* 2009).** The eastward electric field during the daytime produces upward motion of ionospheric plasma, hence the northward motion of ionization crest while the westward electric field during night results in downward motion of plasma, hence southward motion of ionization crest. This southward motion of plasma may be the one responsible for the nighttime enhancement in VTEC.

Sufficient amplitude scintillation, $S_4 > 0.2$, (**D'ujanga *et al*. 2012**) were observed in the local post sunset sector during the months of February, March, April, May, June, July, August, September and October and the greatest values occurred in March and April. The S_4 index is correlated with VTEC depletions. The correspondence of VTEC depletions with increase in S_4 index is in conformity with results from previous researchers **(Dashora and Pandey, 2005, Seemala and Valladares, 2011).** These depletions are attributed to density irregularities and are manifested in ionospheric scintillations. Ionospheric scintillations are capable of causing fading of trans-ionospheric signals, causing threat to communication and navigation systems.

Figure 5.11 illustrates the seasonal variation of mean VTEC and mean, S_4 over Maseno during geomagnetic quiet time. The largest diurnal maxima in mean VTEC occurred in March equinox and the smallest during the June solstice while September equinox and December solstice have equal peaks. The greatest mean post sunset scintillations occurred in March equinox while the least occurred in December solstice. The high VTEC values are attributed to high solar EUV radiation during the season, responsible for photo-ionization

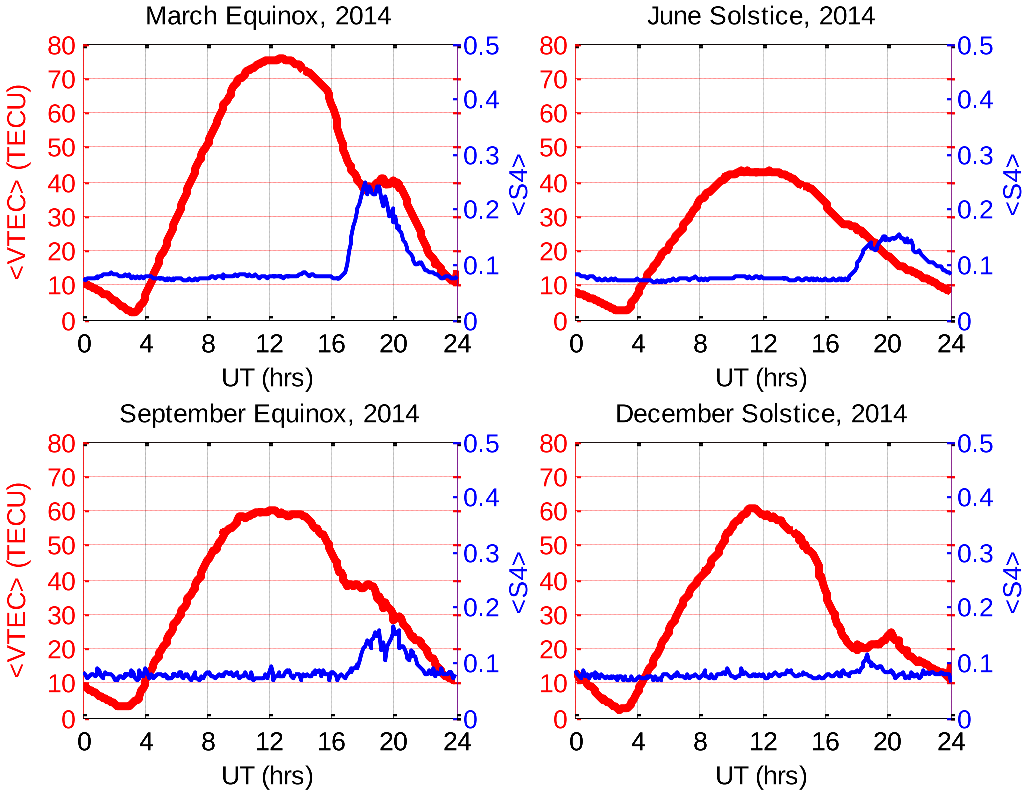

Figure 5.11: Seasonal variation of mean VTEC, plotted on the left hand y-axis, and mean S_4, plotted on the right hand y-axis, over Maseno

5.4 Morphology of storm time VTEC

5.4.1 VTEC variation during the 6th April, 2011storm

Figure 5.12 shows the VTEC variation for the days before, during and after the storm period for 5th-8th April, 2011 for AAB (top panel) and NAB (bottom panel). NAB had gaps in data on 7th and 8th April, 2011.

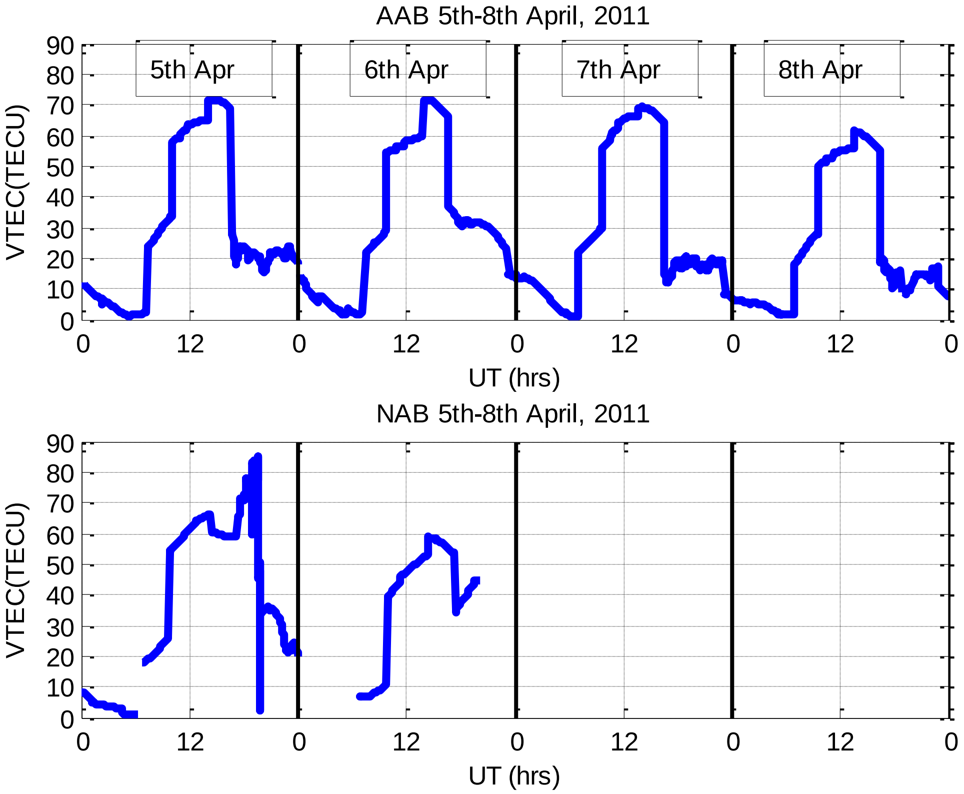

Figure 5.12: Variation of VTEC at Addis Ababa and Nairobi during the period 5th-8th April, 2011

During the main phase of the storm, on 6th April, 2011, enhancement in VTEC is observed at both stations around the time of $Sym-H_{\min}$ as well as instants of occurrence of minimum values of $Sd(H)$ and $SD(H)$, depicting a good correlation between VTEC variation and geomagnetic field variation. Figure 5.13 and Figure 5.14 provide the percentage change in VTEC $(\Delta TEC(\%))$

with respect to the VTEC of the reference most internationally quiet day (21st April, 2011), calculated using equation (4.9). The black horizontal lines mark the zero level of $\Delta TEC(\%)$.

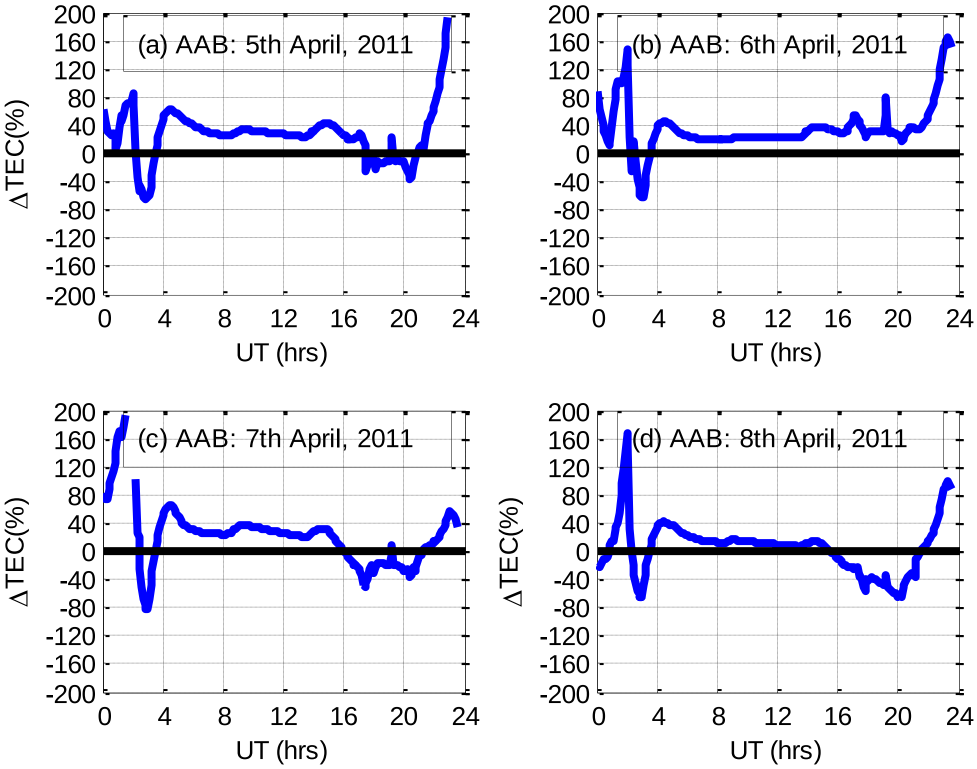

Figure 5.13: $\Delta TEC(\%)$ at Addis Ababa station during 5th-8th April, 2011

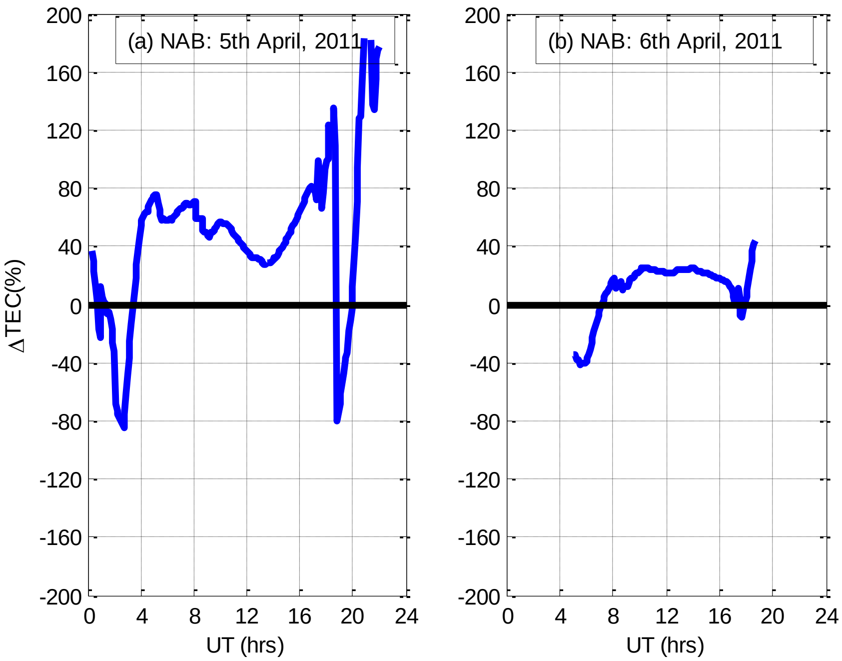

Figure 5.14: $\Delta TEC(\%)$ at Nairobi station during 5th and 6th April, 2011

Figure 5.13, shows that the maximum enhancement above the reference quiet day values at AAB was around 40% while Figure 5.14 shows that the maximum enhancement during the same period at NAB was around 30%. During the recovery phase of the storm on 7th April, 2011, successive enhancements reaching 160% and depressions up to 80% occur between 00:00 UT and 04:00 UT at Addis Ababa. The variation then remains approximately constant about 40% above the quiet time values until 16:00 UT when another depression occurs lasting for 4 hours. At 20:00 UT, the VTEC begins to increase above quiet time values again.

5.4.2 VTEC variation during the 12th April, 2014 storm

Figure 5.15 shows the variation of VTEC at AAB and NAB stations for the period 11th-14th April, 2014. The enhancements in VTEC at around 17:00 UT are observed at AAB on 11th, 12th and 13th April, 2014. Further, the least peak value of VTEC at AAB is seen on the storm day.

However, at NAB, the peak values of VTEC take an increasing trend with 11th April, 2014 having the least peak value.

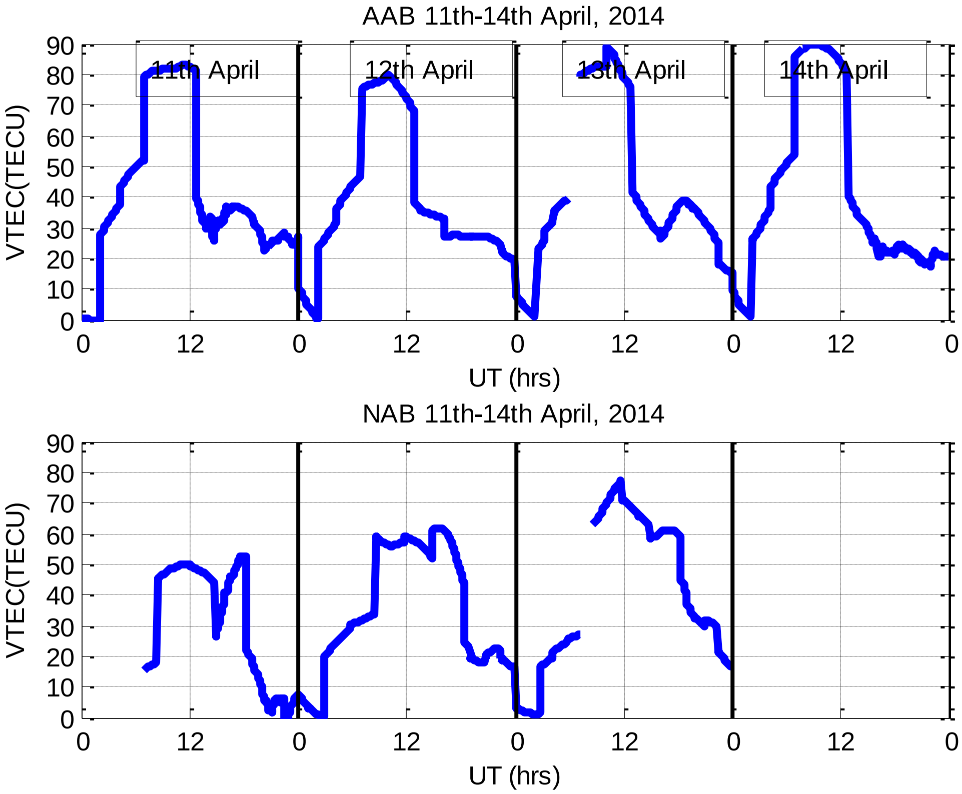

Figure 5.15: Variation of VTEC at Addis Ababa and Nairobi during the period 11th-14th April, 2014

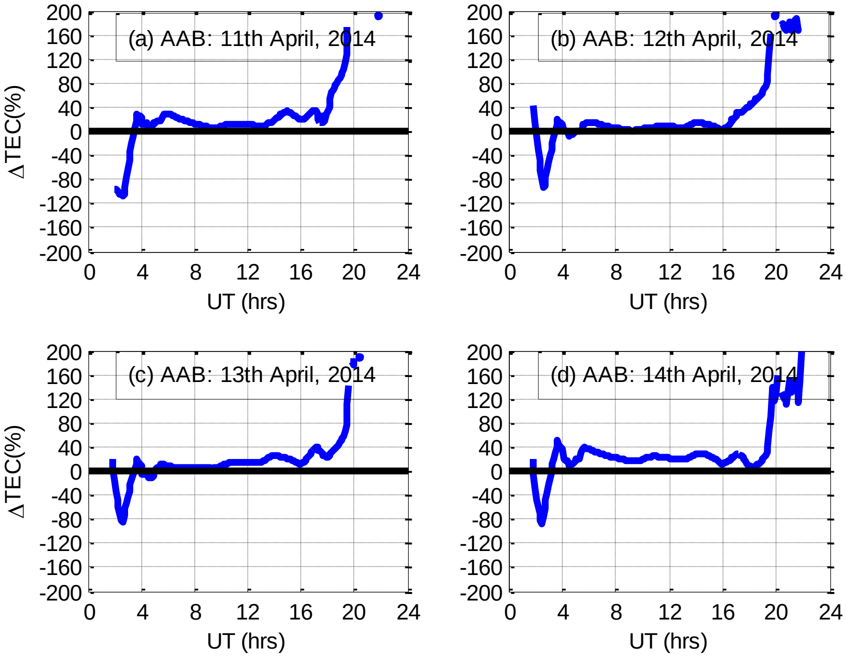

Figure 5.16: $\Delta TEC(\%)$ at Addis Ababa station during 11th-14th April, 2014

Figure 5.16 and Figure 5.17 show the percentage change in VTEC from the reference quiet day's VTEC at AAB and NAB respectively.

At AAB, the VTEC undergoes a depletion of about 80% around 02:00 UT, after which it follows the variation of quiet time VTEC until around 16:00 UT on the storm day (12th April, 2014) and around 18:00 UT on the other days before and after the storm when enhancements reaching 160% are observed.

At Nairobi (Figure 5.17), there are sharp depressions, representing negative ionospheric storm effects, in VTEC (80%) around 03:00 UT on 12th and 13th April, 2014. After this, VTEC begins to increase until 04:00 UT when it starts to approximately follow the variation of the quiet time VTEC. At 16:00 UT VTEC increases rapidly beyond the quiet day values by about 40% on the storm day. On the days before and after the storm, these enhancements are observed to occur gradually at around 18:00 UT reaching about 60% on 11th April, 2014 and 120% on 13th April, 2014. NAB had gaps in data on 14th April, 2014.

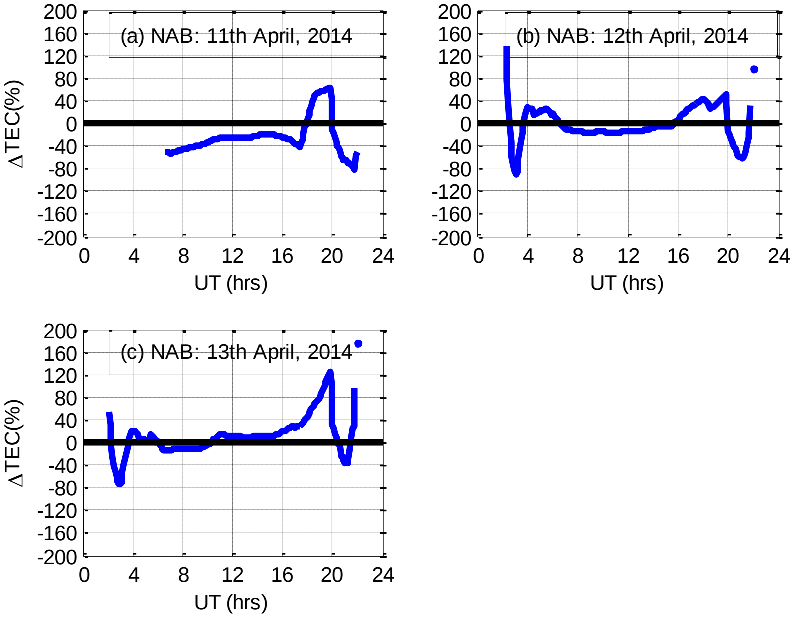

Figure 5.17: $\Delta TEC(\%)$ at Nairobi station during 11th-13th April, 2014. The black horizontal line represents the zero level. Positive values occur when the quiet time VTEC is less than the storm time VTEC (positive ionospheric storm).

The post sunset enhancements observed in VTEC in the present study cannot fully be related to the impacts of geomagnetic storms since they also exist during geo-magnetic quiet conditions. At NAB, closer to the EIA, multiple peaks of VTEC are observed on 12th April, 2014 and may be attributed to combined effect of penetration electric field and modified fountain effects consistent with the findings of **Chakraborty *et al.* (2015)**.

To validate the variations in VTEC during the 6th April, 2011 storm period; the GUVI thermospheric O/N_2 ratio has been used. Figure 5.18 shows the global O/N_2 maps during storm (6th April, 2011) and a reference quiet day (21st April, 2011). The O/N_2 ratios on storm day are greater than the corresponding values on quiet day. The magnitude of O/N_2 ratio is the same at both stations (AAB and NAB), confirming the nearly similar effects of the storm on TEC at these stations.

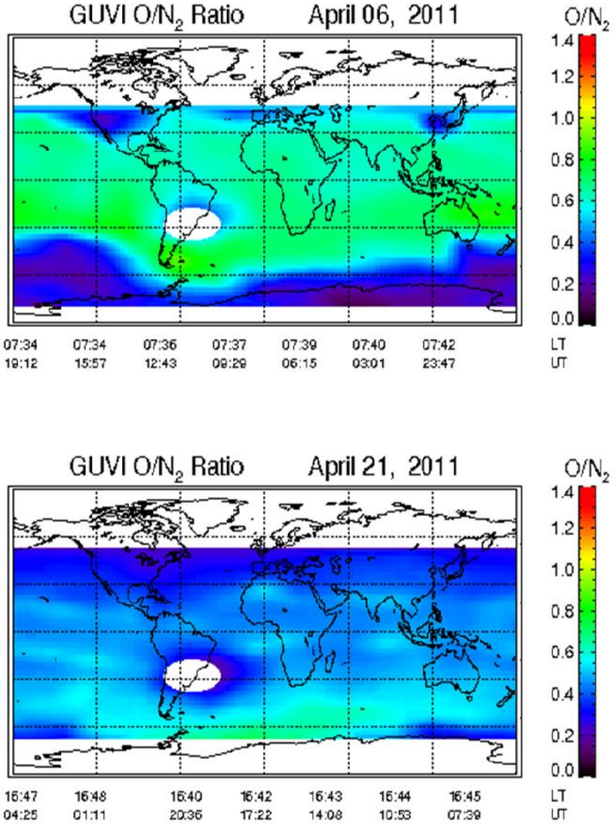

Figure 5.18: The map of thermospheric O/N_2 ratio on a storm day (6th April, 2011) and a quiet day (21st April, 2011).

During the two storms presented in this thesis, the enhancement (maximum up to 160% at AAB and NAB) and depression (maximum up to -80% at AAB and NAB) in VTEC compared to reference quiet time have been observed. Such perturbation levels during geomagnetic storms can cause interference in communication and navigation systems.

5.5 Correlation between geomagnetic field variations and VTEC

5.5.1 Quiet time Sq(H) and VTEC correlation at Addis Ababa

Simultaneous $VTEC$ and $Sq(H)$ variations on the quiet days from each month at Addis Ababa are shown in Figures 5.19, 5.20, 5.21, 5.22, 5.23 and 5.24 for the years 2009, 2010, 2011, 2012, 2013 and 2014 respectively.. The mean values of VTEC ($\langle VTEC\rangle$) and mean values of $Sq(H)$ ($\langle Sq(H)\rangle$) are also shown in each graph. The black horizontal lines indicate the zero level of $Sq(H)$ at Addis Ababa.

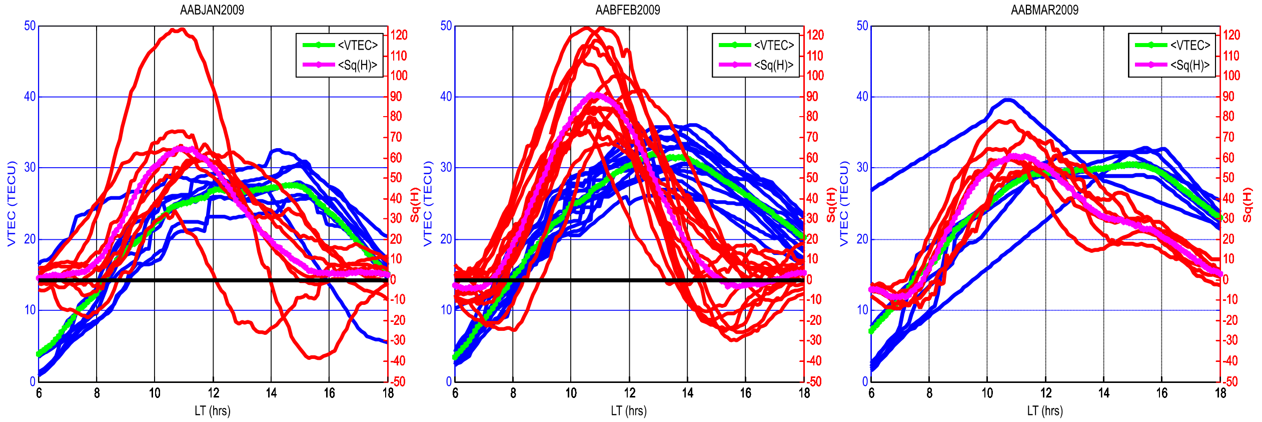

Figure 5.19: Simultaneous daytime variation of VTEC and Sq(H) at Addis Ababa in 2009.

Sq(H) attains its peaks earlier than VTEC confirming that $\boldsymbol{Sq(H)}$ influences VTEC. $\boldsymbol{Sq(H)}$ is driven by the eastward electric field. Once the electric field maximizes more plasma is uplifted to higher altitudes and it takes time for the plasma to be deposited for VTEC to maximize.

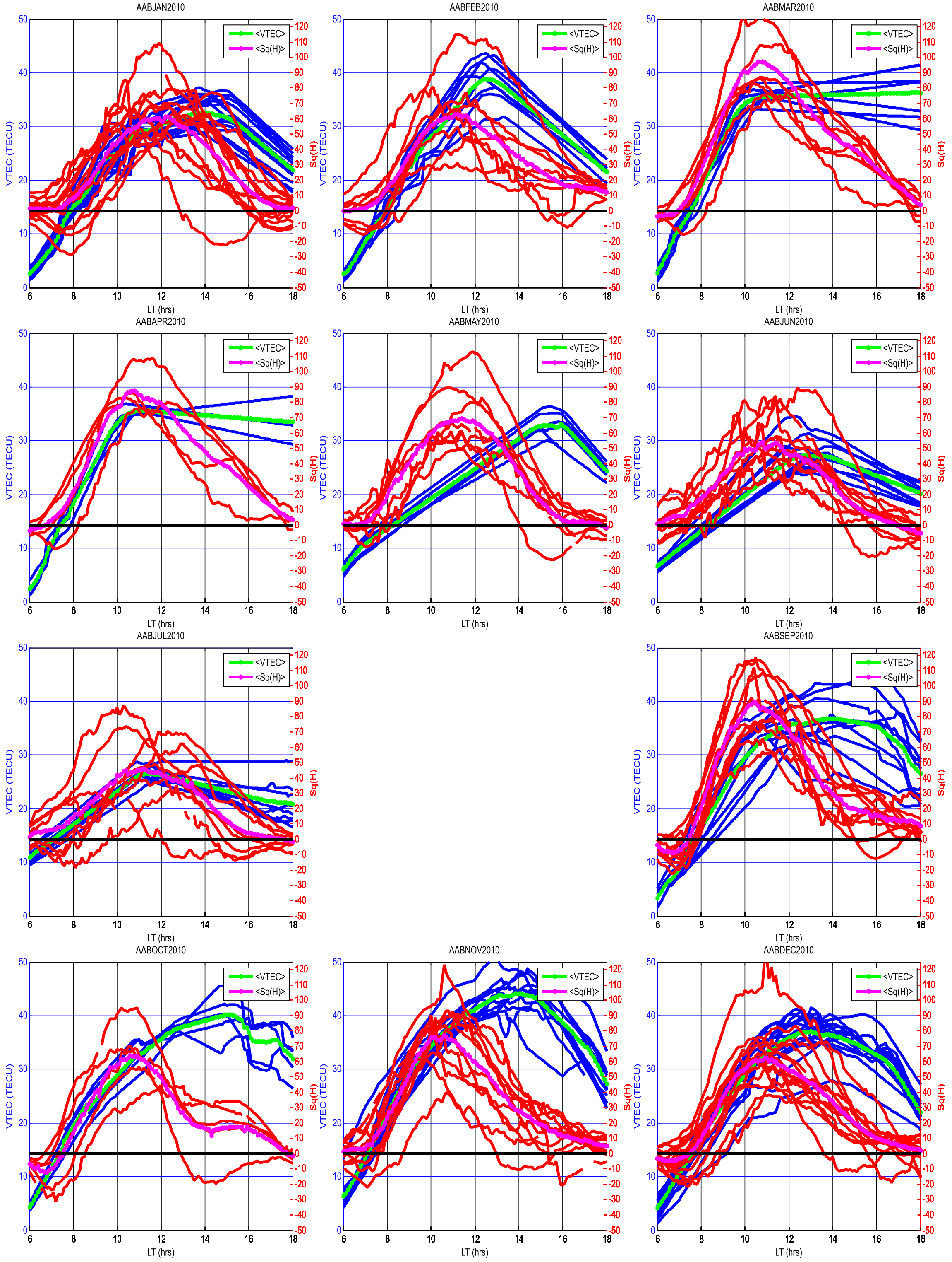

Figure 5.20: Simultaneous daytime variation of VTEC and Sq(H) at Addis Ababa in 2010.

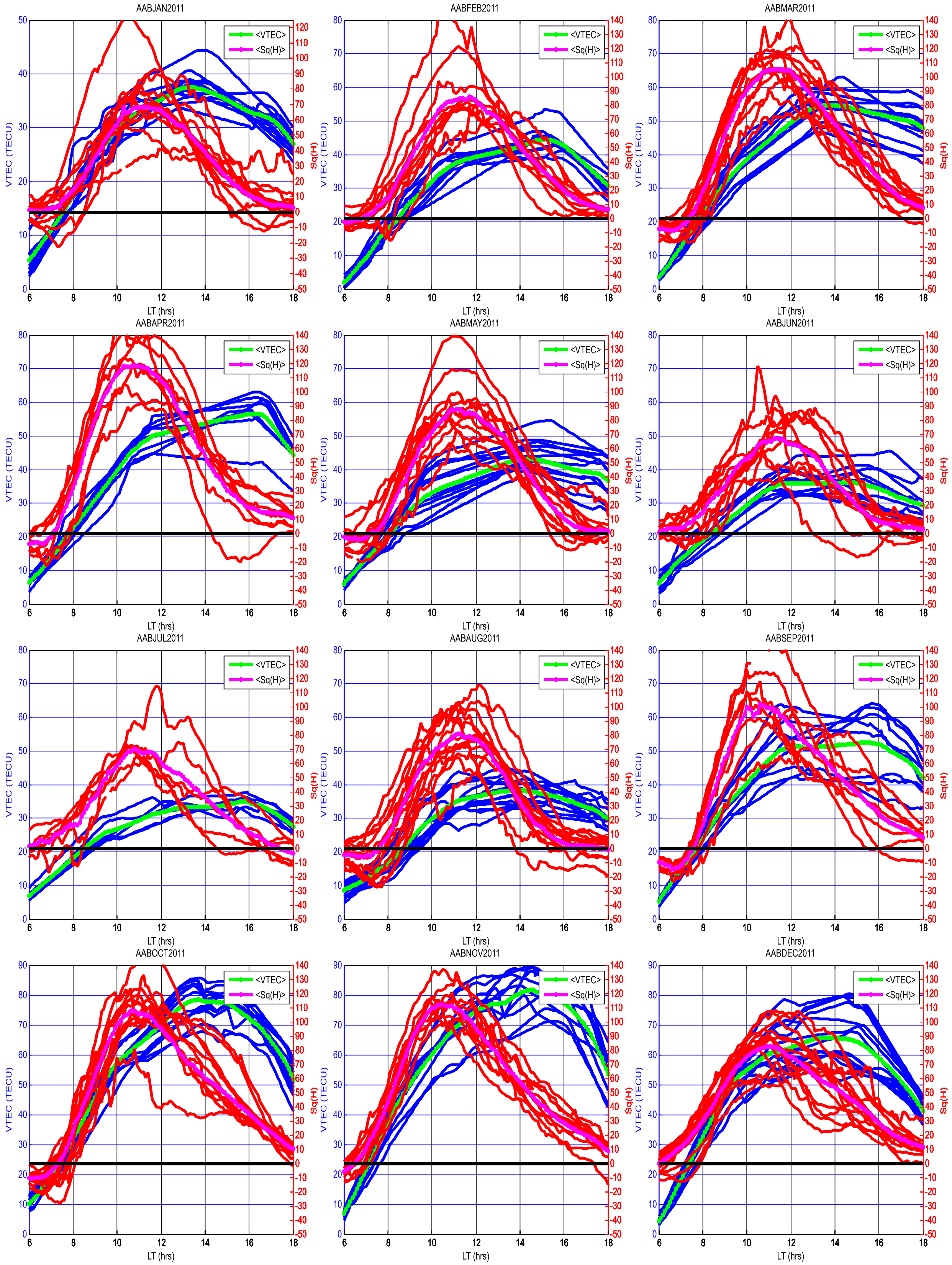

Figure 5.21: Simultaneous daytime variation of VTEC and Sq(H) at Addis Ababa in 2011.

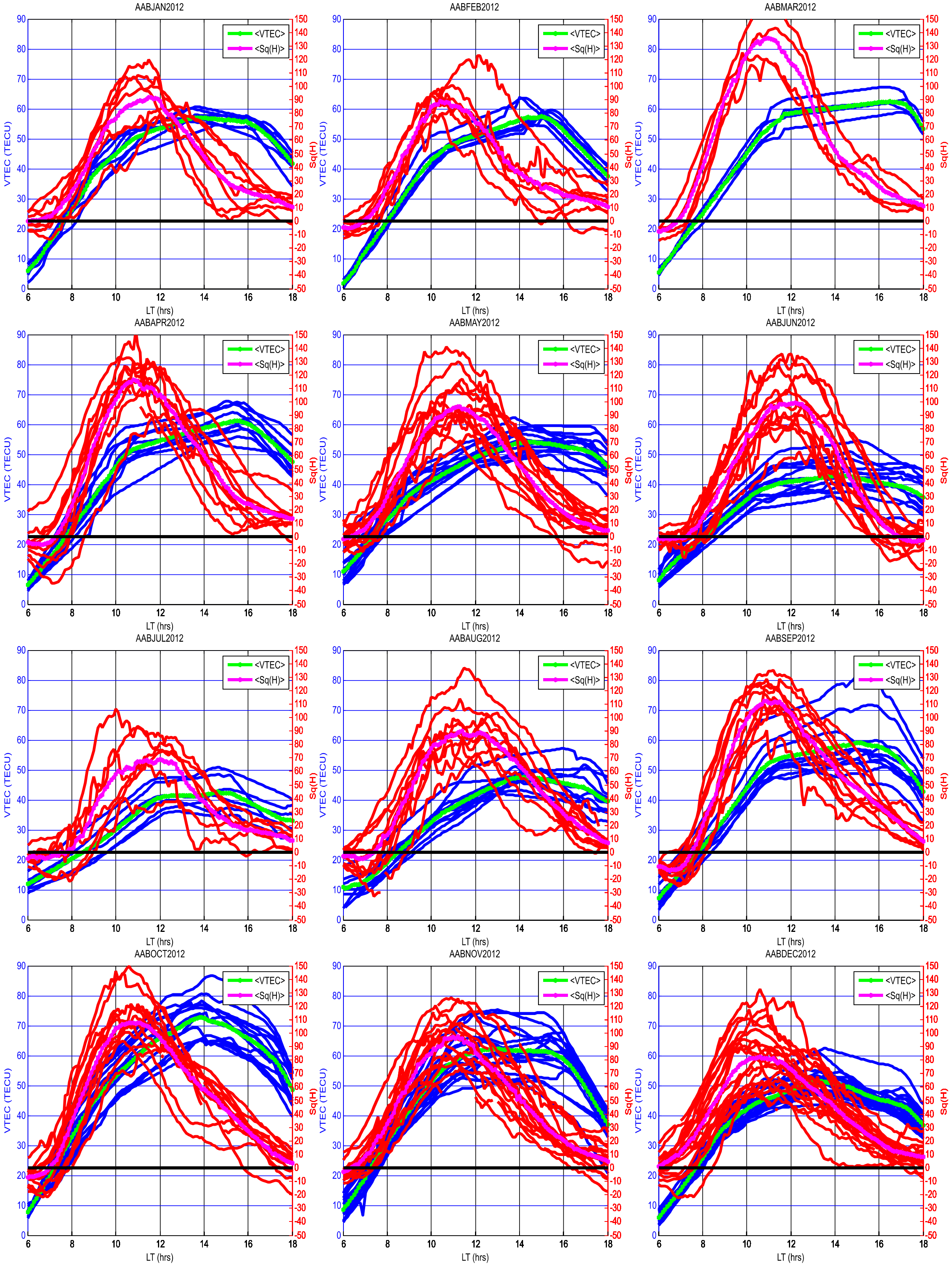

Figure 5.22: Simultaneous daytime variation of VTEC and Sq(H) at Addis Ababa in 2012.

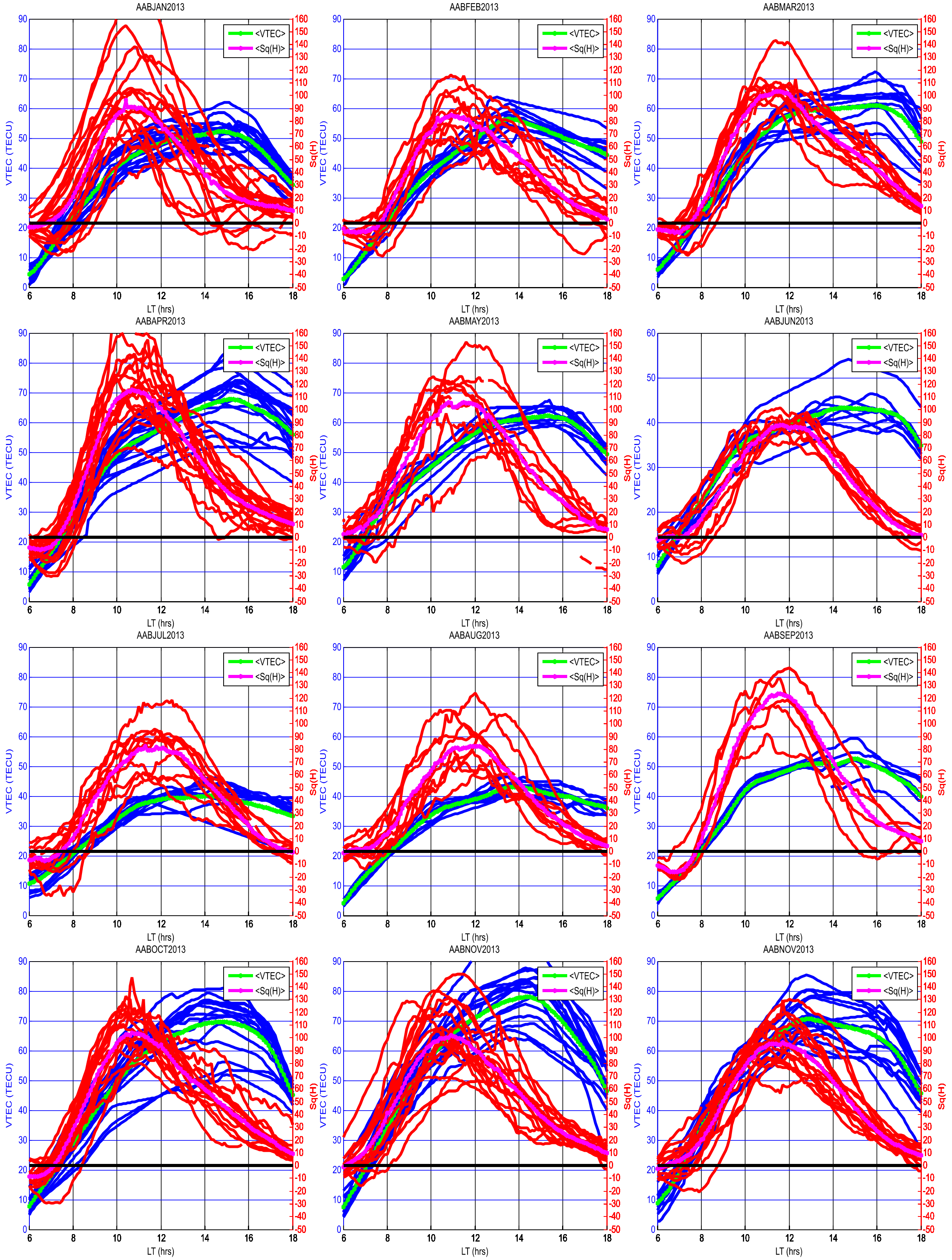

Figure 5.23: Simultaneous daytime variation of VTEC and Sq(H) at Addis Ababa in 2013.

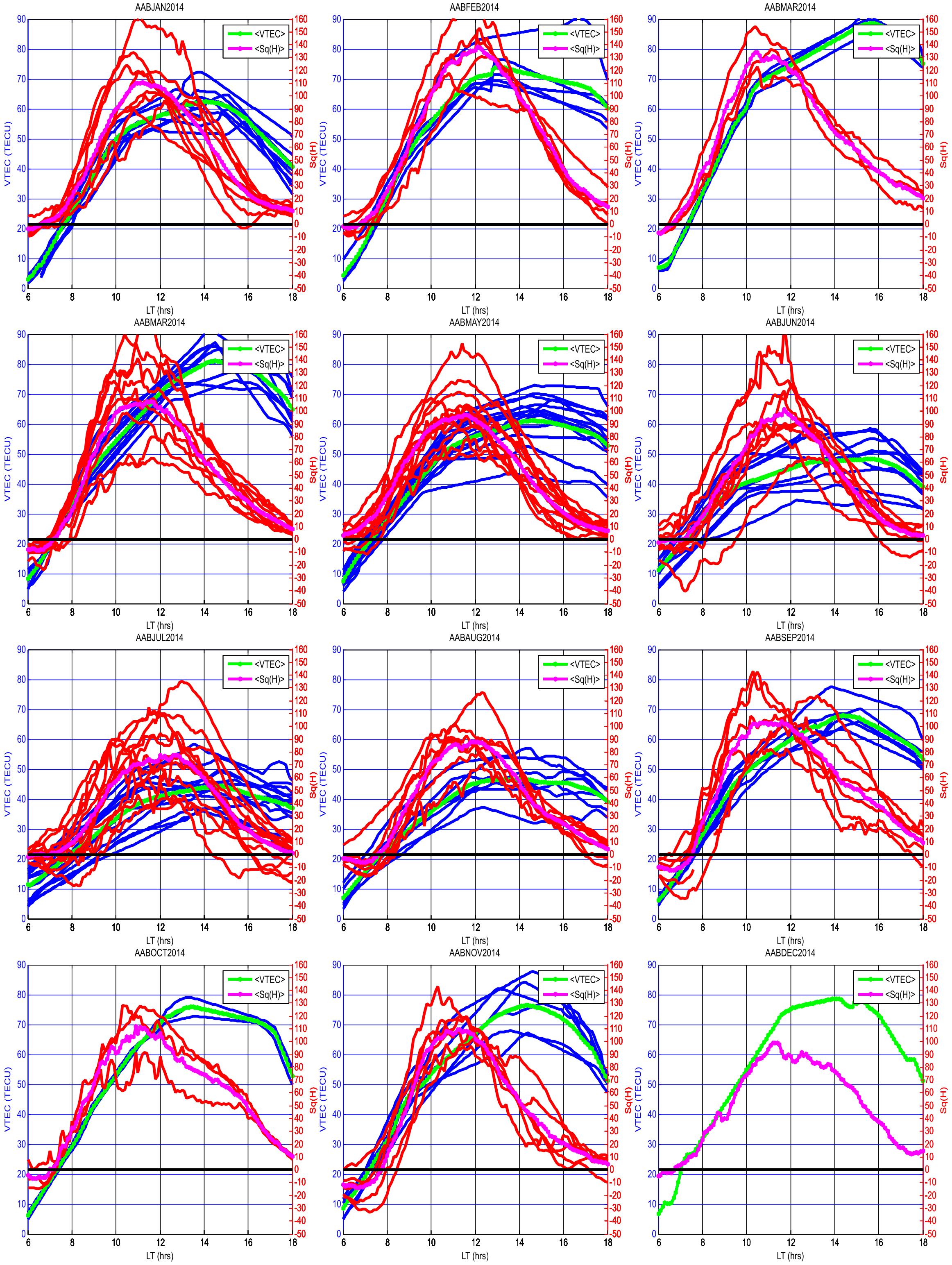

Figure 5.24: Simultaneous daytime variation of VTEC and Sq(H) at Addis Ababa in 2014.

5.5.1.1 Prenoon phase of daytime (0600-1200 LT) at Addis Ababa

The magnitudes of $VTEC$ have been found to increase steeply from 0600 LT to around 0900 LT during the entire period of study, consistent with the results of **Chakraborty and Hajra (2008)** as well as **Bolaji *et al.* (2013)**. **Chakraborty and Hajra (2008)** suggested that the contribution of solar flux to TEC maximizes around 0800-0900 LT after which the rate remains approximately constant. During the assumed constant period of rate of production, EIA can continue to dominate due to strong reversal of westward nighttime to the eastward daytime electric field around 0700 LT. This can affect the steep increase on $VTEC$ around 1000 LT resulting in its gradual increase and pre-noon peaks. The $Sq(H)$ averagely maximizes around1100LT-1200 LT. Maximized $Sq(H)$ implies full development of EIA caused by strongest vertical $\vec{E} \times \vec{B}$ drifts due to EEJ.

The daytime hours (0600–1800 LT) were categorized into two phases, namely the prenoon (0600-1200 LT) and afternoon (1300-1800 LT) phases. Also, the correlation coefficients between $VTEC$ and $Sq(H)$ values were computed on all the quiet days from each month based on the prenoon and afternoon phases throughout the period of study. These correlation coefficients have been plotted in Figure 5.25.

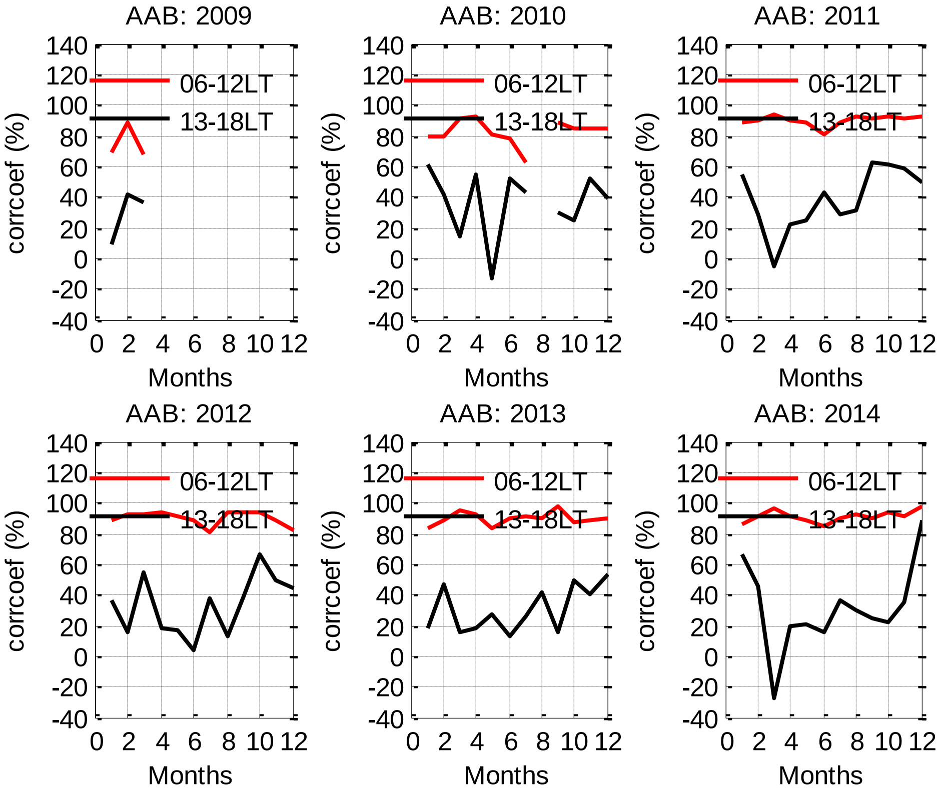

Figure 5.25: Correlation coefficient values between VTEC and $Sq(H)$ variations at Addis Ababa

Figure 5.25 shows that the correlation coefficients between $VTEC$ and $Sq(H)$ during the prenoon phase (0600–1200 LT) were strongest and ranged from 0.69 in January, 2009 to 0.98 in December, 2014. This strongest relationship was caused by the continuous independent increase of the magnitudes of VTEC due to photo-ionization and $Sq(H)$ magnitudes due to the eastward electric field. This implies that photo-ionization on VTEC variation increases linearly with the increase in $Sq(H)$. The correlations are weakest during the period 1300-1800 LT mainly due to the discrepancy in the time instants of occurrence of peaks in $Sq(H)$ and VTEC. The $Sq(H)$ values attained their maxima earlier around 1100 LT and 1200 LT compared to that of VTEC which were seen around 1300 LT and 1500 LT, except for some pre-noon peaks during the prenoon phases. The pre-noon peaks are attributed to the absence of counter electrojet during sunrise hours, thereby creating great plasma intensity on VTEC before and during noon. On the other hand, the absence of pre-noon and noon peaks result from the increase in the intensity of solar radiation which is inversely proportional to the solar zenith angle, making photo-ionization dominant over EIA forming mechanisms. The $Sq(H)$ at AAB generally attains its peak around 1100 LT during low solar activity years 2009 and 2010 and near noon during high solar activity years 2013 and 2014 consistent with the results of **Rastogi and Iyer (1976)**.

The annual correlation coefficients between VTEC and $Sq(H)$ were computed for the ascending phase of the daytime variation. The results are shown in Figure 5.26.

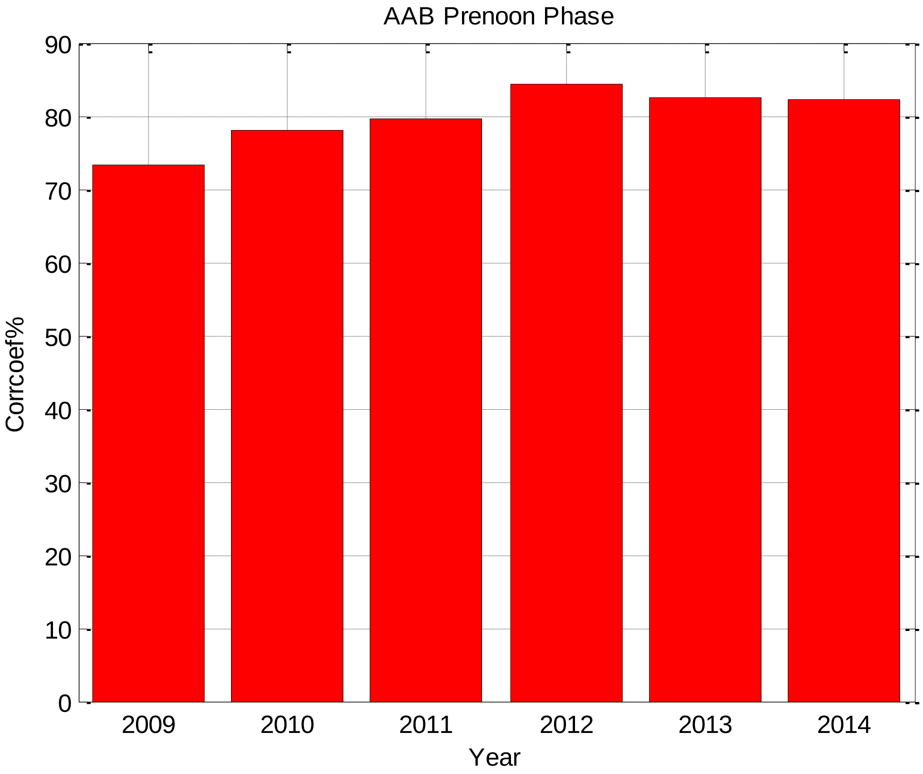

Figure 5.26: Annual prenoon phase correlation between VTEC and $Sq(H)$ at Addis Ababa from 2009 to 2014

Figure 5.26 shows strong positive linear relationship between VTEC and $Sq(H)$. The correlation coefficient during high solar activity year (2014) is greater than the corresponding correlation coefficient in the low solar activity year (2009). The motivation for converting the correlation coefficients into percentages was the need for easy legibility of the graph without losing meaning of the magnitude of the correlation. This was advised by a reviewer of one of my publications through a private communication.

5.5.1.2 Afternoon phase of daytime (1300-1800 LT) at Addis Ababa

Figure 5.27 shows the annual correlation coefficients between VTEC and $Sq(H)$ at AAB during the afternoon phase of the daytime (1300-1800 LT). The correlation is, generally, weak and attained the highest value of 0.38 in the year 2011. During the descending phase of the daytime, correlation coefficients computed range from -0.28 in March, 2014 to 0.89 in December, 2014. The weak correlation is attributed to the discrepancy in the instants of turning points of VTEC and $Sq(H)$ graphs. For example, after $Sq(H)$ has reached its peak and begun to descend, VTEC is observed aiming to attain its peak resulting in phase shifts. The discrepancy in the instants of peak VTEC and $Sq(H)$ is caused by two coupled physical processes, namely $\vec{E} \times \vec{B}$ drifts and photo-ionization. The near zero degrees solar zenith angle maintains photo-ionization, hence sustaining the increase in VTEC. However, $Sq(H)$ changes direction westward after reaching its peak and gets to the zero level and beyond due to the change in direction of $\vec{E} \times \vec{B}$ from upward to downward trend.

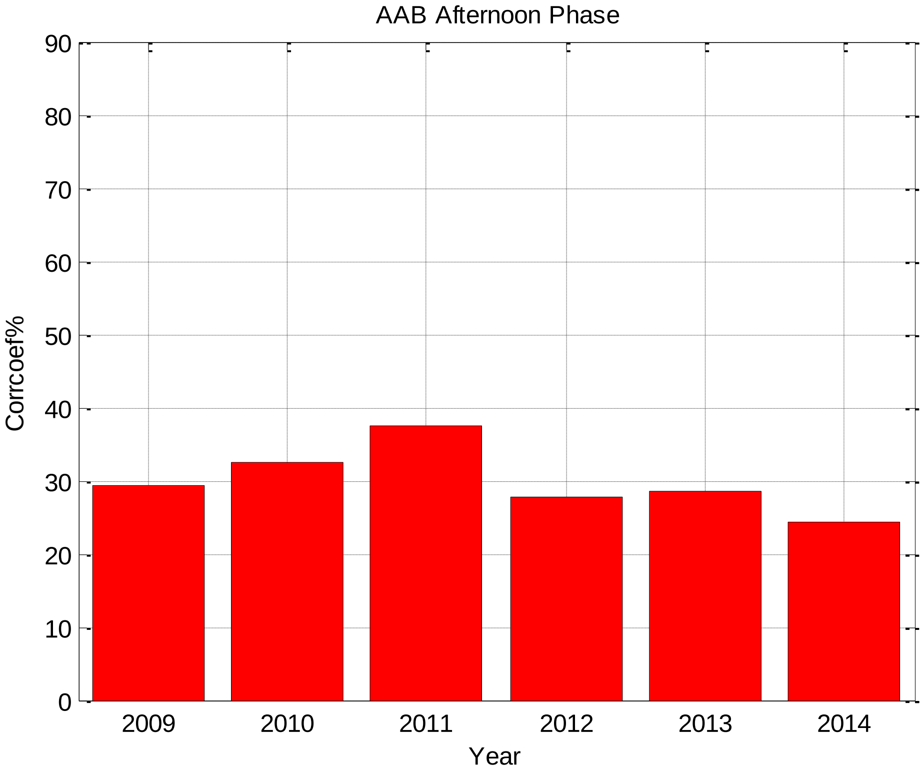

Figure 5.27: Annual afternoon phase correlation between VTEC and $Sq(H)$ at Addis Ababa from 2009 to 2014

5.5.2 Day time variations of VTEC and $Sq(H)$ at Nairobi

Simultaneous VTEC and $Sq(H)$ variations on the quiet days from each month at Nairobi have been displayed in Figures 5.28, 5.29, 5.30, 5.31, 5.32 and 5.33 corresponding to the years 2009, 2010, 2011, 2012, 2013 and 2014 respectively. The mean values of VTEC and mean values of $Sq(H)$ are also shown in each graph. The black horizontal cyan lines mark the zero level of $Sq(H)$ at Nairobi.

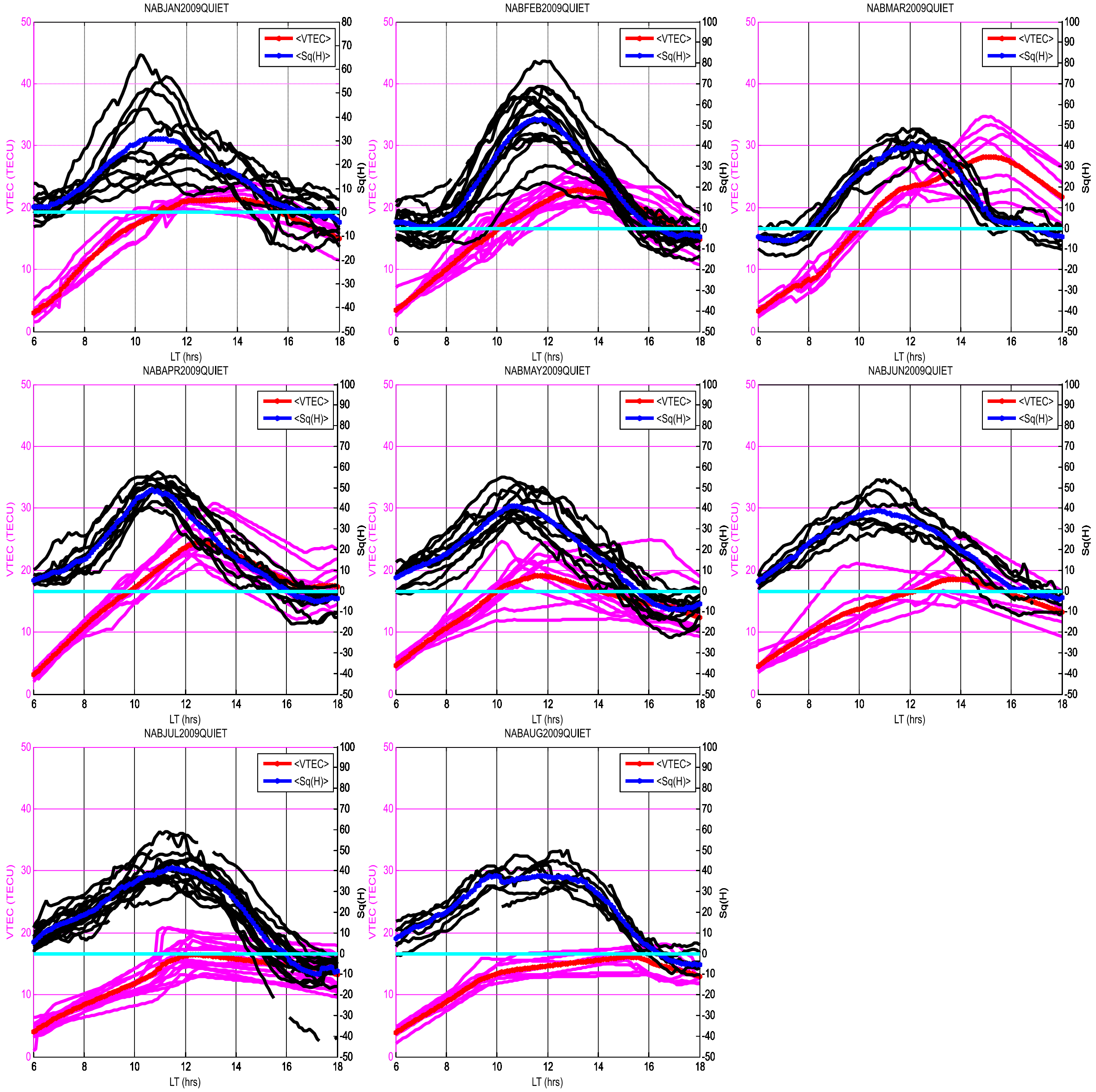

Figure 5.28: Simultaneous daytime variation of VTEC and Sq(H) at Nairobi in 2009.

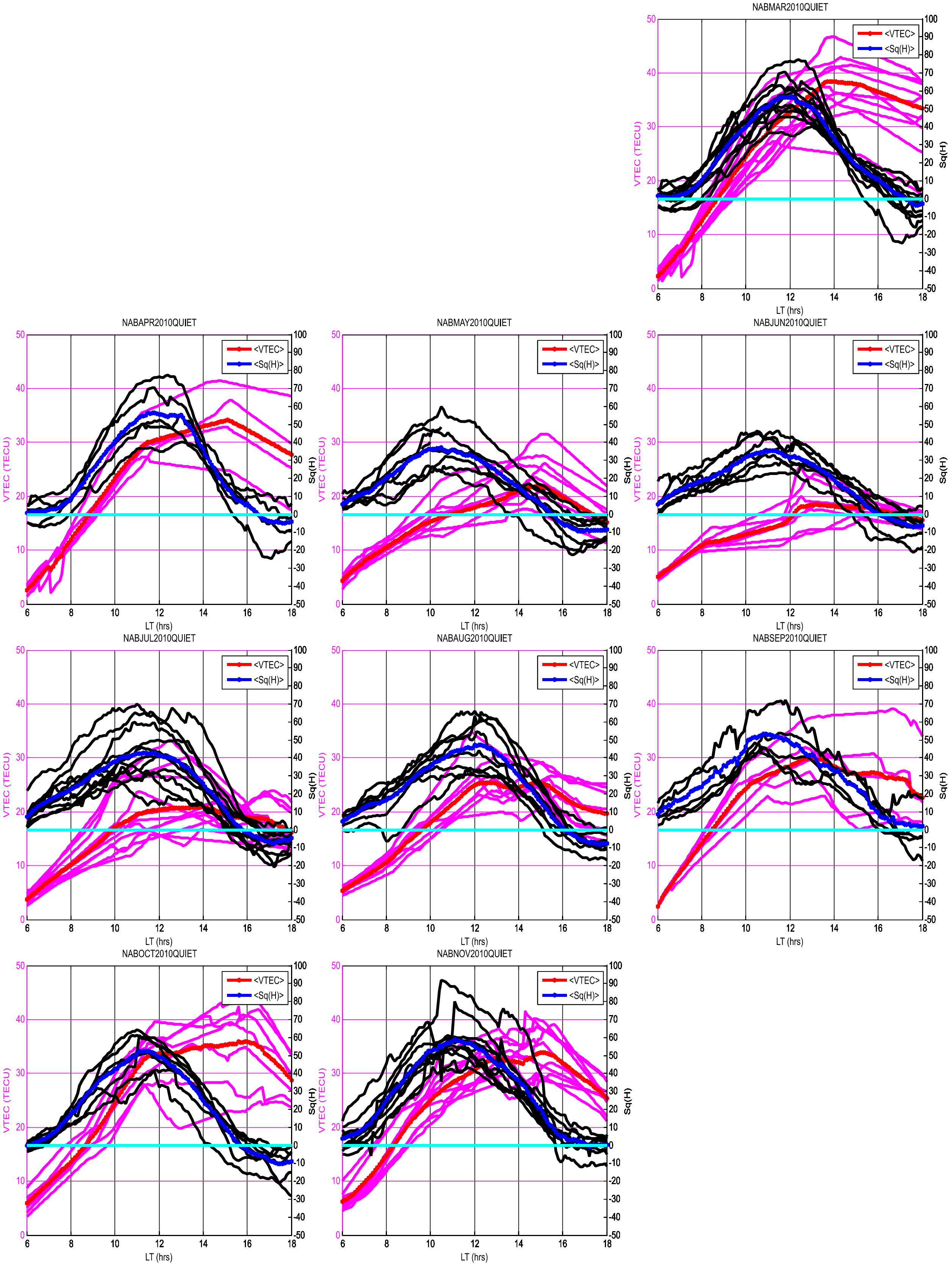

Figure 5.29: Simultaneous daytime variation of VTEC and Sq(H) at Nairobi in 2010.

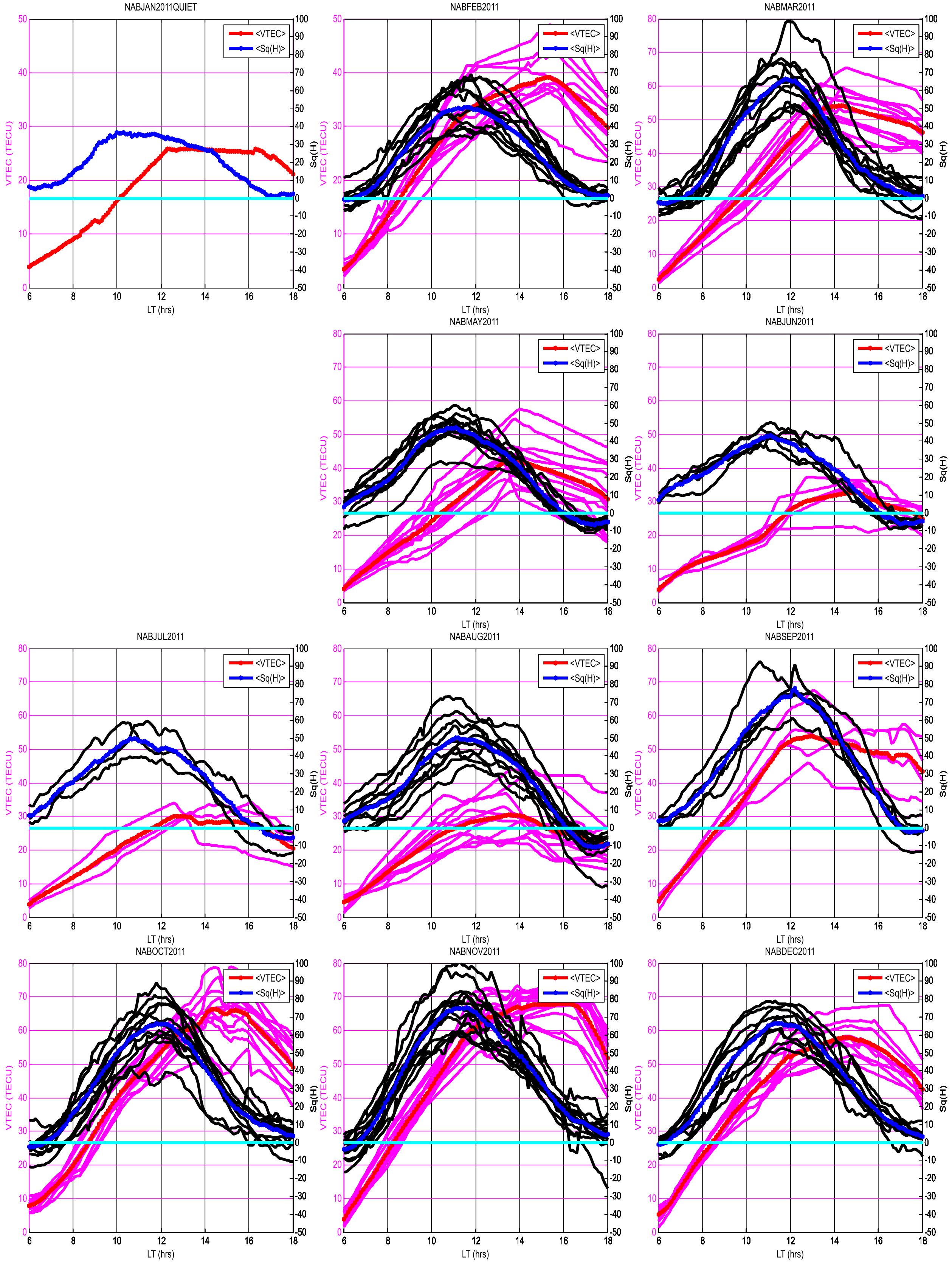

Figure 5.30: Simultaneous daytime variation of VTEC and Sq(H) at Nairobi in 2011.

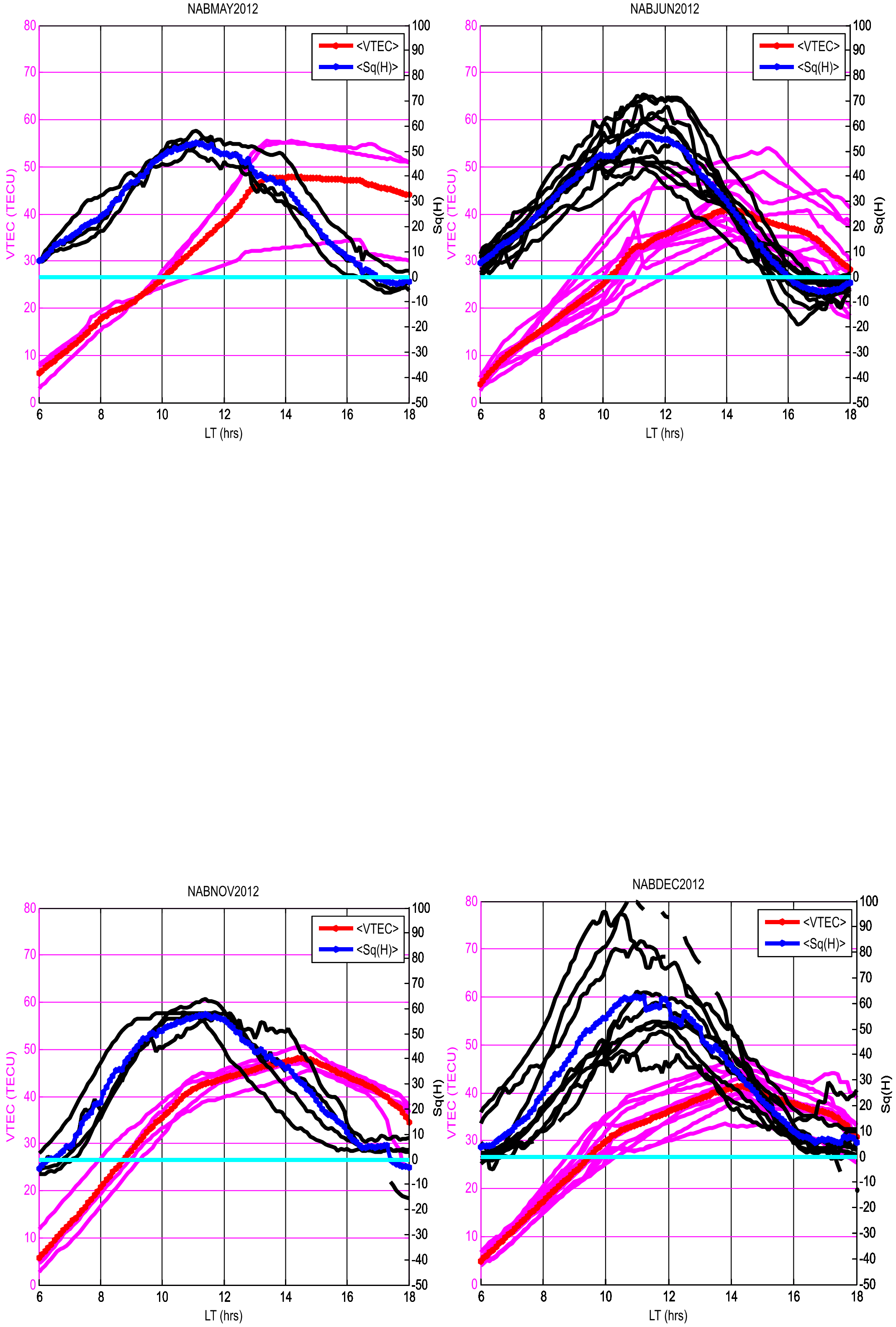

Figure 5.31: Simultaneous daytime variation of VTEC and Sq(H) at Nairobi in 2012.

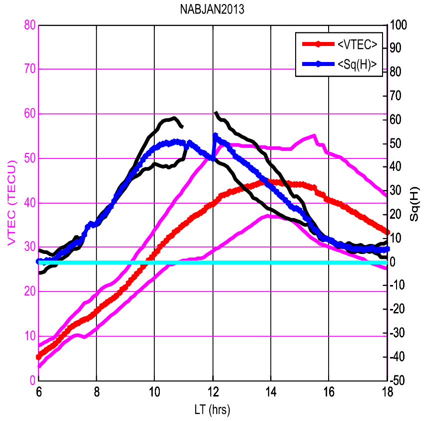

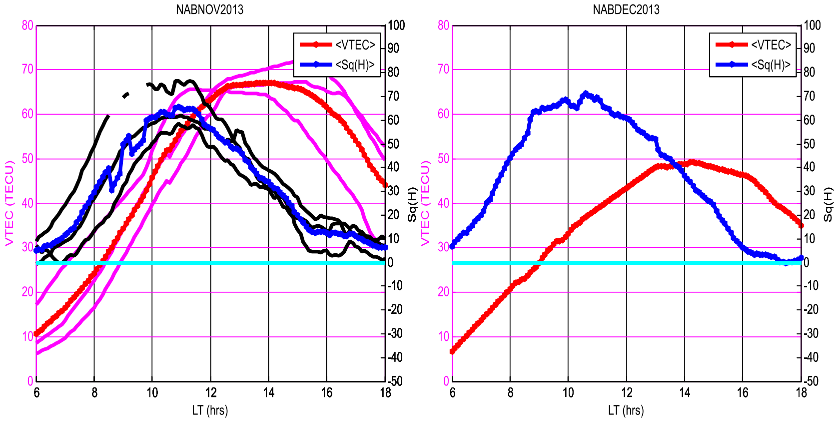

Figure 5.32: Simultaneous daytime variation of VTEC and Sq(H) at Nairobi in 2013.

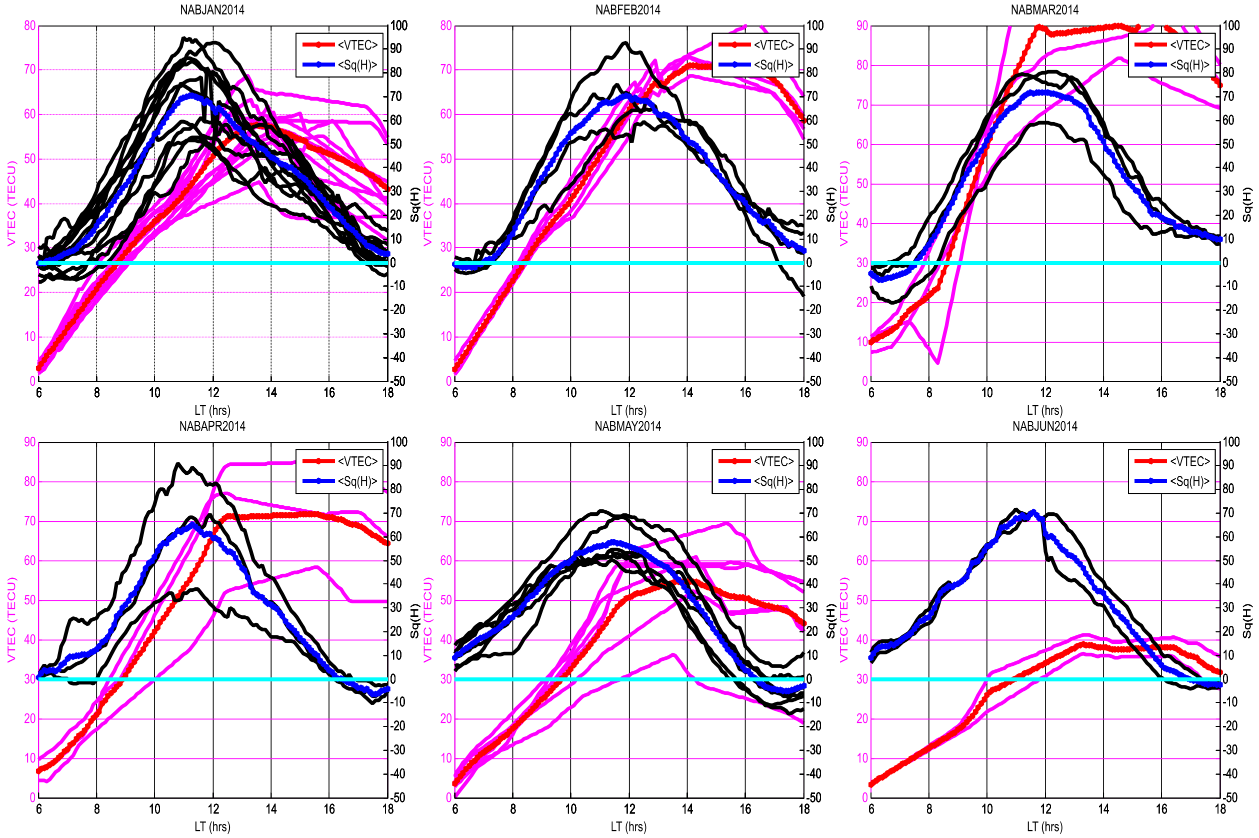
NABJAN2014 NABFEB2014 NABMAR2014

NABAPR2014 NABMAY2014 NABJUN2014

Figure 5.33: Simultaneous daytime variation of VTEC and Sq(H) at Nairobi in 2014.

5.5.2.1 Prenoon phase of daytime (0600-1200 LT) at Nairobi.

We note that NAB station suffered geomagnetic field and GPS data gaps in some months. These months, are therefore, not shown in the plots. The values of $VTEC$ increase steadily, from 0600 LT to around 0900 LT during the entire period of study, similar to earlier observations at AAB. The increase then becomes gradual resulting in peak values in the range from 1300 LT to 1500 LT. The peak values of $VTEC$ at Nairobi are smaller than those at Addis Ababa. These features are attributed to the presence of EEJ at Addis Ababa which acts to deposit plasma on $VTEC$. $Sq(H)$ values increase from 0800 LT to around 1100-1200LT when they attain their peaks. Nevertheless, the magnitudes of $Sq(H)$ peaks are smaller at Nairobi than at Addis Ababa mainly due to the EEJ that is imposed onto the normal Sq current system at Addis Ababa. The magnitudes of $VTEC$ and $Sq(H)$ at both stations are higher during high solar activity year (2014) than during low solar activity year (2009).

The correlation coefficients between $VTEC$ and $Sq(H)$ were calculated for each month based on prenoon (0600-1200 LT) and afternoon (1300-1800 LT) phases in the entire period of study. The results shown in Figure 5.34 indicate that during the prenoon phase (0600-1200 LT), correlation coefficients were strong, ranging from 0.61 in June, 2010 to 0.97 in December, 2013. These observations of strong linear relationship between $VTEC$ and $Sq(H)$ are similar to those obtained at AAB.

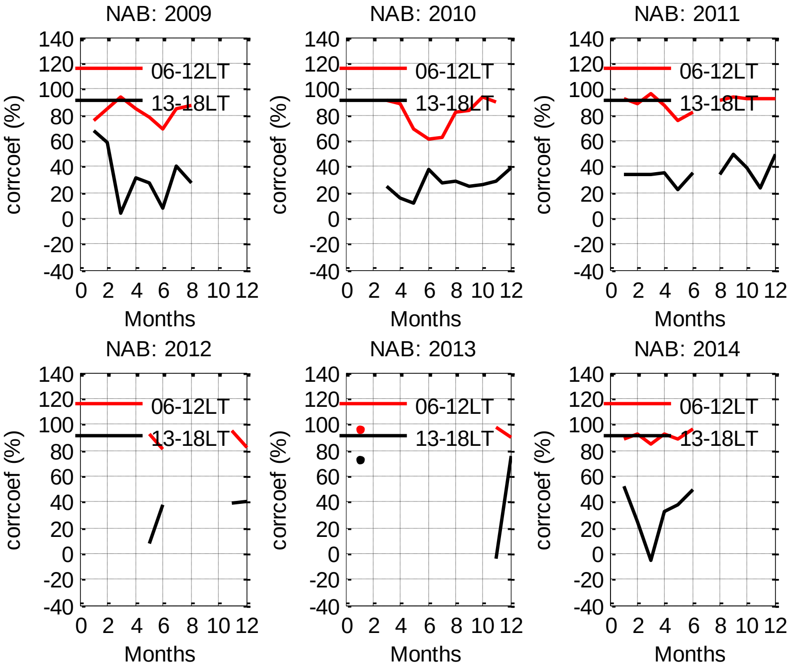

Figure 5.34: Correlation coefficient values between VTEC and Sq(H) variations at Nairobi

The annual correlation coefficients between $VTEC$ and $Sq(H)$ were also determined for the prenoon phase of the daytime variation. The results are displayed in Figure 5.35.

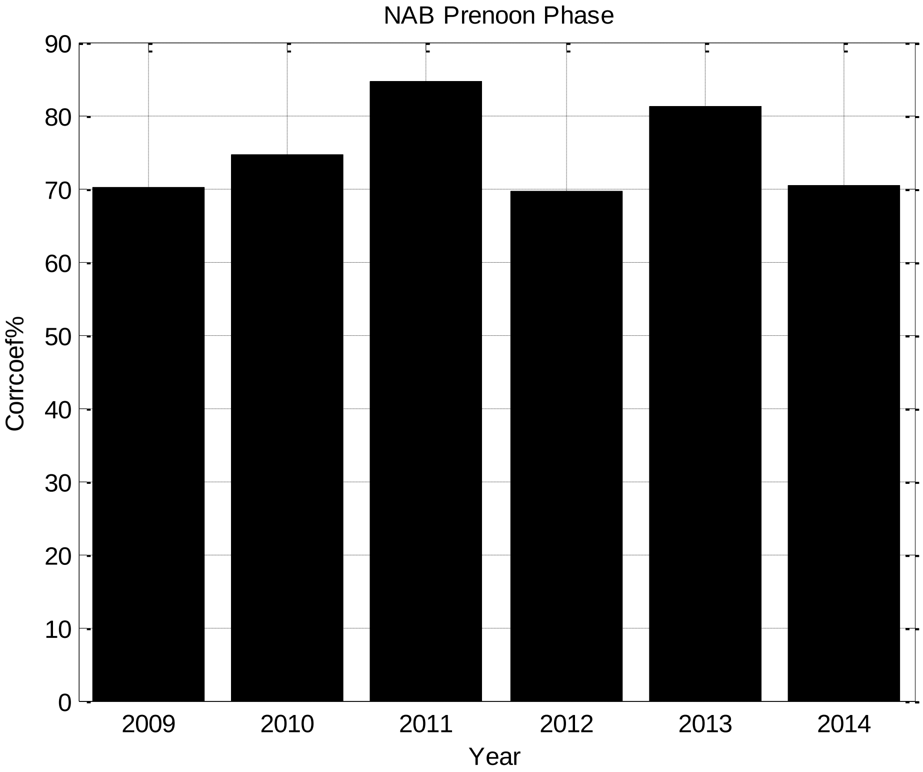

Figure 5.35: Annual prenoon phase correlation between $VTEC$ and $Sq(H)$ at Nairobi from 2009 to 2014.

Figure 5.35 confirms the existence of strong positive correlation between VTEC and $Sq(H)$ annually at Nairobi during the prenoon phase (0600-1200 LT). This suggests that the variation of $Sq(H)$ may be inferred from the variation of VTEC during this period.

5.5.2.2 Afternoon phase of daytime (1300-1800 LT) at Nairobi

During the afternoon phase of the daytime, correlation coefficients range from -0.06 in March, 2014 to 0.76 in December, 2013. Incidentally, considering the annual correlation coefficients during the descending phase, the strongest positive correlation was observed in the year 2011, moderate solar activity year, just like at AAB.

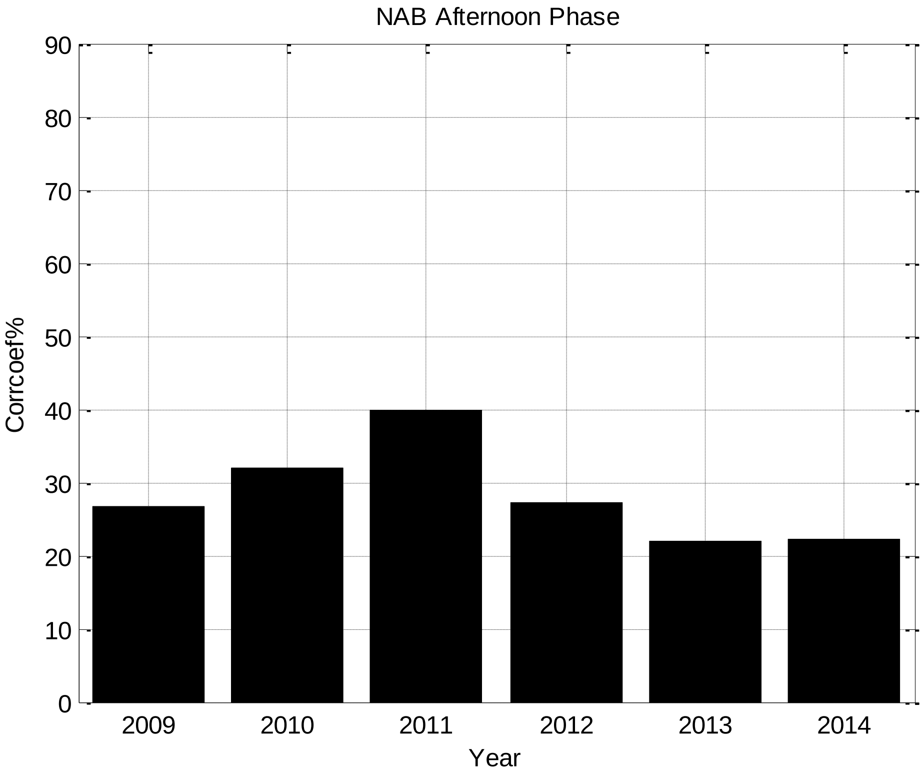

Figure 5.36: Annual afternoon phase correlation between VTEC and $Sq(H)$ at Nairobi, from 2009 to 2014

5.5.3 Inferring VTEC from the $Sq(H)$ values

Figure 5.37 shows the relationship between VTEC and $Sq(H)$ during the prenoon phase of the daytime (0600 LT-1200 LT), obtained through the process of polynomial regression. The resulting quadratic equations are shown within the graphs.

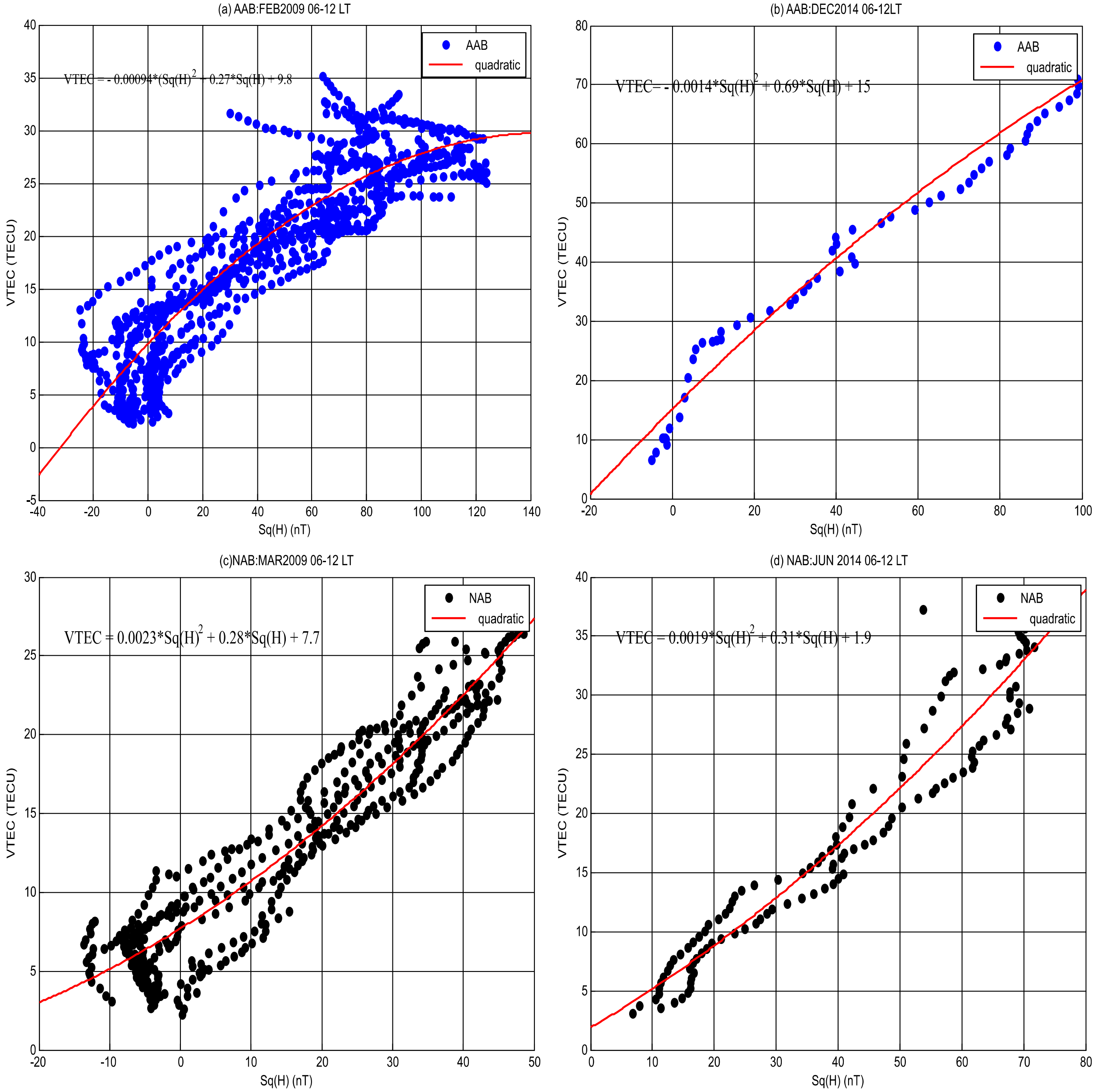

Figure 5.37: The relationship between VTEC and Sq(H) during arbitrarily selected months in 2009 and 2014.Part (a) shows the relationship at Addis Ababa in February, 2009, (b) indicates the relationship at Addis Ababa in December, 2014. In (c), the relationship is shown for Nairobi in March, 2009 and (d) illustrates the relationship at Nairobi in June, 2014.

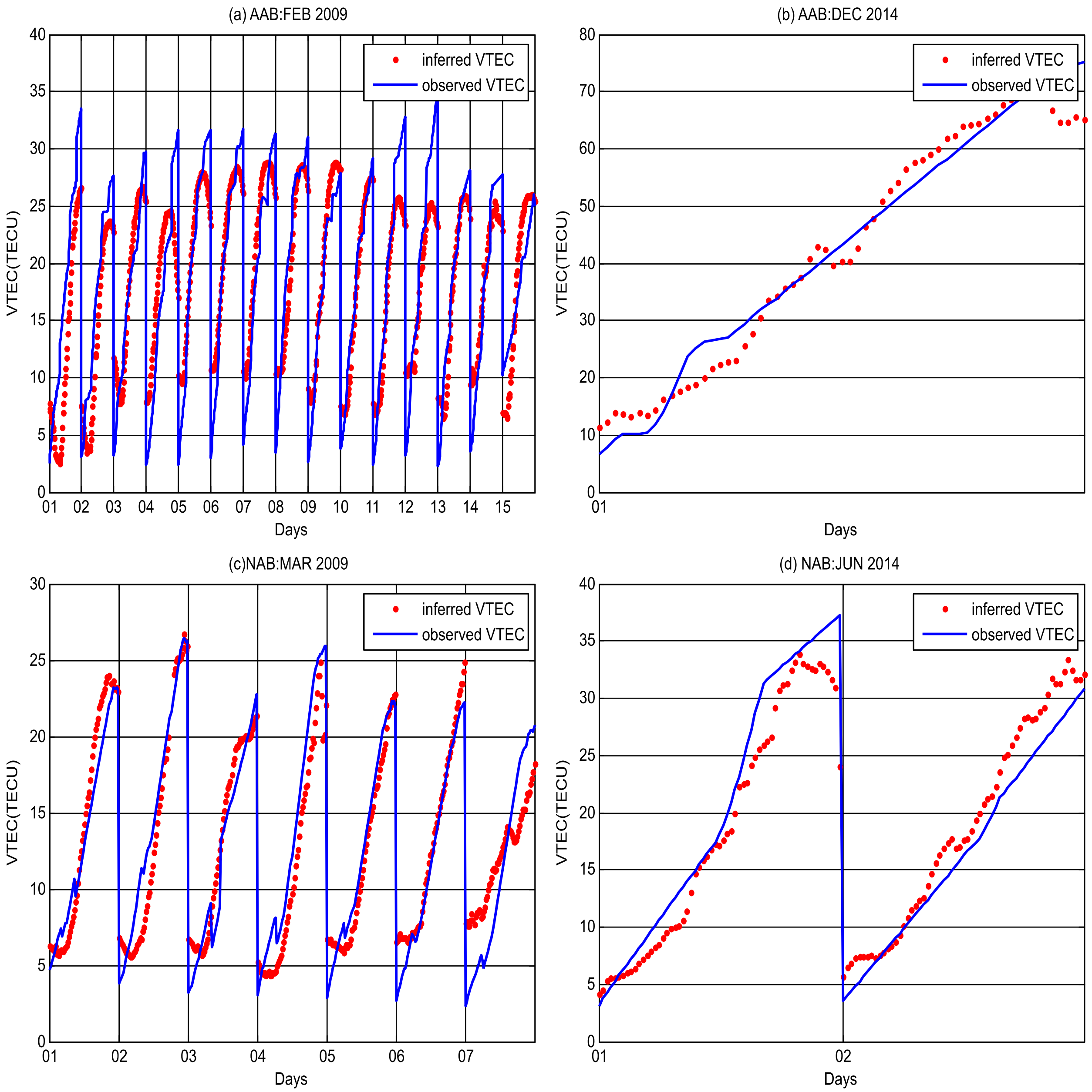

Figure 5.38: Comparison of the inferred VTEC with the GPS measured VTEC during the period 0600 -1200 LT. The horizontal axis in each graph represents the number of geomagnetic quiet days.

Figure 5.38 confirms that there exist quantitative relationships between $Sq(H)$ and VTEC during the ascending phase of the daytime validated by the good comparison between $Sq(H)$ inferred VTEC with the actual GPS measured VTEC.

CHAPTER SIX: SUMMARY, CONCLUSIONS AND RECOMMENDATIONS

The current chapter summarizes the major findings, discusses the practical application and implications of the findings in the real world and makes recommendations for present and further research.

6.1 Summary

The present study had set out to: determine the mean annual variation of the geomagnetic field from the low solar activity year (2009) to the high solar activity year (2014) within East Africa; investigate the annual morphology of TEC within East Africa; investigate the correlation between geomagnetic field variations and TEC during the ascending phase of solar cycle 24 in East Africa and investigate the possibility of inferring $VTEC$ from $Sq(H)$.

In summary, the present study has provided the following contributions to knowledge.

1) Global effects due to equatorial ring currents and storm time thermospheric winds cancel local effects, such as effects of neutral winds, during the main phase of the storm.
2) The Equatorial Ionization Anomaly is pronounced during high solar activity due to the intensification of the zonal electric field.
3) The correlation between $VTEC$ and $Sq(H)$ over the East African sector is strongest during (0600-1200 LT) and increases with increase in solar activity. It is suggested that the $VTEC$ measured at this time may be used as an input in modeling $VTEC$ over this sector in the local morning hours.
4) Geomagnetic quiet time TEC variations during the prenoon phase of the daytime (0600-1200 LT) may be inferred from the quiet time geomagnetic field data.

6.2 Conclusions

The amplitude of mean $Sq(H)$ has shown dependence on local time of the day and solar activity at Addis Ababa and Nairobi stations. The mean $Sq(H)$ increases steadily from morning hours attaining peak values around 1100 LT at Addis Ababa during low solar activity years (2009, 2010, 2011) and 1200 LT during high solar activity years (2012, 2013 and 2014), then decreases gradually attaining minimum values ,around $0\ nT$, in the evening hours around 1700 LT. In Nairobi, the peak in mean $Sq(H)$ is achieved around 1130 LT. This local time dependence is attributed to the variation in solar heating and ionization rates. Peak values of the mean $Sq(H)$ are highest in solar maximum years. In addition, the mean $Sq(H)$ at Nairobi is consistently higher than the corresponding values at Addis Ababa; attributed to the morning counter electrojet that acts to reverse the direction of the $Sq(H)$ current system closer to the geomagnetic equator.

The geomagnetic field variations during geomagnetic storms are characterized by irregular perturbations in the H-field. These irregularities are caused by the induced electric field from the solar wind constituents into the Earth's atmosphere. In general, the geomagnetic storms resulted in a depression of the geomagnetic field variation (reversal in the direction of the geomagnetic field variation from Eastward to westward) due to the imposition of the westward ring currents. The results demonstrate that moderate storms can have impacts of magnitudes comparable to the impacts of major storms on the geomagnetic field.

During geomagnetically quiet times, mean annual VTEC increases from morning hours (about 0700 LT); maximizing around 1300 LT; then decreases gradually towards sunset (1900 LT). Such local time dependence of the morphology of VTEC is mainly caused by the variation in the intensity of the main source of ionization, Extreme Ultraviolet radiation, with local time of the day, which defines the solar zenith angle. The peak quiet time mean VTEC is less than the corresponding peak at Addis Ababa during low solar activity year (2009); but this difference decreases with increase in solar activity, until at the high solar activity year (2014) when peak value at Nairobi overtakes the peak value at Addis Ababa. This phenomenon is attributed to the intensification of the eastward electric field, which is responsible for uplifting of ionospheric plasma to higher altitudes during daylight hours, and then the plasma diffuses through gravity and pressure gradients to higher latitudes creating a trough of ionization close to the dip equator and crest of ionization at $\pm 15^0$ latitudes. Further, the peak values of mean VTEC were found to increase with increase in geomagnetic activity. Sufficient amplitude scintillation, $S_4 > 0.2$ well correlated with depletions in VTEC have been found in the local post sunset sector during the months of February, March, April, May, June, July, August, September and October and the greatest values occurred in March and April, 2014 over Maseno, Kenya. The correspondence of VTEC depletions with increase in S_4 index is in conformity with results from previous researchers **(Dashora and Pandey, 2005, Seemala and Valladares, 2011).** The depletions are attributed to density irregularities and are manifested in ionospheric scintillations.

The response of VTEC to geomagnetic storms exhibited an enhancement (maximum up to 160%) and depletion (maximum up to 80%) in VTEC, which can cause interference to communication systems, compared to the corresponding quiet time values. The perturbations in ***H***-field and VTEC are attributed to disturbance dynamo electric field and storm time thermospheric winds.

The present study has demonstrated that the instants of occurrence of peaks in $VTEC$ are controlled by processes of EIA formation and photo-ionization. The magnitudes of peaks of $VTEC$ obtained in this study are stronger than those obtained in West Africa by **Bolaji *et al.* (2013)** due to the stronger equatorial electrojet in East Africa. The correlation coefficients between $VTEC$ and $Sq(H)$ calculated throughout the entire period of study show that during the prenoon phase of the daytime (0600-1200 LT) the linear relationship is stronger than during the afternoon phase (1300-1800 LT). The observed strong relationship during ascending phase of the daytime is attributed to the independent increase of the eastward electric field on $Sq(H)$ and photo-ionization on$VTEC$. Weak relationship during the descending phase is mainly due to the domination of photo-ionization over EIA. Further, the magnitudes of peak $VTEC$ and $Sq(H)$ at Addis Ababa have been found to be greater than the corresponding peaks at Nairobi; mainly attributed to the strong EEJ at Addis Ababa. In addition, correlation coefficients at Addis Ababa are stronger than those at Nairobi.

The time instants of the impact of the storms on geomagnetic field and VTEC are correlated, showing that the global drivers of storms (equatorial ring currents and storm time thermospheric winds) overwrite the local factors determining the variation of the geomagnetic field and VTEC.

It is possible to infer quiet time VTEC variations from ***Sq (H)*,** during the period 0600-1200 LT.

6.3 Recommendations for future work

The present study acts as a starting point for future related studies. Examples of possible future studies related to the current work are stated below.

This work provides trends in VTEC and geomagnetic field variations over the equatorial East African sector during the ascending phase of the solar cycle 24 which can be used as a basis for developing a regional model for Sq current and VTEC prediction over this sector.

The present thesis has shown that the ionospheric E-region coupled interactive systems, namely, $Sq(H)$, EEJ and vertical $\vec{E} \times \vec{B}$ drifts, strongly influence TEC through EIA. A global model of the influence of these parameters on TEC is recommended. The results of such a study will provide information about the quantity of EEJ at the dip equator that determines the EIA that is developed and transported to the trough.

Further studies that are geared towards the estimation of TEC variations from the geomagnetic field variations during geomagnetic storms are necessary.

REFERENCES

Abbas, M. , Zaharadeen, Y.J., Joshua, B. & Mohammed, S. (2013). Geomagnetic Field Variations at Low Latitudes along 96 degrees Magnetic Meridian. *International Journal of Marine, Atmospheric & Earth Sciences* , 1(2), 96-109.

Abdu, M. A. (2005). Equatorial Ionosphere-Thermosphere System: Electrodynamics and Irregularities. *Advances in Space Research*, 35, 771-787

Adeniyi, J. O., Doherty, P. H., Oladipo, O. A. & Bolaji, O. (2014). Magnetic storm effects on the variation of TEC over Ilorin an equatorial station. *Radio Science*, 49, 1245-1253, doi: 10.1002/2014RS005404.

Afraimovich ,E. L., Astafieva , E. I., Voeykov , S. V., Tsegmed, B., Potekhin, A.P.& Rasson, J. L. (2006). An investigation of the correlation between ionospheric and geomagnetic variations using data from the GPS and INTERMAGNET networks. *Advances in Space Research , 38*, 2332-2336.

Afraimovich, E. L., Kosogorov, E. A., Lesyuta, O. S., Ushakov, I. I. & Yakovets, A. F. (2001). Geomagnetic control of the spectrum of traveling ionospheric disturbances based on data from a global GPS network. *Annales Geophysicae , 19*, 723–731.

Akala, A. O.,Somoye, E. O., Adeloye, A. B. & Rabiu, A. B. (2011). Ionospheric f0F2 variability at equatorial and low latitudes during high, moderate and low solar activity. *Indian Journal Of Radio & Space Physics* , 40,124-129.

Al'Perovich, L. S., Fedorov E. N.,Volgin, A. V., Pilipenko,V. A. & Pokhil'ko, S. N. (1991). Doppler sounding as a tool for the study of the MHD wave structure of the magnetosphere. *Journal of Atmospheric and Terrestrial Physics* , 55(67),581-586.

Anderson, A., Anghel, A., Yumoto, K., Ishitsuka, M. & Kudeki, E. (2002). Estimating daytime vertical drift velocities in the equatorial F-region using ground-based magnetometer observations. *Geophysical Research Letters , 29* (12), 1596.

Anderson, A., Anghel, A., Chau, J., Yumoto, K., Battacharyya, A.& Alex,S. (2006). Daytime, low latitude, vertical ExB drift velocities, inferred from ground-based magnetometer observations in the Peruvian, Philippine and Indian longitude sectors under quiet and disturbed conditions. *ILWS Workshop, GOA.*

Basu, S. & Gupta, A. D. (1967). Latitude Variation of Total Electron Content in the Equatorial Region. *Journal of Geophysical Research , 72* (21), 5555-5558.

Baumjohann, W. & Treumann, R. A. (1996). *Basic Space Plasma Physics.* London: Imperial College Press.

Bhattacharya, S., Purohit, P.K. & Gwal, A.K (2009). Ionospheric time delay variations in equatorial anomaly region during low solar activity using GPS. *Indian Journal of Radio and Space Physics,* 38, 266–274.

Bhuyan P.K. & Borah R.R. (2007). TEC derived from GPS network in India and comparison with the IRI. *Advances in Space Research , 39*, 830-840.

Blanc, M. & Richmond,A. D. (1980). The Ionospheric disturbance dynamo. *Journal Of Geophysical Research , 85* (A4), 1669-1686.

Bolaji, O. S., Adeniyi, J. O., Adimula, I. A., Radicella, S.M. & Doherty P. H. (2013). Total electron content and magnetic field intensity over Ilorin, Nigeria. *Journal of Atmospheric and Solar-Terrestrial Physics , 98*, 1-11.

Burlaga, L. F. & Ogilvie, W. (1969). Causes of Sudden Commencements and Sudden Impulses. *Journal of Geophysical Research: Space Physics , 74* (11), 2815-2825.

Campbell, W. (1982). Annual and Semiannual Changes of the Quiet Daily Variations (Sq). *Journal Of Geophysical Research* , 785-796.

Campbell, W. (2003). *Introduction to geomagnetic fields* (2nd ed.). New York: Cambridge University Press.

Campbell, W. (1997). *Introduction to Geomagnetic Fields* (1st ed.). New York: Cambridge University Press.

Campbell, W. (1989). *Quiet Daily Geomagnetic Fields* (1st ed., Vol. 131). (W. H. Campbell, Ed.) Boston: Birkhiiuser Verlag Basel.

Carrano, C. S. (2007). GPS-SCINDA: A real time GPS Data Acquisition and Ionospheric analysis system for SCINDA, *Atmospheric and Environmental Research, Inc*. Lexicon, MA 02421

Chakraborty, M., Kumar, S.,DE, K. B. & Guha, A. (2015). Effects of geomagnetic storm on low latitude ionospheric total electron contnent. A case study from the Indian sector. *Journal of Earth System Science , 124*, 1115-1126.

Chandra, H. & Rastogi, R. G. (1997). Geomagnetic storm effects on zonal and meridional equatorial electrojet currents. *Journal of Geophysical Research , 102* (A6), 11611-11617.

Chen, Y., Liu, L., Wan, W., Yue, X. & Su, S. (2009). Solar activity dependence of the topside ionosphere at low latitudes. *Journal Of Geophysical Research* , 114, A08306, doi:10.1029/2008JA013957.

Dashora, N. & Pandey, R. (2005). Observations in equatorial anomaly region of total electron content enhancements and depletions. *Annales Geophysicae*, 23, 2449-2456.

de Haro Barbás, B. F., Ríos, V. H., Pérez Gómez, A. & Santillán, M. (2002). Variations of total electron content during a magnetic storm. *Geofísica Internacional , 41* (1), 49-55.

D'ujanga, F.M., Mubiru, J., Twinamasiko, B.F., Basalirwa, C. & Ssenyonga, T.J. (2012). Total electron content variations in equatorial anomaly region, *Advances in Space Research*, 50 (441-449).

El Hawary *et al.* (2012). Annual and semi-annual Sq variations at 96◦ MM MAGDAS I and II stations in Africa. *Earth Planets Space* , 64, 425–432.

Fejer, B. (2002). Low latitude storm time ionospheric electrodynamics. *Journal of Atmospheric and Solar-Terrestrial Physics* , 64,1401 – 1408.

Forbes, J. (2007). Dynamics of the Thermosphere. *Journal of the Meteorological Society of Japan , 85B*, 193-213.

Gonzales, C. A., Kelley, M. C., Fejer, B. G. Vickey, J. F.& Woodman, R. F. (1979). Equatorial Electric Fields During Magnetically Disturbed Conditions 2. Implications of Simultaneous Auroral and Equatorial Measurements. *Journal of Geophysical Research , 84* (A10), 5803-5812.

Goodman, J.M. (2005). *Space Weather and Telecommunications*. Radio Propagation Services, Inc. (RPSI), Alexandria, VA 22308-1943 USA, ISBN 0-387-23670-8.

Gopi, S. (2014). *Gopi Seemala Rinex GPS-TEC program version 2.9.2.* Retrieved February 29, 2016, from http://seemala.blogspot.com

Ho, C. M., Mannucci, A. J., Sparks, L., Pi, X., Lindq_wister, U. J., Wilson, B. D., Iijima, B. A. & Reyes, M. J. (1998). Ionospheric total electron content perturbations monitored by the GPS global network during two northern hemisphere winter storms. *Journal Of Geophysical Research , 103* (A11), 26,409-26,420

Jain, A., Sunita, T.,Sudhir, J. & Gwal, A. K. (2010). TEC response during severe geomagnetic storms near the crest of equatorial ionization anomaly. *Indian Journal of Radio & Space Physics , 39*, 11-24.

Kivelson, M. G and Russel, C. T. (1995). *Introduction to Space Physics.* New York: Cambridge University Press.

Knipp, J. (2011). *Understanding Space Weather and the Physics behind It* (1st ed.). New York: Mc Graw-Hill Companies Inc.

Lanyi, G. E. & Roth, T. (1988). A comparison of mapped and measured total ionospheric electron content using global positioning system and beacon satellite observations. *Radio Science , 23* (4), 4 83-492.

Lei, J., Thayer, J. P., Forbes, J. M., Sutton, E. K., Nerem, R. S, Temmer, M. & Veronig, A. M. (2008). Global thermospheric density variations caused by high-speed solar wind streams during the declining phase of solar cycle 23. *Journal Of Geophysical Research* , 113, A11303, doi:10.1029/2008JA013433.

Loewe, C. A. & Prolss, G. W. (1997). Classification and mean behavior of magnetic storms. *Journal Of Geophysical Research , 102* (A7), 14209-14213.

Macmillan, S. (2004/Rev.2006). Earth's magnetic field. In G. a. Geochemistry, *Encyclopedia of Life Support Systems.* Oxford ,UK: Eolss Publishers.

Matsushita, S., and Maeda, H. (1965). On the Geomagnetic Solar Quiet Daily Variation Field during the IGY. *Journal of Geophysical Research , 70* (11), 2535-2558.

National Aeronautics and Space Administration. (2016). *Solar Physics*. Retrieved from Solar Cycle Prediction: http://solarscience.msfc.nasa.gov/predict.shtml on 6th May, 2016.

National Oceanic and Atmospheric Administration. (2016). *Solar Cycle Progression*. Retrieved May 06, 2016, from Space Weather Prediction Center:

Nishida, A. (1968). Coherence of Geomagnetic D P2 Fluctuations with Interplanetary Magnetic Variations. *Journal of Geophysical Research: Space Physics , 73* (17), 5549-5559.

Obiekezie, T. N. and Obiadazie, S. C. (2013). The Variability of H component of Geomagnetic Field at the African Sector. *Physical Review & Research International*, 3(2), 154-160.

Okeke, F. N. and Hamano, Y. (2000). Daily variations of geomagnetic H, D and Z-field at equatorial latitudes. *Earth Planets Space*, **52**, 237-243.

Olwendo ,O.J., Baki , P., Cilliers, P.J., Mito ,C.& Doherty, P. (2012). Comparison of GPS TEC measurements with IRI-2007 TEC prediction over the Kenyan region during the descending phase of solar cycle 23. *Advances in Space Research , 49*, 914–921.

Omondi G. E., Baki P. and Ndinya B. (2016). Quiet Time Geomagnetic Field Variations in the Equatorial East African Region During the Inclining Phase of Solar Cycle 24. *International Journal of Astrophysics and Space Science.* Vol. 4, No. 2, pp. 21-25. doi: 10.11648/j.ijass.20160402.11

Oron, S., D'ujanga, F.M. & Ssenyonga, T. J. (2013). Ionospheric TEC variations during the ascending solar activity phase at an equatorial station, Uganda. *Indian Journal Of Radio & Space Physics , 42*, 7-17.

Oryema ,B., Jurua ,E., D’ujanga , F. M. & Ssebiyonga, N. (2015). Investigation of TEC variations over the magnetic equatorial and equatorial anomaly regions of the African sector. *Advances in Space Research , 56*, 1939–1950.

Oryema, B. Jurua, E. and Ssebiyonga, N. (2016).Variations of Crest-to-Trough TEC Ratio of the East African Equatorial Anomaly Region. *International Journal of Astrophysics and Space Science.* 4(1), 12-20, doi: 10.11648/j.ijass.20160401.12

Rabiu, A. (2001). Seasonal variability of Solar quiet at middle latitudes. *Ghana Journal of Science , 41*, 15-22.

Rabiu, A. B., Mamukuyomi, A. I. & Joshua, E. O. (2007). Variability of equatorial ionosphere inferred from geomagnetic field measurements. *Bulletin of Astronomical Society of India , 35*, 607-618.

Rabiu, A. B., Nagarajan, N., Okeke, F. N., Ariyibi, E. A.,Olayanju, G. M., Joshua, E. O. & Chukwuma,V. U. (2007). A Study Of day-to-day variability in geomagnetic field variations in the electrojet zone of Addis Ababa, East Africa. *African Journal of Science and Technology (AJST) Science and Engineering Series , 8* (2), 54 - 63.

Rabiu, A. B., Yumoto, K., Falayi, E.O., Bello, O.R.& MAGDAS/CPMN Group. (2011). Ionosphere over Africa: Results from Geomagnetic Field Measurements During International Heliophysical Year IHY. *Sun and Geosphere , 6* (2), 63 - 66.

Radicella, S. M. (2009). The African Ionosphere. *Satellite Navig. Sci and Tech for Africa Worksho*p (23rdMarch – 9th April 2009, ICTP, Trieste, Italy).

Rastogi, R. G. & Iyer, K.N. (1976). Quiet Day Variation of Geomagnetic H-Field at Low latitudes. *Journal of Geomagnetism and Geoelectricity , 28*, 461-479.

Rastogi, R. G. & Klobuchar, J. A. (1990). Ionospheric Electron Content Within the Equatorial F2 Layer Anomaly Belt. *Journal of Geophysical Research , 95* (A11), 19,045-19.

Rastogi, R. G. (2004). Electromagnetic induction by the equatorial electrojet. *Geophysical Journal International*, 158, 16-31.

Rastogi,R. G., Kitamura,T. & Kitamura, K. (2004). Geomagnetic field variations at the equatorial electrojet station in Sri Lanka, Peredinia. *Annales Geophysicae , 22*, 2729-2739.

Rastogi, R. G. (2006). Magnetic storm effects at equatorial electrojet stations. *Earth Planets Space , 58*, 645–657.

Seemala, G. K. & Valladares, C. E. (2011). Statistics of total electron depletions observed over South American continent for the year 2008. *Radio Science*, 46, RS5019, doi: 10.1029/2011RS004722.

Sharma, K., Dabas, R. S. & Sudha, R. (2012). Study of total electron content variations over equatorial and low latitude ionosphere during extreme solar minimum. *Astrophysics and Space Science* , doi 10.1007/s10509-012-1133-3.

Solar and Heliospheric Observatory (2002). *New Views of the Sun.* Retrieved from https://sohowww.nascom.nasa.gov/gallery/Presentations/slides 2002low.pdf on 1st November, 2017

Space Weather Prediction Centre: National Oceanic and Atmospheric Administration (2017). *Sunspot Number Progression*. Retrieved from http://www.swpc.noaa.gov/products/solar-cycle-progression on 6th June, 2017.

Stolle, C., Manoj, C., Luhr, H., Maus, S. & Alken, P. (2008). Estimating the daytime equatorial ionization anomaly strength from electric field proxies. *Journal of Geophysical Research , 113* , A09310, http://dx.doi.org/10.1029/2007JA012781.

Takeda, M. & Araki, T. (1985). Electric conductivity of the ionosphere and nocturnal currents. *Journal of Atmospheric and Terrestrial Physics , 47* (6), 601-609.

Veenadhari, B. & Alex, S. (2006). Space weather effects on low latitude geomagnetic field and ionospheric plasma response. *ILWS Workshop,February 19-24.* GOA.

Wong, A. (2009). US space-based PNT international cooperation and support in Africa. *Bureau of Oceans & Environ. Sci. Satellite & Navig. Sci. and Tech. for Africa Workshop* (23rd March – 9th April 2009, ICTP, Trieste, Italy)

World Data Center for Geomagnetism,Kyoto. (2016). *Geomagnetic Data Service.* Retrieved January 04, 2016, from http://wdc.kugi.Kyoto-u.ac.jp/cgi-bin/Kp-cgi

Yamazaki, Y. & Kosch, M. J. (2015). The equatorial electrojet during geomagnetic storms and substorms. *Journal of Geophysical Research: Space Physics , 120,* 2276-2287,doi:10.1002/2014JA020773.

Yamazaki, Y., Yumoto, K., Cardinal, M. G., Fraser, B. J., Hattori, P., Kakinami,Y.,. Liu,J. Y, Lynn, K. J. W., Marshall, R., McNamara, D., Nagatsuma, T., Nikiforov,V. M.,. Otadoy, R. E, Ruhimat, M., Shevtsov, B. M., Shiokawa,K.,Abe, S.,Uozumi,T.&Yoshikawa, A. (2011). An empirical model of the quiet daily geomagnetic field variation. *Journal of Geophysical Research , 116* (A10312), doi:10.1029/2011JA016487.

Yeh, K. C. & Franke, S. J. (2001). An Investigation of Motions of the Equatorial Anomaly Crest. *Geophysical Research Letters , 28* (24), 4517-4520.

Zhao, B., Wan, W., & Liu, L. (2005). Responses of equatorial anomaly to the October–November 2003 superstorms. *Annales Geophysicae*, 23, 693–706.

APPENDICES
APPENDIX A: TYPICAL GEOMAGNETIC DATA PROCESSING SCRIPT

```
%%% A script to  process the MIN files giving the desired outputs
    by George Omondi

%%% We first close all opened files, clear them and clear the command
%%% window  as well using the following three syntaxes respectively
 close all,
 clear all,
 clc
%% We now specify the datapath

Datapath = 'D:\SANSA SVS 2016\MAGNETICDATA\INTERMAGNET\AAE\2014\*.min'; %
Path to the directory containing the data + the extension of the files to
look for

Dirtry ='D:\SANSA SVS 2016\MAGNETICDATA\INTERMAGNET\AAE\2014\';
MIN_FILES = dir(Datapath);%List the files found in the above directory
(Datapath)
numfiles=size(MIN_FILES,1);%Count the number of the CMN_FILES found in the
Datapath

for k = 1:numfiles %start processing the files 1 by 1
       MAGFIELD = [Dirtry MIN_FILES(k).name]; % Specifying the current file
to process + the extention as a function of k which varies the file position
in directory.

        disp(['Processing file ....    ', MAGFIELD]);% Display the CMN file
being processed

%==========opening MAGFIELD==============
% % fid=fopen(MAGFIELD);
% %% start to read the file
%
% disp('reading data... ');
% while feof(fid)==0
%     fg=fgetl(fid);
% end
fid  = fopen(MAGFIELD,'r');
UNPROCESSED_MAGFIELD = textscan(fid,'%s %s %f %f %f %f %f
','headerlines',25);
fclose(fid);

AX = cell2mat(UNPROCESSED_MAGFIELD(:,4));

AY = cell2mat(UNPROCESSED_MAGFIELD(:,5));%cell2mat is conversion of each cell
to a matrix
AX_Sq=AX.^2;
AY_Sq=AY.^2;
AH=sqrt(AX_Sq+AY_Sq);
AUT = (0:0.01666666666666667:24)';
ALT1=AUT(1286:1440,1)+2.58266667-24;
ALT2=AUT(1:1285,1)+2.58266667;%converting  first section to local time
```

```
LT_data=zeros(1440,2);
LT_data(1:155,1)=ALT1;
LT_data(156:1440,1)=ALT2;

LT_data(1:155,2)=AH(1286:1440,1);
LT_data(156:1440,2)=AH(1:1285,1);
ALT=LT_data(:,1);
AHLT=LT_data(:,2);
ALT(ALT<0)=(0);% setting the value of about -0.001 which occurs at 24 UT to
zero.

% Any H component value greater or equal to 10000 should be set to NaN.
AH(AH>=40000) = [NaN]';
%Calculating Sq(H)
AdH=AHLT-nanmean(AHLT(1:300,1));
AHdc=(AdH(1440,1)-AdH(1,1))/sum(~isnan(AdH)-1);
ASqH=AdH+(ALT-1).*AHdc;
 ASqH(ASqH>=40000) = [NaN]';
Aoutput_data = [ALT  ASqH];%creating a matrix with column 1 NLT ,column2 NHLT
and Sq(H) column3


%% figure
plot(ALT,ASqH);


%% writing data into the script
 PROCESSED_MAGFIELD =['OUTPUT-' MIN_FILES(k).name '.Cmn'];
 fid1 =fopen(PROCESSED_MAGFIELD,'wt');
%  fprintf(fid1,'UT \t\t VTEC\n'); % headings
 for i =1:length(Aoutput_data)
          fprintf(fid1,'%6.3f\t %8.2f
\n',Aoutput_data(i,1),Aoutput_data(i,2));
  end
 fclose(fid1);


end

%=======================================================end===================
==========================================================
disp('Successfully completed, God is awesome)');
```

APPENDIX B: TYPICAL GPS CMN FILES PROCESSING SCRIPT

```
%%% A script to quickly process the CMN files giving the desired outputs
%%  by George Omondi

%%% We first close all opened files, clear them and clear the command
%%% window  as well using the following three syntaxes respectively
 close all,
 clear all,
 clc
%% We now specify the datapath

Datapath = 'D:\SANSA SVS 2016\TEC ANALYSIS_SOFTWARE AND
DATA\Obs\Obs\ADIS_TEC_IGS\2014\2014PROCESSED\FILES\*.Cmn'; % Path to the
directory containing the data + the extension of the files to look for

Dirtry ='D:\SANSA SVS 2016\TEC ANALYSIS_SOFTWARE AND
DATA\Obs\Obs\ADIS_TEC_IGS\2014\2014PROCESSED\FILES\';
CMN_FILES = dir(Datapath);%List the files found in the above directory
(Datapath)
numfiles=size(CMN_FILES,1);%Count the number of the CMN_FILES found in the
Datapath

for k = 1:numfiles %start processing the files 1 by 1
       VTEC = [Dirtry CMN_FILES(k).name]; % Specifying the current file to
process + the extention as a function of k which varies the file position in
directory.

        disp(['Processing file ....    ', VTEC]);% Display the CMN file being
processed

% %==========opening vTEC==============
% fid=fopen(VTEC);
% %% start to read the file
%
% disp('reading data... ');
% while feof(fid)==0
%     fg=fgetl(fid);
% end
fid  = fopen(VTEC,'r');
UNPROCESSED_VTEC = textscan(fid,'%f %f %f %f %f %f %f %f %f %f
','headerlines',5);
fclose(fid);

AUt = cell2mat(UNPROCESSED_VTEC(:,2));%cell2mat is conversion of each cell to
a matrix

% Any Universal time value equal to -24 should be replaced with zero
AUt(AUt==-24) = [0];

APrn=cell2mat(UNPROCESSED_VTEC(:,3));
AEl=cell2mat(UNPROCESSED_VTEC(:,5));
AVtec=cell2mat(UNPROCESSED_VTEC(:,9));
```

```
 indx = find(AEl>=70);%%setting a threshold elevation angle to be used in
data selection
AUT=AUt(indx);
APRN=APrn(indx);
AEL =AEl(indx);
AVTEC=AVtec(indx);
[a, b, c]=unique(AUT);%%setting the function to average TEC that occur at the
same time (overlap) from different PRNS.
Aoutput_data=[a(:), accumarray(c, AVTEC, [],@mean)];%carrying out the
averaging and giving the outputs
Anew_time=Aoutput_data(:,1);%%defining new time column in the output data i.e
column 1
ATEC_mean=Aoutput_data(:,2);%%defining the column for mean of VTEC in the
resultant data set i.e column2

ALT=Anew_time+2.58266667;

ANewoutput_data = [Anew_time ALT ATEC_mean];
% Newoutput = [Anew_time ATEC_mean];
%% figure
plot(ALT,ATEC_mean);


%% writing data into the script
 PROCESSED_VTEC =['OUTPUT-' CMN_FILES(k).name];
 fid1 =fopen(PROCESSED_VTEC,'wt');
%  fprintf(fid1,'UT \t\t VTEC\n'); % headings
 for i =1:length(ANewoutput_data)
          fprintf(fid1,'%6.5f \t %6.5f \t %5.3f
\n',ANewoutput_data(i,1),ANewoutput_data(i,2),ANewoutput_data(i,3));
  end
 fclose(fid1);


end

%======================================================end===================
==========================================================
disp('Successfully completed, God is good)');
```

APPENDIX C: SAMPLE DATA ANALYSIS SCRIPT: PART OF FEBRUARY 2014 QUIET TIME

```
clear all
close all
% .......................................................................
%
% % % % % % SHEET1 BELOW
% %
Scriptpath='C:\Users\Omondi\Documents\MATLAB';
addpath(Scriptpath);
Datapath='E:\EXCELDATASHEETSSANSA\NEWANALYSIS\TEC_SQHPROCESSED\2014';
datestr1='AAB_NAB_TECSQH2014FEBQUIET.xlsx';
sheet='sheet1';
filename=datestr1;
% % % % import Excel spreadsheet
cd(Datapath);
if exist(filename,'file')
    sheet1= xlsread(filename,sheet);
else
    fprintf('%s not found in %s \n',filename,Datapath);
end

AUTTEC=sheet1(:,1);
ALTTEC=sheet1(:,2);
ATEC=sheet1(:,3);
ALTSq=sheet1(:,4);
ASqH=sheet1(:,5);
NUTTEC=sheet1(:,6);
NLTTEC=sheet1(:,7);
NTEC=sheet1(:,8);
NLTSq=sheet1(:,9);
NSqH=sheet1(:,10);
EEJ=ASqH-NSqH;
ATEC(ATEC<0)=(NaN);
NTEC(NTEC<0)=(NaN);



ALTtec=sheet1(1:sum(~isnan(ALTTEC)),2);
ATEc=sheet1(1:sum(~isnan(ALTTEC)),3);

NLTtec=sheet1(1:sum(~isnan(NLTTEC)),7);
NTEc=sheet1(1:sum(~isnan(NLTTEC)),8);




subplot(211)
plot(ALTSq,ASqH,'r','LineWidth',3);ylabel('SqH(nT)');set(gca,'XTick',0:4:24);
xlim([0 23.99]),ylim([-50 100]),
title('Sq(H)on 20140202');
legend('AAB')
 grid on
```

```
subplot(212),
plot(ALTTEC,ATEC,'r--','LineWidth',3);xlabel('Local time
(hours)'),ylabel('VTEC(TECU)');set(gca,'XTick',0:4:24);
xlim([0 23.99]),ylim([0 40]);
title('VTEC on 20140202');
legend('AAB');
 grid on

 pause

 subplot(211),
plot(NLTSq,NSqH,'k','LineWidth',3);ylabel('SqH(nT)');set(gca,'XTick',0:4:24);
xlim([0 23.99]);ylim([-50 100]);
title('Sq(H)on 20140202');
legend('NAB')
 grid on



subplot(212),
plot(NLTTEC,NTEC,'k--','LineWidth',3);xlabel('Local time
(hours)'),ylabel('VTEC(TECU)');set(gca,'XTick',0:4:24);
xlim([0 23.99]),ylim([0 40]);
title('VTEC on 20140202');
legend('NAB')
 grid on

 pause
 LT=(7:0.1:19)';
 Atec=interp1(ALTtec,ATEc,LT);%sampling(interpolating) values at 0.1 hr time
intervals to get points to compare exactly with geomagnetic field time
instants.
 AsqH=interp1(ALTSq,ASqH,LT);
 Eej=interp1(ALTSq,EEJ,LT);
 Ntec=interp1(NLTtec,NTEc,LT);
 NsqH=interp1(NLTSq,NSqH,LT);

[AX,H1,H2] = plotyy(LT,AsqH,LT,Atec,'plot');
set(get(AX(1),'Ylabel'),'String','Sq(H) (nT)', 'Color','r');
set(AX(1),'YColor','r');
set(AX(2),'YColor','b');
set(get(AX(2),'Ylabel'),'String','VTEC (TECU)','Color','b');
set(AX,'XTick',7:2:19);
set(AX(1),'YTick',-50:50:100);
set(AX(2),'YTick',0:20:40);
xlabel('Local time (hours)'); grid on
title('AABSqHVTEC on 20140202') ;
set(H1,'LineStyle','-');
set(H2,'LineStyle','-');
set(H1,'LineWidth',3);
set(H1,'Color','r');
set(H2,'LineWidth',3);
set(H2,'Color','b');
```

```
pause

[AX,H1,H2] = plotyy(LT,Eej,LT,Atec,'plot');
set(get(AX(1),'Ylabel'),'String','EEJ(nT)', 'Color','r');
set(AX(1),'YColor','r');
set(AX(2),'YColor','b','YTick',0:20:40);
set(AX(1),'YTick',-50:50:100);
set(get(AX(2),'Ylabel'),'String','VTEC (TECU)','Color','b');
set(AX,'XTick',7:2:19);
xlabel('Local time (hours)');
title('AABEEJVTEC on 20140202') ;
set(H1,'LineStyle','-');
set(H2,'LineStyle','-');
set(H1,'LineWidth',3);
set(H1,'Color','r');
set(H2,'LineWidth',3);grid on
set(H2,'Color','b');

pause

[AX,H1,H2] = plotyy(LT,NsqH,LT,Ntec,'plot');
set(get(AX(1),'Ylabel'),'String','Sq(H)(nT)', 'Color','k');
set(AX(1),'YColor','k');
set(AX(2),'YColor','b');
set(get(AX(2),'Ylabel'),'String','VTEC (TECU)','Color','b');
set(AX,'XTick',7:2:19);
set(AX(1),'YTick',-50:50:130);
set(AX(2),'YTick',0:20:40);
xlabel('Local time (hours)'); grid on
title('NABSqHVTECon 20140202') ;
set(H1,'LineStyle','-');
set(H2,'LineStyle','-');
set(H1,'LineWidth',3);
set(H1,'Color','k');
set(H2,'LineWidth',3);
set(H2,'Color','b');

AAB_results01=[Atec AsqH Eej];
NAB_results01=[Ntec NsqH];

%
%
pause
%
% % % ..........................................................

% % % SHEET2 BELOW

...........................................................................

Scriptpath='C:\Users\Omondi\Documents\MATLAB';
addpath(Scriptpath);
Datapath='E:\EXCELDATASHEETSSANSA\NEWANALYSIS\TEC_SQHPROCESSED\2014';
datestr1='AAB_NAB_TECSQH2014FEBQUIET.xlsx';
sheet='sheet2';
```

```
filename=datestr1;
% % % % import Excel spreadsheet
cd(Datapath);
if exist(filename,'file')
    sheet2= xlsread(filename,sheet);
else
    fprintf('%s not found in %s \n',filename,Datapath);
end
sheet1=sheet2;
AUTTEC=sheet1(:,1);
ALTTEC=sheet1(:,2);
ATEC=sheet1(:,3);
ALTSq=sheet1(:,4);
ASqH=sheet1(:,5);
NUTTEC=sheet1(:,6);
NLTTEC=sheet1(:,7);
NTEC=sheet1(:,8);
NLTSq=sheet1(:,9);
NSqH=sheet1(:,10);
EEJ=ASqH-NSqH;
ATEC(ATEC<0)=(NaN);
NTEC(NTEC<0)=(NaN);




ALTtec=sheet1(1:sum(~isnan(ALTTEC)),2);
ATEc=sheet1(1:sum(~isnan(ALTTEC)),3);

NLTtec=sheet1(1:sum(~isnan(NLTTEC)),7);
NTEc=sheet1(1:sum(~isnan(NLTTEC)),8);






subplot(211)
plot(ALTSq,ASqH,'r','LineWidth',3);ylabel('SqH(nT)');set(gca,'XTick',0:4:24);
xlim([0 23.99]),ylim([-50 100]),
title('Sq(H)on 20140203');
legend('AAB')
 grid on



subplot(212),
plot(ALTTEC,ATEC,'r--','LineWidth',3);xlabel('Local time
(hours)'),ylabel('VTEC(TECU)');set(gca,'XTick',0:4:24);
xlim([0 23.99]),ylim([0 40]);
title('VTEC on 20140203');
legend('AAB');
 grid on

 pause

 subplot(211),
plot(NLTSq,NSqH,'k','LineWidth',3);ylabel('SqH(nT)');set(gca,'XTick',0:4:24);
```

```
xlim([0 23.99]);ylim([-50 100]);
title('Sq(H)on 20140203');
legend('NAB')
 grid on


subplot(212),
plot(NLTTEC,NTEC,'k--','LineWidth',3);xlabel('Local time
(hours)'),ylabel('VTEC(TECU)');set(gca,'XTick',0:4:24);
xlim([0 23.99]),ylim([0 40]);
title('VTEC on 20140203');
legend('NAB')
 grid on

 pause
 LT=(7:0.1:19)';
 Atec=interp1(ALTtec,ATEc,LT);%sampling(interpolating) values at 0.1 hr time
intervals to get points to compare exactly with geomagnetic field instants.
 AsqH=interp1(ALTSq,ASqH,LT);
 Eej=interp1(ALTSq,EEJ,LT);
 Ntec=interp1(NLTtec,NTEc,LT);
 NsqH=interp1(NLTSq,NSqH,LT);

[AX,H1,H2] = plotyy(LT,AsqH,LT,Atec,'plot');
set(get(AX(1),'Ylabel'),'String','Sq(H) (nT)', 'Color','r');
set(AX(1),'YColor','r');
set(AX(2),'YColor','b');
set(get(AX(2),'Ylabel'),'String','VTEC (TECU)','Color','b');
set(AX,'XTick',7:2:19);
set(AX(1),'YTick',-50:50:100);
set(AX(2),'YTick',0:20:40);
xlabel('Local time (hours)'); grid on
title('AABSqHVTEC on 20140203') ;
set(H1,'LineStyle','-');
set(H2,'LineStyle','-');
set(H1,'LineWidth',3);
set(H1,'Color','r');
set(H2,'LineWidth',3);
set(H2,'Color','b');

pause

[AX,H1,H2] = plotyy(LT,Eej,LT,Atec,'plot');
set(get(AX(1),'Ylabel'),'String','EEJ(nT)', 'Color','r');
set(AX(1),'YColor','r');
set(AX(2),'YColor','b','YTick',0:20:40);
set(AX(1),'YTick',-50:50:100);
set(get(AX(2),'Ylabel'),'String','VTEC (TECU)','Color','b');
set(AX,'XTick',7:2:19);
xlabel('Local time (hours)');
title('AABEEJVTEC on 20140203') ;
set(H1,'LineStyle','-');
set(H2,'LineStyle','-');
set(H1,'LineWidth',3);
set(H1,'Color','r');
set(H2,'LineWidth',3);grid on
```

```
set(H2,'Color','b')
pause

[AX,H1,H2] = plotyy(LT,NsqH,LT,Ntec,'plot');
set(get(AX(1),'Ylabel'),'String','Sq(H)(nT)', 'Color','k');
set(AX(1),'YColor','k');
set(AX(2),'YColor','b');
set(get(AX(2),'Ylabel'),'String','VTEC (TECU)','Color','b');
set(AX,'XTick',7:2:19);
set(AX(1),'YTick',-50:50:130);
set(AX(2),'YTick',0:20:40);
xlabel('Local time (hours)'); grid on
title('NABSqHVTEC on 20140203') ;
set(H1,'LineStyle','-');
set(H2,'LineStyle','-');
set(H1,'LineWidth',3);
set(H1,'Color','k');
set(H2,'LineWidth',3);
set(H2,'Color','b');

AAB_results02=[Atec AsqH Eej];
NAB_results02=[Ntec NsqH];

pause
%% ..................................................................
% % % % % SHEET3 BELOW

...................................................................
clc
Scriptpath='C:\Users\Omondi\Documents\MATLAB';
addpath(Scriptpath);
Datapath='E:\EXCELDATASHEETSSANSA\NEWANALYSIS\TEC_SQHPROCESSED\2014';
datestr1='AAB_NAB_TECSQH2014FEBQUIET.xlsx';
sheet='sheet3';
filename=datestr1;
% % % % import Excel spreadsheet
cd(Datapath);
if exist(filename,'file')
    sheet3= xlsread(filename,sheet);
else
    fprintf('%s not found in %s \n',filename,Datapath);
end
sheet1=sheet3;
AUTTEC=sheet1(:,1);
ALTTEC=sheet1(:,2);
ATEC=sheet1(:,3);
ALTSq=sheet1(:,4);
ASqH=sheet1(:,5);
NUTTEC=sheet1(:,6);
NLTTEC=sheet1(:,7);
NTEC=sheet1(:,8);
NLTSq=sheet1(:,9);
NSqH=sheet1(:,10);
EEJ=ASqH-NSqH;
ATEC(ATEC<0)=(NaN);
NTEC(NTEC<0)=(NaN);
```

```
ALTtec=sheet1(1:sum(~isnan(ALTTEC)),2);
ATEc=sheet1(1:sum(~isnan(ALTTEC)),3);

NLTtec=sheet1(1:sum(~isnan(NLTTEC)),7);
NTEc=sheet1(1:sum(~isnan(NLTTEC)),8);




subplot(211)
plot(ALTSq,ASqH,'r','LineWidth',3);ylabel('SqH(nT)');set(gca,'XTick',0:4:24);
xlim([0 23.99]),ylim([-50 100]),
title('Sq(H)on 20140204');
legend('AAB')
 grid on


subplot(212),
plot(ALTTEC,ATEC,'r--','LineWidth',3);xlabel('Local time
(hours)'),ylabel('VTEC(TECU)');set(gca,'XTick',0:4:24);
xlim([0 23.99]),ylim([0 40]);
title('VTEC on 20140204');
legend('AAB');
 grid on

 pause

 subplot(211),
plot(NLTSq,NSqH,'k','LineWidth',3);ylabel('SqH(nT)');set(gca,'XTick',0:4:24);
xlim([0 23.99]);ylim([-50 100]);
title('Sq(H)on 20140204');
legend('NAB')
 grid on


subplot(212),
plot(NLTTEC,NTEC,'k--','LineWidth',3);xlabel('Local time
(hours)'),ylabel('VTEC(TECU)');set(gca,'XTick',0:4:24);
xlim([0 23.99]),ylim([0 40]);
title('VTEC on 20140204');
legend('NAB')
 grid on

 pause
 LT=(7:0.1:19)';
 Atec=interp1(ALTtec,ATEc,LT);%sampling(interpolating) values at 0.1 hr time
intervals to get points to compare exactly with geomagnetic field instants.
 AsqH=interp1(ALTSq,ASqH,LT);
 Eej=interp1(ALTSq,EEJ,LT);
 Ntec=interp1(NLTtec,NTEc,LT);
 NsqH=interp1(NLTSq,NSqH,LT);
```

```
[AX,H1,H2] = plotyy(LT,AsqH,LT,Atec,'plot');
set(get(AX(1),'Ylabel'),'String','Sq(H) (nT)', 'Color','r');
set(AX(1),'YColor','r');
set(AX(2),'YColor','b');
set(get(AX(2),'Ylabel'),'String','VTEC (TECU)','Color','b');
set(AX,'XTick',7:2:19);
set(AX(1),'YTick',-50:50:100);
set(AX(2),'YTick',0:20:40);
xlabel('Local time (hours)'); grid on
title('AABSqHVTEC on 20140204') ;
set(H1,'LineStyle','-');
set(H2,'LineStyle','-');
set(H1,'LineWidth',3);
set(H1,'Color','r');
set(H2,'LineWidth',3);
set(H2,'Color','b');

pause

[AX,H1,H2] = plotyy(LT,Eej,LT,Atec,'plot');
set(get(AX(1),'Ylabel'),'String','EEJ(nT)', 'Color','r');
set(AX(1),'YColor','r');
set(AX(2),'YColor','b','YTick',0:20:40);
set(AX(1),'YTick',-50:50:100);
set(get(AX(2),'Ylabel'),'String','VTEC (TECU)','Color','b');
set(AX,'XTick',7:2:19);
xlabel('Local time (hours)');
title('AABEEJVTEC on 20140204') ;
set(H1,'LineStyle','-');
set(H2,'LineStyle','-');
set(H1,'LineWidth',3);
set(H1,'Color','r');
set(H2,'LineWidth',3);grid on
set(H2,'Color','b');

pause

[AX,H1,H2] = plotyy(LT,NsqH,LT,Ntec,'plot');
set(get(AX(1),'Ylabel'),'String','Sq(H)(nT)', 'Color','k');
set(AX(1),'YColor','k');
set(AX(2),'YColor','b');
set(get(AX(2),'Ylabel'),'String','VTEC (TECU)','Color','b');
set(AX,'XTick',7:2:19);
set(AX(1),'YTick',-50:50:130);
set(AX(2),'YTick',0:20:40);
xlabel('Local time (hours)'); grid on
title('NABSqHVTEC on 20140204') ;
set(H1,'LineStyle','-');
set(H2,'LineStyle','-');
set(H1,'LineWidth',3);
set(H1,'Color','k');
set(H2,'LineWidth',3);
set(H2,'Color','b');

AAB_results03=[Atec AsqH Eej];
```

```
NAB_results03=[Ntec NsqH];
```